INSCRIPTION AND ANALYSIS OF NON-UNIFORM DIFFRACTION GRATINGS IN AZOBENZENE MOLECULAR GLASS THIN FILMS

INSCRIPTION ET ANALYSE DES RÉSEAUX DE DIFFRACTION NON-UNIFORMES SUR DES FILMS MINCES DE VERRES MOLÉCULAIRES D'AZOBENZÈNE

A Thesis Submitted to the Division of Graduate Studies of the Royal Military College of Canada by

Nicholas Tyler O'Krane Swanson
A/SLt

In Partial Fulfillment of the Requirements for the Degree of Masters of Science

April 2018

Acknowledgements

I would like to thank my supervisor Dr. Ribal Georges Sabat for his endless patience and encouragement and for providing me with the resources necessary to complete this thesis.

I would also like to sincerely thank my loving wife, Deborah Swanson, for her support throughout this Master's program, and the hours spent patiently editing this thesis.

Abstract

A Direct Interference Lithography Patterning technique was used to inscribe non-uniform, or spatially curving, surface relief diffraction gratings on photomechanical thin films using a modified Lloyd's mirror interferometer. The experimentally-fabricated gratings are compared to a theoretical model, developed by simulating the recombined laser interference phase information to theoretically achieve various non-uniform grating profiles as it would be expected in the actual fabrication process. A Coherent Verdi V5 diode-pumped continuous wave laser, having a wavelength $\lambda = 532$ nm, was used to experimentally generate a collimated and circularly-polarized laser beam. A spherical lens having a 5.72 mm diameter was placed along the laser beam path towards the Lloyd's mirror interferometer to produce a spherically-curving wave front and to generate a non-uniform interference pattern, which was imprinted on a Disperse Red 1 molecular glass thin film. It was found that two parameters could be used to control the overall distribution of the non-uniform grating's physical and optical properties: the laser incidence angle, dictating the central grating pitch, and the physical position of the spherical lens. These parameters were varied to experimentally and theoretically produce twelve different non-uniform gratings. Central pitch values of $\Lambda = 500$ nm, $\Lambda = 1000$ nm, $\Lambda = 1500$ nm, and $\Lambda = 2000$ nm were used for inscription at lens positions of $f = 35$ mm, $f = 45$ mm, and $f = 55$ mm from the azobenzene film surface. An Atomic Force Microscope was used to characterize the resulting gratings in order to obtain the localized grating pitch, vector orientation and modulation depths at 25 X-Y coordinates on the grating's surface. The experimental results and theoretical simulations were compared using three-dimensional vector plots. The grating's pitch and vector information were found to be in close agreement between the theoretical and experimental results. The experimental modulation depth was compared to a theoretical laser irradiance distribution, and some variation was found and explained. This method for non-uniform grating fabrication was found to produce cheap and inexpensive gratings with easily controllable optical parameters, which allows them to be used in a variety of photonics application in research and industry.

Résumé

Une technique de fabrication par lithographie en interférence directe a été utilisée pour inscrire des réseaux de diffraction non uniformes, ou spatialement incurvés, sur des films minces photomécaniques en utilisant un interféromètre à miroir de Lloyd modifié. Les réseaux fabriqués expérimentalement sont comparés à un modèle théorique, developé en simulant l'information de phase d'interférence recombinée pour obtenir théoriquement des différents profils de réseaux non uniformes comme on peut s'y attendre dans le processus de fabrication expérimental. Un laser à onde continue pompé par diode Verdi V5 de Coherent, ayant une longueur d'onde λ = 532 nm, a été utilisé pour générer expérimentalement un faisceau laser collimaté et à polarisation circulaire. Une lentille sphérique de 5,72 mm de diamètre a été placée le long du trajet du faisceau laser vers l'interféromètre à miroir de Lloyd pour produire un front d'onde sphériquement incurvé et pour générer un patron d'interférence non uniforme qui a été imprimé sur un verre moléculaire Disperse Red 1 en couche mince. Il a été constaté que deux paramètres pouvaient être utilisés pour contrôler les propriétés physiques et optiques d'un réseau non uniforme: l'angle d'incidence du laser, dictant le pas central du réseau, et la position physique de la lentille sphérique. Ces paramètres ont été variés pour générer expérimentalement et théoriquement douze réseaux non uniformes différents. Les valeurs du pas central de Λ = 500 nm, Λ = 1000 nm, Λ = 1500 nm et Λ = 2000 nm ont été utilisées pour l'inscription aux positions de lentilles de f = 35 mm, f = 45 mm et f = 55 mm de la surface du film d'azobenzène. Un microscope à force atomique a été utilisé pour caractériser les réseaux résultants afin d'obtenir les informations sur le pas local du réseau, l'orientation du vecteur du réseau et la profondeur de modulation sur 25 coordonnées X-Y sur la surface du film. Les résultats expérimentaux et les simulations théoriques ont été comparés en utilisant des tracés vectoriels tridimensionnels. Les informations du pas et du vecteur du réseau ont été trouvées en accord étroit entre les résultats théoriques et expérimentaux. La profondeur de modulation expérimentale a été comparée à une distribution théorique d'irradiance laser, et une variation a été trouvée et expliquée. Cette méthode pour la fabrication de réseaux non uniformes a été trouvée de produire des réseaux avec des paramètres optiques facilement contrôlables, ce qui leur permet d'être utilisés dans une variété d'applications photoniques dans la recherche et l'industrie.

Contents

List of Tables

List of Figures

List of Abbreviations

AFM: Atomic Force Microscope

DNA: Deoxyribonucleic Acid

FIB: Focused Ion Beam

Ga^{+}: Gallium ion

gDR1: Disperse Red 1 Molecular Glass

PDMS: poly(dimethylsiloxane)

SCD: Single Crystal Diamond

SRG: Surface Relief Grating

List of Symbols

Roman Symbols

Symbols	Description (units)	Definition
c	Speed of light (m/s)	
f	Distance from the spherical lens to the axis of intersection between the azobenzene film and the Lloyd's mirror (mm)	
f_1	Focal length of the lens (mm)	14.3 mm
k	Wave number (m^{-1})	
$\boldsymbol{k}$	Wave vector (m^{-1})	
m	Diffraction order (no units)	
$\boldsymbol{l}$	Vector normal to the propagation direction (no units)	
$\boldsymbol{r}$	Position vector	
s_1	Path length traveled by the laser beam (mm)	
t	Time (s)	
$\boldsymbol{E}$	Electric Field Vector (V/m)	
$\boldsymbol{H}$	Magnetic Field Vector (A/m)	
I	Irradiance (W/m^2)	
I_1	Irradiance from the direct laser beam in a Lloyd's mirror interferometer (W/m^2)	
I_2	Irradiance from the reflected laser beam in a Lloyd's mirror interferometer (W/m^2)	
I_{12}	Interference irradiance (W/m^2)	
$\boldsymbol{J}$	Volume current density (A/m^3)	
$\mathbf{K}$	Grating vector (no units)	
L	Width of inscription area along the X-axis (mm)	
$\boldsymbol{S}$	Poynting vector (W/m^2)	
T	Grating modulation depth (nm)	

Greek Symbols

Symbol	Description (units)	Definition
δ	Phase difference between two laser beams (no units)	
ϵ	Position change in the spherical lens (mm)	
ϵ_o	Permittivity of free space (F/m)	$8.854 \times 10^{-12} \frac{F}{m}$
θ	Angle between the Lloyd's mirror and the optical axis (degrees)	
θ_i	Angle of the incident light on the grating surface (degrees)	
θ_m	Angle of the reflected/transmitted light from the grating surface (degrees)	
λ	The laser wavelength (nm)	532 nm
μ_o	Permeability of free space (H/m)	$1.257 \times 10^{-6} \frac{H}{m}$
ν	Velocity of a wave (m/s)	
ϕ	Phase shift contributed by the addition of a spherical lens (no units)	
ψ	Applied phase shift (no units)	
ω	Angular frequency (s^{-1})	
Δ	Optical path length contributed by the divergence of the laser beam from the spherical lens (nm)	
Λ	Grating central pitch (nm)	

Operators

Symbol	Description
A	Scalar
$\|A\|$	Absolute value of Scalar A
$\boldsymbol{A}$	Vector
A_o	Magnitude of A
$\widetilde{\boldsymbol{A}}$	Complex vector
$\nabla\boldsymbol{A}$	Gradient of vector A
$\|\boldsymbol{A}\|$	Magnitude of vector A
$\langle\boldsymbol{A}\rangle$	Time average of vector A
$\widehat{\boldsymbol{A}}$	Unit vector of vector A
$\hat{\boldsymbol{n}}$	Unit vector in the n direction

Chapter 1 Introduction

1.1 Diffraction Grating Background

The study of optical diffraction and its properties originates from observations made by Isaac Newton in 1672 when the separation of the visible colour spectrum occurred upon irradiating a ½ mm wide slit with white light [1]. It was not until the early 1800s that further observations of this phenomena would be studied and recorded. Since these preliminary stages, the study of optical diffraction has progressed drastically as new and powerful lasers became accessible, optical lenses were fabricated to minimize impurities and have carefully tuned properties, and the ability to produce optical structures at progressively smaller scales became achievable [2].

In modern optics and photonics research, the most common method used to produce optical diffraction is through the use of diffraction gratings. Diffraction gratings are periodically repeating structures, with a structure separation typically at the scale of the incident light's wavelength. Although diffraction gratings can be a series of slits cut into an opaque wafer, this thesis will focus strictly on a type of diffraction grating known as a Surface Relief Grating (SRG).

SRGs are defined as periodic undulations on the surface of a material. The surface undulations interact with incident light in the same manner as a slit diffraction grating does, however the difference between the two is that a SRG is not cut through a material but rather resides strictly on the material's surface. The SRG induces diffraction by introducing a periodic alternation between two different optical materials thereby varying the refractive index of the medium the light is interacting with. The benefit of this feature is that diffraction can be achieved through either reflection or transmission depending on the transparency of the materials onto which the grating is inscribed. Another method of producing optical diffraction is by modulating the incident light's amplitude by introducing a series of opaque and transparent regions with which the light interacts [3]. Any transmissive diffraction grating that accomplishes diffraction through the alteration of the light's amplitude is known as a transmission amplitude grating. Slit diffraction gratings are classified in this category. For many surface relief gratings, diffraction is produced by modulating the phase of the incident light by introducing periodic trenches in the surface. The properties of diffraction caused from the transmitted and the reflected light are very similar in nature. Therefore, any grating producing diffraction in this

manner through transmission is known as a transmission phase grating and through reflection is known as a reflection phase grating.

The fabrication methods of SRGs vary drastically and consequentially produce surface profiles of different shapes. The most common grating structures are sinusoidal, square, saw-tooth, and triangular. In each case, the structure will repeat periodically with a distance between the periodic structures measured from one peak to the next. This peak-to-peak distance is known as the grating pitch with most SRG applications having pitch lengths which correspond to wavelengths within the visible range of electromagnetic radiation. Another property that is used to characterize diffraction gratings is the grating vector which is defined as the vector perpendicular to the peaks of the surface undulations and is parallel to the surface. A side profile of a sinusoidal SRG with the properties described above is illustrated in Figure 1.1.

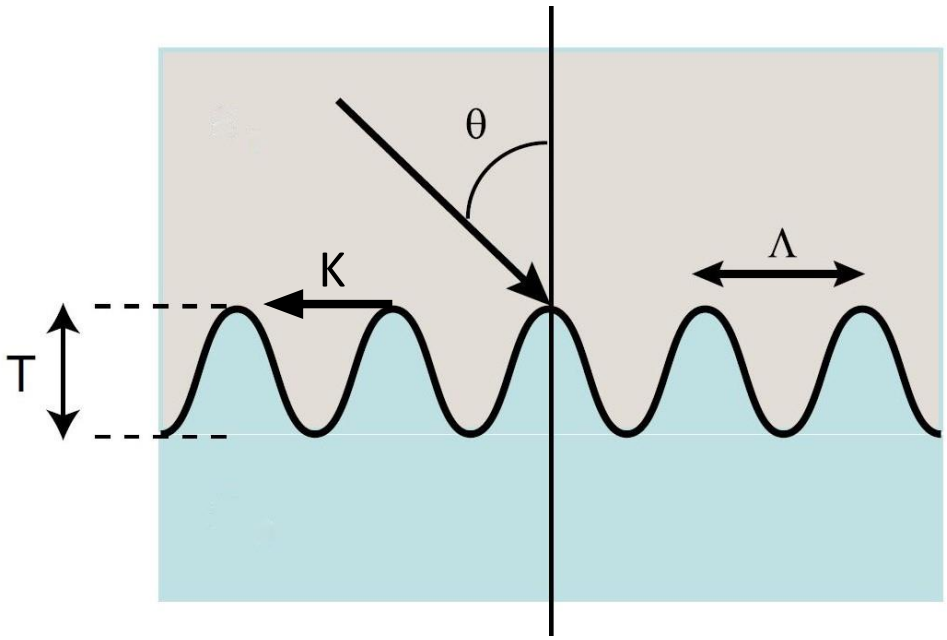

Figure 1.1 Sinusoidal surface relief diffraction grating profile. T represents the grating modulation depth, Λ is the grating pitch, θ is the angle of the incident light, and K is the grating vector [4].

A SRG is said to be uniform when the grating vector remains constant across the entire grating. For non-uniform SRGs, the grating vector gradually changes direction across the grating's surface. A grating exhibiting non-uniformity in its pitch, meaning that the grating pitch value does not remain constant, is referred to as having

a chirped pitch. Gratings with a chirped pitch can either exhibit a pitch value increase from one edge to the opposite edge, or from the edges to the center.

The fundamental property of a uniform diffraction grating is that it will diffract light into what are known as diffraction orders. This phenomenon can be explained using the grating equation [1].

$$\Lambda(\sin(\theta_m) - \sin(\theta_i)) = m\lambda \tag{1.1}$$

In Equation (1.1), the diffracted angle of light is represented by θ_m, the incident light angle is represented by θ_i, the wavelength of the incident light is λ and the grating pitch is Λ. The final term, m, represents the order of diffraction. Since this expression is periodic in nature, a single incidence angle could yield multiple diffraction orders [1]. The angular positions of these diffraction orders can be calculated by controlling the basic properties of the grating in fabrication and therefore have a number of applications, which will be elaborated on later in the introduction. Further analytic [5] and numerical [6], [7] approaches have been developed since the 1930s to accurately model the properties of light while interacting with a SRG surface, but will not be discussed in this thesis.

1.2 Diffraction Grating Fabrication Methods

Many techniques have been developed to produce stable and efficient surface relief gratings using a variety of different materials. Inscription methods can be classified under two primary categories: top-down inscription and bottom-up fabrication [8]. Top-down inscription refers to a technique where an external force is applied to the material's surface to cut, imprint, or irradiate the SRG structure onto the desired material. Some examples of this technique include chemical grating fabrication, mechanical etching, and laser inscription, which will be discussed throughout this section. Bottom-up grating fabrication refers to techniques in which the material is deposited in layers or the molecules are arranged at an atomic level to form desired structures. Examples of this technique include atomic layer deposition [9], [10], molecular self-assembly [11], and DNA-scaffolding [12], [13]. Only top-down inscription techniques will be further elaborated on as they are the most commonly used and reflect the fabrication approach taken for the non-uniform SRG fabrication in this thesis.

1.2.1 Chemical SRG Production Method

The least common of the three top-down grating production methods outlined above is that of chemical grating fabrication. This method induces surface deformations resulting from surface buckling effects in a poly(dimethylsiloxane)

(PDMS) thin film [14], [15]. The buckling is caused by applying linear stress on a selected axis in the material, then exposing the surface to an oxygen plasma, causing the film to heat and oxidize. The oxidation process causes the formation of a thin silicate layer on the surface of the film. The duration of oxidation in this process and consequentially the thickness of the silicate, will influence the pitch of the SRGs formed on the PDMS film.

Once the predetermined exposure time is reached, the stress is removed, and the silicate surface buckles, forming a sinusoidal SRG. The exposure times necessary for this process range from 10 seconds to 30 minutes and SRGs with pitches between 0.5 and 10 μm can be fabricated. The depth of the gratings formed using this method are reported to be between 20 nm to 1000 nm [14]. This process has been proven to produce constant pitch [14] and chirped pitch gratings [15]. The control over the surface gratings orientation on the PDMS surface appears however to be strictly local, as the pattern across larger surface areas seems to be chaotic in nature [16].

The greatest drawback from this fabrication technique is the control over the grating parameters. Although localized grating formation exhibits properties of linear and chirped SRGs, the chaotic nature of the gratings across larger surface areas does not allow for the production of SRGs comparable in size to those that can be produced using other methods. The multi-step process of this method also hinders the simplicity and efficiency of this production technique.

1.2.2 Mechanical SRG Inscription Method

The second common top-down SRG fabrication technique is mechanical etching. Mechanical etching uses the principle of applying a precise force to physically cut a grating into a material's surface. One method that has been developed to perform mechanical etching is known as scanning probe lithography which uses a modified diamond tip in an Atomic Force Microscope (AFM) to apply pressure to the surface of an aluminium substrate [17]. The applied pressure is adjusted so as to deform the material's surface and is then dragged across it to inscribe the grating structure. This technique is able to inscribe uniform gratings at a rate of 10 μm/s. This process provides great three-dimensional control over the inscription process and can be used for inscribing any number of patterns or images into a material's surface. The primary drawbacks of this approach however are the slow inscribing times due to the speed constraints of the AFM tip as well as the short lifespan of the diamond tip resulting from clogging due to residue from the etching process and tip degradation.

Applying the same principles as scanning probe lithography, a process known as diamond turning has been developed and employed to expedite mechanical

SRG production [18]. This technique employs a Single Crystal Diamond (SCD) tool to cut periodic SRGs into a material's surface. The tool is fabricated using a focused ion beam sputtering technique. The periodic grating section of the SCD tool is cut from the edge of a diamond chisel piece, to construct the desired pitch and depth. This process produces a grating inscription tool with up to 10 nm accuracy which can then be used to mechanically cut SRGs into a material's surface. The limitation to this technique is that the SCD tool can only be used to inscribe an SRG with the pitch, depth, and width properties attributed to the tool itself. Therefore, for each new grating with more complex geometries, or varying surface properties, a new tool must be fabricated.

The final top-down mechanical SRG production technique that will be discussed is contact imprinting [19]. This technique uses elastomeric stamps, typically made of PDMS, to imprint a grating structure onto silicon wafers and metal substrates. Approximately 0.3 MPa of pressure is applied to the elastomeric stamp once in contact with the substrate surface. The applied pressure can be varied in order to cause a deformation of the PDMS to produce hollow structures, such as rings or trenches instead of dots or square gratings, or a backbone can be added to prevent any deformation [19].

1.2.3 Laser SRG Inscription Method

The most common method used in SRG fabrication is laser inscription. Laser inscription can be further classified into two main categories, the first of which is ion beam patterning. Ions can be applied to a material's surface in two primary ways to further control the properties of the fabricated SRG. Nano-optical patterns can be written by irradiating a material's surface through a dielectric stencil [20]. This uses what is referred to as a mask, a dielectric wafer with a nano-pattern previously cut out, to govern the section of the sample to be irradiated. The ion beam will irradiate the sample surface only through the section of the mask that has been cut out, boring a grating or hole pattern into the material where it is incident on the sample's surface. The second technique is known as Focused Ion Beam (FIB) patterning, which has been applied in the fabrication of nano-hole arrays as well as grating patterns used for micro optical apparatuses. FIB patterning accelerates ions from a source and focuses them at one point on the material [21]. The recombination of this ion source (typically a Ga^+ ion) with a separate electron beam from a scanning electron microscope generates a focused beam of accelerated particles, the diameter of which governs the resolution of the inscribed SRG. Using this technique, it is possible to write a grating or a nano-array into the sample's surface by controlling the position of the ion beam and etching each component of the desired SRG individually [22]. This technique can control the size of the features produced across

small surface areas, which can, in future processing steps, be used to create more intricate optical devices and nano-systems [23].

The second laser technique used in optical patterning is laser lithography. Laser lithography operates by generating an optical pattern using either an interference pattern or a dielectric mask [24]. This pattern is then projected onto the surface of a photoresist or a photomechanical material, such an azobenzene-derivative material, and optically imprinted. In masked laser lithography, the dielectric mask is positioned between the laser beams source and the sample surface [25]. Using lenses, the size of the pattern produced from the mask may be controlled to imprint smaller scale patterns on the azo-film, however it is not required as many masks used in the production of grating patterns are cut prior to grating inscription with the desired width and grating pitch. Mask-less lithography produces an interference pattern from the recombination of two coherent laser beams instead of using a dielectric mask [26]. The interference pattern produced is incident on an azobenzene thin film and is optically imprinted into the sample. This method has proven to be effective not only in the production of uniform gratings, but also in the production of periodic nano-arrays and three-dimensional patterns using between two and four interfering lasers irradiating in measured bursts [27].

Although mask-less laser lithography is limited in that it can only inscribe patterns that can be produced either by the interference of the incident laser beams, it was selected for the production of non-linear SRGs in this thesis because it is efficient, cost effective, and provides a single step fabrication process.

1.3 Azobenzene Thin Films

A useful and effective material when inscribing SRGs using laser lithography is azobenzene derivatives. A basic azobenzene molecule is two nitrogen atoms bound to two benzene rings. This molecule undergoes a *trans-cis* photoisomerization cycle when irradiated by an incident laser beam [28]. This means that when exposed to an irradiating beam, the azobenzene molecules will move away from the areas of high irradiance into the darker regions of the interference pattern [29]. Applying this concept, it becomes clear that by using a laser to irradiate an azobenzene substrate with a controlled interference pattern, it is possible to produce a grating in the azobenzene film in the configuration of the interference pattern. An illustration of the azobenzene molecule and its *trans* and *cis* configurations are shown in Figure 1.2.

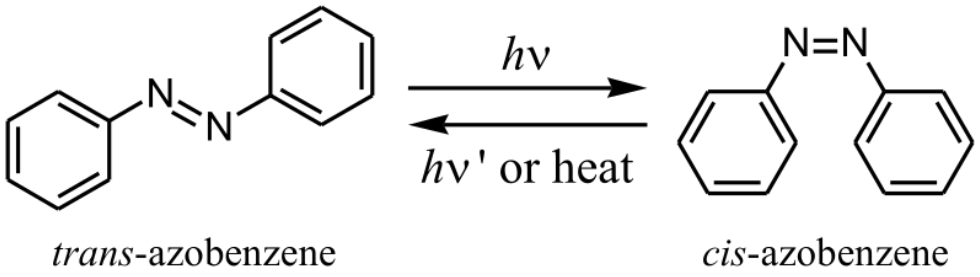

Figure 1.2: Illustration of the *tran-cis* photoisomerization cycle process undergone by azobenzene when exposed to a highly irradiating beam [30].

This technique has been heavily used in the production of linear diffraction gratings for at least the last 23 years [31], [32] however there is the constant motivation to improve the azobenzene film by binding the azobenzene chromophore with different backbones [33]. The formation of a SRG in an azobenzene thin film is also notably influenced by the polarization and wavelength of the incident light. The optimal wavelength for inscription is the absorption wavelength of the film [34], whereas circularly polarized light was determined to be the optimal polarization [35].

Recently, a research group from Queen's university and the Royal Military College have developed an azobenzene chromophore with a mexylamiontriazine backbone [36]. The combination is referred to as Disperse Red 1 Molecular Glass (gDR1), and has been shown to produce high quality thin films with a larger absorption bandwidth and a much easier synthesis and higher yield than their previously-used azo-polymer counterparts. Therefore, the gDR1 molecule was selected as the azobenzene chromophore used in the inscription of the non-uniform SRGs produced in this thesis.

1.4 Diffraction Grating Applications and Recent Developments

Diffraction gratings have several applications in industry and research alike. Possibly the most notable application has been their incorporation into waveguides and integrated optical systems. Their ability to diffract light at specific frequencies, determined by their grating pitch, has allowed for control over the mode coupling and decoupling of excited electromagnetic energy in waveguides [37]. Consequentially, diffraction light filters can be specifically designed to match the band-rejection requirements for a specific waveguide. Typically, the inscription process for SRG diffraction filters in waveguides has been accomplished using ion beam etching [38]. It has been shown however that the inscription of the SRG diffraction filter on an azobenzene film has been successfully implemented in integrated optical systems [32]. The technology has recently been further developed by superimposing multiple diffraction gratings on an SRG diffraction filter to more

precisely control the photonic bandgap in a slab waveguide [39]. In addition to their incorporation into waveguides, the SRG diffraction filters have been integrated into optical fiber cables [40]. By heating the SRG, without erasing the grating pattern, a tunable control system has been developed to control the grating pitch in-situ and, in turn, control the allowed frequencies. The successful application of the azobenzene layer and consequential grating inscription for mode coupling in slab waveguides shows that the single step and cost-effective method used for non-uniform grating inscription in this thesis is a reliable and stable SRG production method for industry.

The application of optical diffraction filters is far more diverse than simply controlling the modes of propagating electromagnetic waves in waveguides and optical fibers, with new applications constantly being discovered. In research, diffraction gratings are being used for second harmonic diffraction in non-linear optics and restricting dispersion or laser light from sub-wavelength apertures [41], [42]. Reflective diffraction gratings are also applied in laser systems for the purposes of pulse compression, which can be achieved using the first diffracted order of a SRG [43]. The diverse applications of diffraction gratings also extend to satellite systems, where an echelle (saw-tooth) style diffraction grating is used for information processing of spectral data [44], as well as medical research, where diffraction filters are used as sensors to monitor neural response in the visual cortex [45]. Because of this diverse set of applications, there is ongoing development and research focused on producing more robust SRGs that maintain high diffraction efficiencies after lengthy continuous laser exposures [46], as well as reducing polarization loss while improving diffraction efficiency at higher diffracted orders [47].

An area of particular interest for SRG application is in the area of surface plasmonics. As optical systems have become more refined and are able to produce nanostructures, various applications in physics, as well as chemistry, computer engineering, and even biology are becoming apparent [48]. Surface plasmon waves are defined as being electromagnetic excitations that propagate outward two-dimensionally from their induction point [49]. There are three methods used to induce surface plasmons in a conductive surface: prism coupling using total internal reflection [50], the introduction of metallic surface inhomogeneities to cause light scattering [51], and the application of periodic grating structures [52]. The nanostructures that are being created in modern optics allow not only for the excitation of surface plasmon polaritons and waves, but also permit measurable control over the way they behave [48]. Recent research conducted by Prof. Sabat's research group at RMC has shown that it is possible to not only produce chirped pitch SRG structures on azobenzene molecular glass using a cylindrical lens, but, by

sputter coating these SRGs with a layer of silver, the bandwidth of allowable wavelengths contributing to surface plasmon induction is increased [53].

1.5 Research Goal and Application

The goal of this thesis is to describe an experimental method of non-uniform SRG fabrication on the surface of azobenzene molecular glass thin films and validate the experimental process by comparing the results to theoretical models produced analytically. The method described herein produces SRGs by introducing a spherical lens to diffract the light in one half of a Lloyd's mirror interferometer onto an azobenzene molecular glass thin film. The interference pattern produced by the recombination of the two laser beams introduces a non-uniformity in two dimensions. This non-uniformity produces a changing grating vector direction along the grating vertical axis, and a chirped pitch along the grating horizontal axis.

This method provides a fabrication technique that allows for control of the grating properties across the entire surface of the SRG by varying the lens position during the inscription process and by varying the grating's central pitch. The need for non-uniform diffraction gratings has arisen recently with new developments in plasmonics and its applications to solar technology [54]. Many of the techniques discussed in Section 1.2 allow for the production of uniform chirped pitch SRGs. There is also the documented production of circular gratings with both constant and chirped pitch using a similar direct laser interference patterning technique to what will be described herein [55], [56].

In this thesis, the results from non-uniform SRG inscription using a spherical lens are shown. The resulting grating pitch, vector direction, and modulation depth profiles are compared between non-uniform gratings written at central pitches of 500 nm, 1000 nm, 1500 nm, and 2000 nm, as well as non-uniform gratings written at three lens positions of 35 mm, 45 mm, and 55 mm with respect to the azobenzene surface during the writing process. The localized grating pitch, vector orientation and modulation depth for the fabricated non-uniform gratings are measured experimentally using an AFM. A theoretical model is also developed and compared to the experimental results. The results presented herein are the first instance in published literature where non-uniform SRGs have been fully characterized both experimentally and analytically using a method that provides precise control over every parameter contributing to diffraction across the SRG surface.

1.6 Structure of the Thesis

This thesis will be composed of five chapters. Chapter 1, the introduction, begins by discussing the basics properties of diffraction gratings and surface relief grating structures. It goes on to discuss three primary top-down methods of surface

relief grating inscription – chemical buckling, mechanical etching, and laser inscription – and discusses the benefits and drawbacks of each, as well as some applications of surface relief gratings in both industry and research. Then, the introduction outlines the properties of azobenzene materials and their applications to SRG inscription, focusing on the azobenzene molecular glass derivative used in the inscription of the non-uniform SRGs discussed in this thesis. Finally, the research goals, motivation, and thesis outline are provided.

Chapter 2 contains the derivations and theory required for the experimental production and analytic model of the non-uniform surface relief gratings. It derives the expression for the interference phase of the recombined laser light used to write uniform SRGs, and, from that, produces the expression for grating central pitch from Maxwell's equations. Then, from the divergence of light resulting from the introduction of a spherical lens, it geometrically derives the expression for the non-uniform light interference phase used to write the SRGs discussed in this thesis. This chapter also outlines the procedure used to produce the hypothetical SRGs analytically, and the steps and considerations taken to program the analytic model.

Chapter 3 provides an overview of the experimental procedure used to create the non-uniform SRGs. It describes the steps taken to prepare the sample with the azobenzene thin film. The Lloyd's mirror interferometer set-up is described in detail, and the optical system used to control the laser beam properties is explained. Finally, the experimental grating analysis process is explained.

Chapter 4 provides the results from experimental grating inscription and the results from the analytic grating model. It will also present the results of the depth distribution analysis from the inscribed SRGs and compare them to a hypothetical irradiance distribution across the sample's surface. A comparison between the analytic distributions and experimental SRGs will be conducted, and will highlight the distribution of the pitch, vector orientation, and modulation depth across the grating surface in both cases.

Finally, Chapter 5 provides a summary of the results shown in the previous section and concludes the thesis.

Chapter 2 Theoretical Background

2.1 Maxwell's Equations and the Properties of Light

The study of optics and photonics at its most fundamental level is the application of electromagnetic theory to describe the properties of radiation in the forms of infrared, visible, ultraviolet, or x-ray light. Consequentially, the background theory necessary for modelling the inscription of the non-uniform SRGs described in the following chapters can be derived from Maxwell's four equations, as follows:

$$\nabla \cdot \boldsymbol{E} = \frac{1}{\epsilon_o}\rho \tag{2.1}$$

$$\nabla \cdot \boldsymbol{H} = 0 \tag{2.2}$$

$$\nabla \times \boldsymbol{E} = -\mu_o\left(\frac{\partial \boldsymbol{H}}{\partial t}\right) \tag{2.3}$$

$$\nabla \times \boldsymbol{H} = \boldsymbol{J} + \epsilon_o\left(\frac{\partial \boldsymbol{E}}{\partial t}\right) \tag{2.4}$$

Where $\boldsymbol{E}$ is the electric field vector, $\boldsymbol{H}$ is the magnetic field vector, μ_o is the permeability of free space, ϵ_o is the permittivity of free speace, $\boldsymbol{J}$ is the volume current density, and ρ is the volume charge density. Maxwell's first equation, known as Gauss's Law, describes the total electric field produced by all bound and free charges present in a dielectric medium. Maxwell's second equation, although not having a formal name, proves that the divergence of any magnetic field is always equal to zero. This explicitly states that a monopole is impossible, as every unhindered magnetic field must form a closed loop. Maxwell's third equation, known as Faraday's law shows that a changing magnetic field will induce an electric field. Finally, Maxwell's fourth equation, known as Ampere's law, was initially derived by Ampere and showed how the free current density in a closed loop was related to the magnetic field it induced. In order to preserve the continuity equation, Maxwell made a correction to Ampere's law by adding the second right hand term in Equation (2.4) which, in addition to free current, takes into account what is known as displacement current [57].

The four equations explained above explicitly outline the behaviour of all electromagnetic radiation through any media. For the work outlined in this chapter, only the case of light propagating through air and interacting with mediums approximated as perfect insulators will be considered. The versions of Maxwell's equations to be used in the following derivations are therefore presented as:

$$\nabla \cdot \boldsymbol{E} = 0 \tag{2.5}$$

$$\nabla \cdot \boldsymbol{H} = 0 \tag{2.6}$$

$$\nabla \times \boldsymbol{E} = -\mu_o \left(\frac{\partial H}{\partial t}\right) \tag{2.7}$$

$$\nabla \times \boldsymbol{H} = \epsilon_o \left(\frac{\partial \boldsymbol{E}}{\partial t}\right) \tag{2.8}$$

Maxwell's first equation is now simply equal to zero because there is no charge density present in air. Maxwell's second and third equations remain unchanged. Finally, the total volume current density term in Maxwell's fourth equation becomes zero as there is no conductive loop through which current is flowing to produce a magnetic field, and therefore the only term remaining is Maxwell's correction.

From Equations (2.5)-(2.8), the properties of laser propagation can be derived. In the following sections, Maxwell's equations will be used to generate the fundamental characteristics of the electric and magnetic field components of a propagating electromagnetic wave. These properties are essential to characterizing the irradiance profile of a laser beam, which will be used to develop a theoretical model of the SRG depth distribution. The expression for the interference pattern used to fabricate the non-uniform SRGs will also be derived using the phase difference between two interfering laser beams. The method developed to apply the equations produced herein in order to generate a theoretical model of non-uniform SRGs will also be discussed.

2.2 Light as a Wave

The general properties of a laser beam propagating in a vacuum can be derived using Maxwell's four equations. First, a theoretical laser beam will be assumed to be propagating along the Z-axis in a three-dimensional reference frame. The hypothetical laser beam will be collimated and linearly polarized along the vertical. An illustration of an electromagnetic wave exhibiting these characteristics is shown in Figure 2.1.

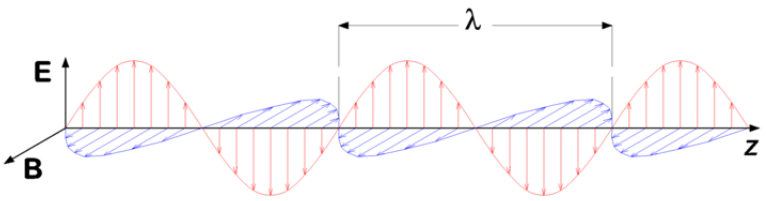

Figure 2.1 A linearly polarized electromagnetic wave propagating along the Z-axis with a wavelength of λ.

Beginning with Maxwell's equations, two partial differential equations for the electric and the magnetic vector fields can be derived. These partial differential equations were obtained by taking the curl of Faraday's and Ampere's laws and are expressed as follows [58]:

$$\nabla^2 \boldsymbol{E} = \mu_o \epsilon_o \left(\frac{\partial^2 \boldsymbol{E}}{\partial t^2} \right) \tag{2.9}$$

$$\nabla^2 \boldsymbol{H} = \mu_o \epsilon_o \left(\frac{\partial^2 \boldsymbol{H}}{\partial t^2} \right) \tag{2.10}$$

The wave equations seen above are known as Helmholtz's equations and describe the general propagation of the electric and magnetic components of electromagnetic radiation.

In wave mechanics, the equation of a generalized traveling wave takes the form of [59]:

$$\frac{\partial^2 y}{\partial t^2} = v^2 \left(\frac{\partial^2 y}{\partial x^2} \right) \tag{2.11}$$

Where v is the wave's velocity. Comparing Equation (2.11) to Equations (2.9) and (2.10), it is shown that the velocity of an electromagnetic wave in a vacuum is simply:

$$v = \frac{1}{\sqrt{\mu_o \epsilon_o}} \cong 3.00 \times 10^8 \, m/s = c \tag{2.12}$$

Where c is the speed of light.

Another property of sinusoidal waves is the wave number, which is inversely proportional to the wavelength of the propagating wave by a factor of 2π. When a direction is associated with the propagating wave, the wave number can be expressed as a vector, known as the wave vector, and has direction parallel to the direction of propagation. The general expression for the wave vector is:

$$\boldsymbol{k} = \frac{2\pi}{\lambda}\hat{\boldsymbol{n}} \tag{2.13}$$

Where $\boldsymbol{k}$ is the wave vector, λ is the wavelength of the propagating electromagnetic wave, and $\hat{\boldsymbol{n}}$ is the direction of propagation.

The expression of electromagnetic radiation as a wave can be used to derive the basic properties of a single wavelength laser. The laser beam can be modeled as a sine wave with the direction of propagation for this example selected to be in the Z direction. From Equations (2.9) and (2.10), the solutions for the electric and magnetic fields are complex and are expressed in the following form:

$$\widetilde{\boldsymbol{E}}(z,t) = \widetilde{\boldsymbol{E}}_o e^{i(kz-\omega t)} \tag{2.14}$$

$$\widetilde{\boldsymbol{H}}(z,t) = \widetilde{\boldsymbol{H}}_{\boldsymbol{o}} e^{i(kz-\omega t)} \tag{2.15}$$

Where $\widetilde{\boldsymbol{E}}(z,t)$ and $\widetilde{\boldsymbol{H}}(z,t)$ are the complex forms of a monochromatic sine wave propagating in the Z-direction, and $\widetilde{\boldsymbol{E}_o}$ and $\widetilde{\boldsymbol{H}_{\boldsymbol{o}}}$ are the respective complex amplitudes. The k and ω terms are the wave number and laser angular frequency respectively. By employing Maxwell's equations, it can be shown that neither the electric or magnetic field amplitude can be in the direction of propagation without disobeying Equations (2.5) and (2.6). This asserts that electromagnetic monochromatic waves must be transverse in nature.

Another property of electromagnetic waves, that will be employed in Sections 2.3 and 2.4, is derived through the application of Equations (2.14) and (2.15) to Equation (2.7). By solving Faraday's law, it is shown that the magnetic and electric components are, in addition to being transverse, orthogonal to each other. Therefore, if the electric field component of an electromagnetic wave propagating in the Z-direction is oscillating along the X-axis, the magnetic field component will always be oscillating along the Y-axis. In addition, it shows that the magnitudes of the electric field and magnetic field components of an electromagnetic wave are proportional by a constant of $\frac{\mu_o}{c}$. Therefore, the general forms of the complex components of a monochromatic plane wave are expressed as:

$$\widetilde{\boldsymbol{E}}(\boldsymbol{r},t) = \tilde{E}_o e^{i(\boldsymbol{k}\cdot\boldsymbol{r}-\omega t)}\hat{\boldsymbol{l}} \tag{2.16}$$

$$\widetilde{\boldsymbol{H}}(\boldsymbol{r},t) = \frac{\mu_o \tilde{E}_o}{c} e^{i(\boldsymbol{k}\cdot\boldsymbol{r}-\omega t)}\left(\hat{\boldsymbol{k}}\times\hat{\boldsymbol{l}}\right) \tag{2.17}$$

Where $\hat{\boldsymbol{k}}$ is the direction of the wave vector. The complex wave forms provide an encompassing view of how the electromagnetic wave propagates through air. In the following derivations however, only the real parts of the electric and magnetic field components are required. Taking the real parts of Equations (2.16) and (2.17), the resulting expressions for the electric and magnetic field components become:

$$\boldsymbol{E}(\boldsymbol{r},t) = E_o \cos(\boldsymbol{k}\cdot\boldsymbol{r}-\omega t+\psi)\,\hat{\boldsymbol{l}} \tag{2.18}$$

$$\boldsymbol{H}(\boldsymbol{r},t) = \frac{\mu_o E_o}{c}\cos(\boldsymbol{k}\cdot\boldsymbol{r}-\omega t+\psi)\left(\hat{\boldsymbol{k}}\times\hat{\boldsymbol{l}}\right) \tag{2.19}$$

Where ψ represents a possible applied phase shift that can imposed to the wave. In the following sections however, the phase shift applied to both the electric and magnetic fields will be zero.

2.3 Laser Irradiance and Power

As outlined in Section 2.1 and Section 2.2, the laser used for the inscription of SRGs can be modeled as an electromagnetic wave propagating along a defined optical axis. The energy contained within an electromagnetic wave is directly related to both the electric and magnetic field components through what is defined as the Poynting vector [58]. The Poynting vector is defined as the energy per unit area per unit time stored in the laser beam and is shown to be:

$$\boldsymbol{S} = (\boldsymbol{E}\times\boldsymbol{H}) \tag{2.20}$$

Where $\boldsymbol{S}$ is the Poynting vector, $\boldsymbol{E}$ is the electric field vector, and $\boldsymbol{H}$ is the magnetic field vector. A correlation can be made between the Poynting vector and the laser's irradiance, which is defined as the time averaged energy per unit area per unit time. The irradiance can be expressed in terms of the Poynting vector as follows [3]:

$$I = \langle|\boldsymbol{S}|\rangle \tag{2.21}$$

Applying Equations (2.18) and (2.19) to the above expression, and expanding out the terms, the irradiance can be written as:

$$I = |\boldsymbol{E_o} \times \boldsymbol{H_o}|\langle \cos^2(\boldsymbol{k} \cdot \boldsymbol{r} - \omega t)\rangle \tag{2.22}$$

The time average of the square of a cosine function is simply ½. Therefore, in the case of a monochromatic plane wave, the irradiance is directly proportional to the magnitude of the electric and magnetic field vectors. By applying Equation (2.19), which defines the relationship between the magnetic field vector magnitude and the electric field vector magnitude, the irradiance expression becomes:

$$I = \frac{1}{2} E_o \left(\frac{\mu_o}{c}\right) E_o \tag{2.23}$$

After simplification, the final form of the irradiance from a single beam can be expressed as:

$$I = \frac{1}{2} \epsilon_o c E_o^2 \tag{2.24}$$

2.4 Laser Recombination and Interference Patterns

The mask-less inscription of a SRG onto an azobenzene surface is done by generating an interference pattern with a laser. The method chosen to achieve this was the application of a Lloyd's mirror interferometer, as shown in Figure 2.2.

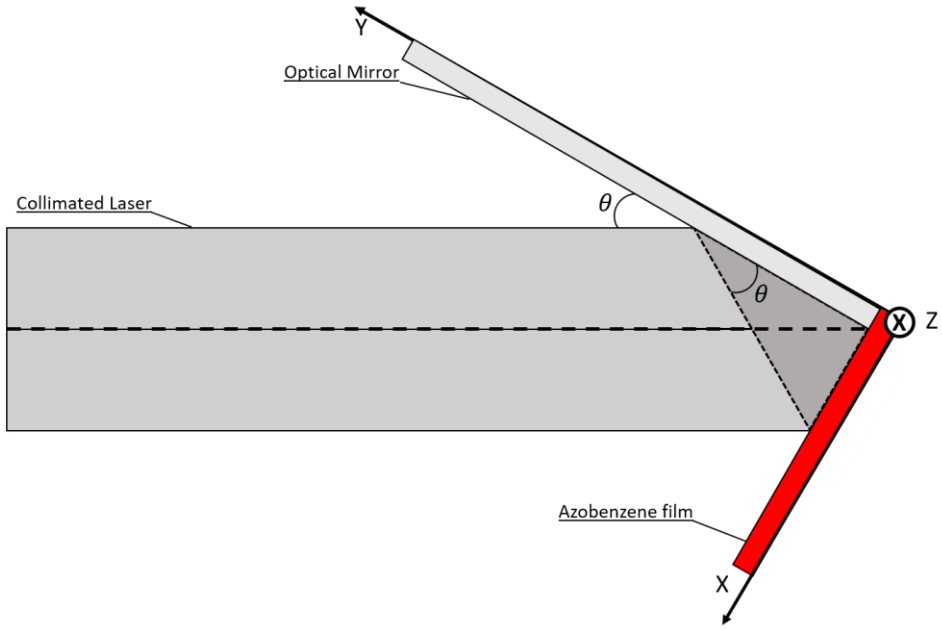

Figure 2.2: Illustration of a collimated laser beam irradiating the surface of an azobenzene film using a Lloyd's mirror interferometer. A Cartesian coordinate system is established with respect to the interferometer.

This set-up generates an interference pattern by producing a path length difference between two halves of the collimated laser beam. To do so, an azobenzene film is positioned at 90° with respect to an optical mirror, with half of a laser beam directly irradiating the surface of the film and half being reflected off of the mirror. The angle between the optical axis and the mirror's surface is defined as θ. The two halves of the beam perfectly overlap on the surface of the film. The varying optical path length difference between the two beams generates an interference pattern on the azobenzene film. The interference pattern is characterized by the phase difference of the two beams.

The reference frame for the Lloyd's mirror interferometer was established using a Cartesian coordinate system. The X-Z plane is defined as being the surface of the azobenzene film and the Y-axis is parallel to the optical mirror, as shown in Figure 2.2. The origin has been set to be the center of the Lloyd's mirror interferometer along the intersection axis of the optical mirror and the azobenzene surface. For simplicity, this will be referred to as the sample reference frame.

2.4.1 Recombined Irradiance

Deriving the total irradiance of the interfering laser beams is accomplished by starting with the expression for the irradiance shown in Equation (2.21). As seen in Section 2.2, the relationship between the magnetic and electric components of a propagating electromagnetic wave allow for the substitution of the magnetic field vector with that of the electric field vector, and provide an equation for the total irradiance as follows:

$$I_T = \epsilon_o c \langle E_T \cdot E_T \rangle \tag{2.25}$$

Where I_T is the total laser irradiance and E_T is the total real part of the electric field vector component of the electromagnetic wave. The expression of the electric field vector contributing to the irradiance in Section 2.3 was for a single electric field as emitted from the source. However, since the interfering beams are treated as independent sources, the total electric field is comprised of two parts. The irradiance equation therefore becomes:

$$I_T = \epsilon_o c \langle (\boldsymbol{E_1} + \boldsymbol{E_2}) \cdot (\boldsymbol{E_1} + \boldsymbol{E_2}) \rangle \tag{2.26}$$

The two electric field vector terms, E_1 and E_2, are the electric fields of the laser beam incident on the azobenzene film and the beam reflected off the mirror respectively. The product of the electric fields seen in Equation (2.26) can be expanded into three terms. The result is shown as follows:

$$I_T = I_1 + I_2 + I_{12} \tag{2.27}$$

The three terms seen in Equation (2.27) can be identified as the three components of the irradiance from two coherent laser beams. The first term, I_1, is simply the irradiance from the direct beam on the surface being irradiated. The second term, I_2, is the irradiance term being reflected from the mirror to overlap the incident beam. Finally, the third term, I_{12}, is a combination of the electric field components from both beams and is known as the interference irradiance. The expressions for the first two irradiance terms have already been solved in the previous section since they are simply the irradiance from a single beam and are given as follows:

$$I_1 = \frac{1}{2}\epsilon_o c E_{o1}^2 \tag{2.28}$$

$$I_2 = \frac{1}{2}\epsilon_o c E_{o2}^2 \tag{2.29}$$

Where E_{o1} and E_{o2} are the amplitudes of the electric field vectors for the directly irradiating laser and the reflected laser respectively. The expression for the interference irradiance requires further derivation as it is a function of the electric field vectors of both beams as seen below:

$$I_{12} = 2\epsilon_o c\langle \boldsymbol{E_1} \cdot \boldsymbol{E_2} \rangle \tag{2.30}$$

Solving the time average of the expression in Equation (2.30) produces the following result for the interference irradiance:

$$I_{12} = \epsilon_o c E_{01} E_{02}(\cos(ks_1)\cos(ks_2) + \sin(ks_1)\sin(ks_2)) \tag{2.31}$$

Where s_1 is the path length traveled by the directly irradiating laser beam, and s_2 is the path length traveled by the reflected laser beam. Using the double angle formula, Equation (2.31) can be further simplified. The result combines all the phase information from both laser beams into a single cosine function, giving:

$$I_{12} = \epsilon_o c E_{01} E_{02}\cos(\delta) \tag{2.32}$$

Where δ is the phase of the interference pattern produced by the two laser beams. The interference phase is defined explicitly as:

$$\delta = ks_1 - ks_2 \tag{2.33}$$

Therefore, the interference irradiance term varies periodically as the two laser beams constructively and destructively interfere. This expression can be further simplified by employing Equations (2.28) and (2.29). This allows the interference irradiance to be defined in terms of the irradiance of the two independent beams, which is shown to be:

$$I_{12} = 2\sqrt{I_1 I_2}\cos(\delta) \tag{2.34}$$

As will be shown in Section 2.4.2 and Section 2.5, the interference phase in Equation (2.34) will be used to generate the grating profile of the non-uniform SRGs.

2.4.2 Recombined Interference Phase

In order to build the framework of the phase profile of non-uniform SRGs, the phase information of uniform constant pitch SRGs must first be derived in order to model the nature of the two interfering lasers, as well as derive the expression for the grating central pitch. The derivation given in this subsection is based on the derivation of the interference phase presented in a publication discussing the fabrication of chirped uniform SRGs [60].

For the creation of constant-pitch uniform gratings, the grating profile can be mapped by analyzing the laser beam interference across the grating surface. This is done by calculating the phase of the interference pattern, which was defined as δ in Equation (2.34). From the calculations conducted in Section 2.4.1, the interference phase is therefore expressed as:

$$\delta = \boldsymbol{k_1} \cdot \boldsymbol{r} - \boldsymbol{k_2} \cdot \boldsymbol{r} \tag{2.35}$$

Where $\boldsymbol{k_1}$ is the wave vector of the incident laser, $\boldsymbol{k_2}$ is the wave vector of the reflected laser, and $\boldsymbol{r}$ is the position vector in the sample reference frame. The position vector in a Cartesian coordinate system is:

$$\boldsymbol{r} = x\hat{\boldsymbol{x}} + y\hat{\boldsymbol{y}} + z\hat{\boldsymbol{z}} \tag{2.36}$$

The expression for $\boldsymbol{k_1}$ and $\boldsymbol{k_2}$ however have yet to be explicitly defined in the sample reference frame. These can be derived by means of a geometric analysis of the two laser beams as they interact with the azobenzene surface. An illustration of the ray trace of both wave propagation vectors is presented in Figure 2.3.

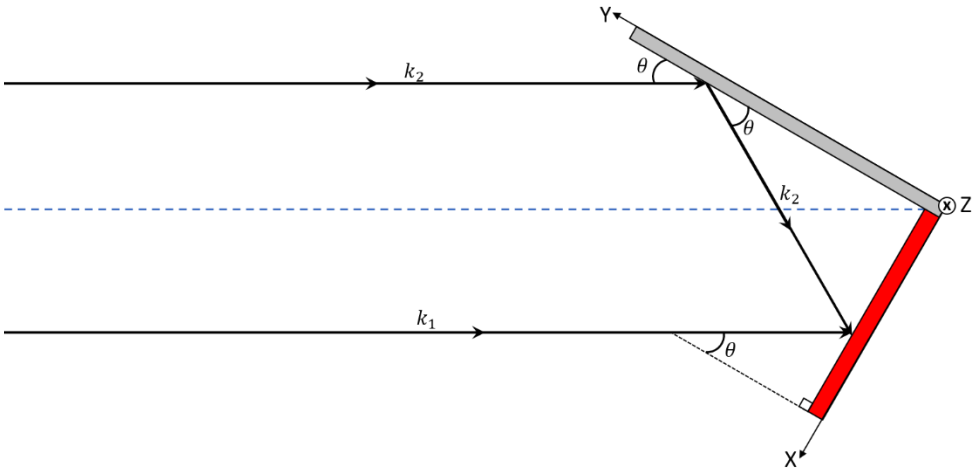

Figure 2.3: Ray-trace illustration of the interfering laser beams used in the fabrication of a uniform SRG.

From the geometry presented in Figure 2.3, the explicit forms of the wave vectors in the sample reference frame are:

$$\boldsymbol{k_1} = \frac{2\pi}{\lambda_{beam}}(-\sin(\theta)\,\hat{\boldsymbol{x}} - \cos(\theta)\,\hat{\boldsymbol{y}}) \tag{2.37}$$

$$\boldsymbol{k_2} = \frac{2\pi}{\lambda_{beam}}(\sin(\theta)\,\hat{\boldsymbol{x}} - \cos(\theta)\,\hat{\boldsymbol{y}}) \tag{2.38}$$

Where θ is the angle between the optical axis and the mirror surface, as seen in Figure 2.3. The wave vectors can be expressed using only the X-Y coordinates instead of a three-dimensional coordinate system as the phase information and the $\boldsymbol{k_1}$ and $\boldsymbol{k_2}$ vectors do not change along the Z-axis for uniform SRG inscription. This is a result of the optical path length of the laser beam being uniform along the Z-axis.

By applying Equations (2.36), (2.37), and (2.38) to Equation (2.35), the expression for the interference phase is shown to be:

$$\begin{aligned}\delta &= \frac{2\pi}{\lambda_{beam}}(-x\sin(\theta) - y\cos(\theta) - x\sin(\theta) + y\cos(\theta)) \\ &= -\frac{4\pi x}{\lambda_{beam}}\sin(\theta)\end{aligned} \tag{2.39}$$

The expression in Equation (2.39) shows the phase value of a sinusoidally periodic interference pattern. The interference phase is periodic along the X-axis, with no variation along the Z-axis.

Knowing that the interference pattern is sinusoidally periodic, the interference phase between one peak and the subsequent peak must therefore be 2π. Equation (2.39) shows that the interference phase changes along the X-axis, and therefore the distance between two subsequence peaks in the interference phase can be determined by applying an interference phase value of $\delta = 2\pi$ as seen below.

$$2\pi = -\frac{4\pi \sin(\theta)}{\lambda_{beam}}\Delta x \tag{2.40}$$

The distance measured between the grating peaks, Δx, in one period has already been defined as the grating pitch. Therefore, Equation (2.40) can be rearranged and the expression for the grating pitch of a uniform constant pitch SRG is shown to be:

$$\Lambda = \Delta x = \frac{\lambda_{beam}}{2 \sin(\theta)} \tag{2.41}$$

Equation (2.41) is also the expression used to determine the value of the central pitch of a non-uniform SRG, as the beam passing through the very center of a spherical lens experiences no path length change except that from the lens' refractive index. It will be seen in Section 2.5 that the diverging laser beam induced by the spherical lens will change the grating pitch at every value except along the path of the beam travelling directly through the center of the lens.

2.5 Non-uniform Interference Patterning

In the fabrication of chirped SRGs, external optical equipment is used to manipulate the shape and path of the laser beam. Equation (2.41) can therefore be used to model how the interference phase is altered by the addition of, in the case of the non-uniform SRGs described herein, a spherical lens. It will be shown in this section how the application of this spherical lens to the Lloyd's mirror interferometer described in section 2.4 can produce not only a chirped grating pitch, but also a curved grating vector across the SRG surface.

A spherical lens, having a focal distance of f_1, is placed in the path of the laser beam directly incident on the azobenzene film. Prior research has shown that the implementation of a cylindrical lens will generate a diverging laser beam along a single axis and, consequentially, produce a chirped grating pattern [60]. The

implementation of the spherical lens will generate a diverging laser beam along two dimensions and will introduce non-uniform patterning in the grating inscription.

All laser light that is not passing through the spherical lens that would otherwise be directly incident on the azobenzene surface is completely obstructed by an opaque material. The new set-up is illustrated in Figure 2.4 from a top and side profile.

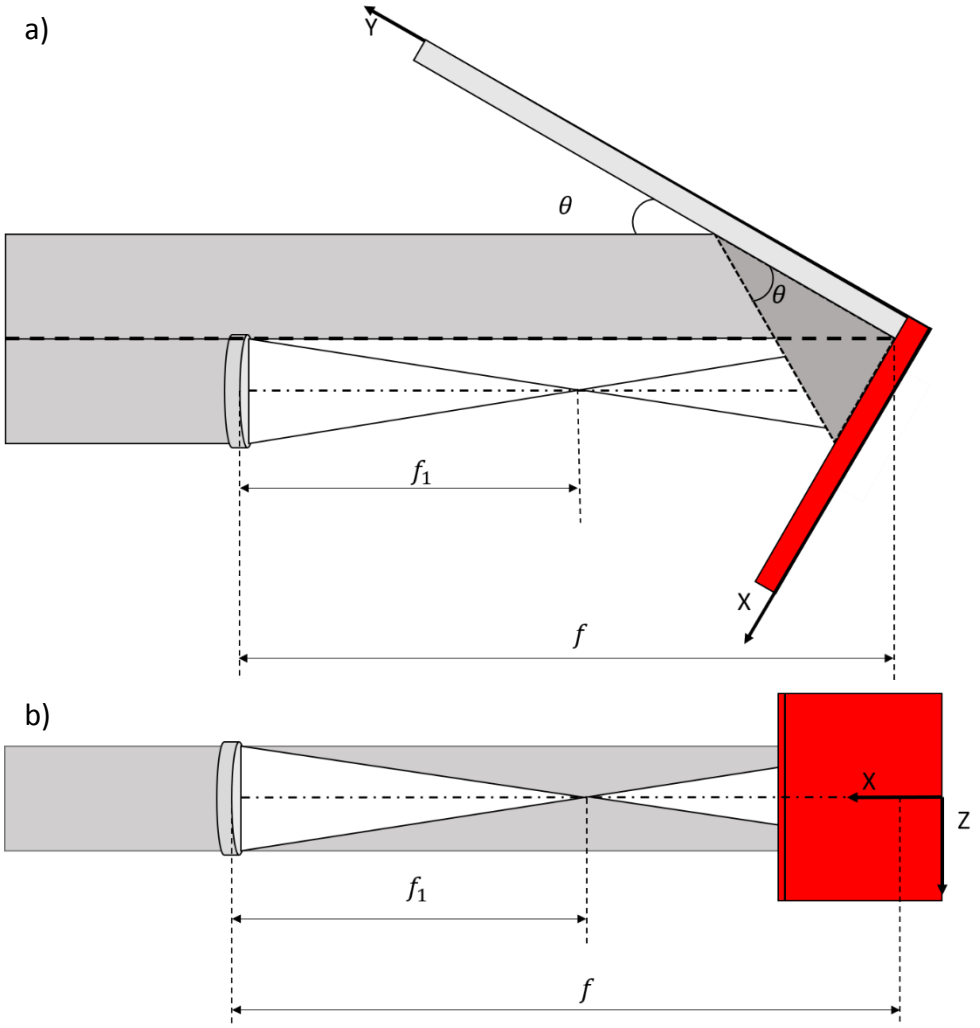

Figure 2.4: A non-uniform SRG fabrication method using a spherical lens as seen from a a) top-down profile; and b) side profile with the axes in the sample reference frame labeled.

It can be seen in Figure 2.4 that the addition of the spherical lens causes the light that would otherwise be directly incident on the azobenzene surface to diverge, forming a spherically curved wave front. The laser beam is assumed to constructively interfere at the focal point of the lens, and the path length difference can therefore be analyzed from the focal point to the azobenzene surface exclusively.

The area in which the SRG is inscribed on the azobenzene film is influenced by this alteration as well. The overlapping area is defined by the position of the spherical lens with respect to the azobenzene surface and the focal length of the lens. An example of the overlapping areas of irradiance in the case of a spherical lens being added to a Lloyd's mirror interferometer is shown in Figure 2.5.

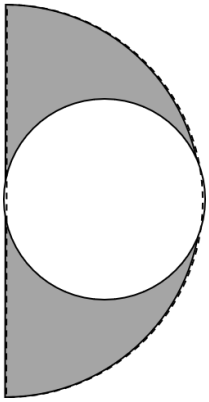

Figure 2.5: An illustration of the beam overlap using a Lloyd's mirror interferometer generated on a photoresistive surface through the introduction of a spherical lens.

The white circle represents the beam generated by the divergence of the laser passing through the lens and the grey half circle is the profile of the laser reflected from the mirror. The area in which they overlap defines the area in which the SRG is inscribed.

The spherical divergence of laser light caused by the lens produces an optical path length change for the directly incident laser beam. To account for the path length change, an extra term must be added to the interference phase equation, Equation (2.39). The interference phase with the added term is expressed as:

$$\delta = (\boldsymbol{k_1} \cdot \boldsymbol{r} + \phi) - \boldsymbol{k_2} \cdot \boldsymbol{r} \tag{2.42}$$

Where ϕ is the additional phase contribution from the change in optical path length. As it can be seen, the phase component of the laser beam reflected from the mirror onto the inscription plane is unaffected by the spherical lens.

By rearranging Equation (2.42) and applying the result given in Equation (2.39) for the unimpeded laser beam, the following expression of the interference phase was derived.

$$\delta = -\frac{4\pi x}{\lambda_{beam}}\sin(\theta) + \phi \tag{2.43}$$

The additional phase term, ϕ, can be solved geometrically using the additional optical path length created by the spherical lens. The magnitude of ϕ is defined as:

$$\phi = \frac{2\pi}{\lambda_{beam}}\Delta \tag{2.44}$$

Where Δ is the additional optical path length contributed by the divergence the laser beam due to the spherical lens. The value of Δ is therefore the unimpeded path length of the laser beam incident on the azobenzene film subtracted from the magnitude of the vector connecting the focal point to an arbitrary point on the sample surface and is shown to be:

$$\Delta = \sqrt{f(x)^2 + t(x)^2 + h(z)^2} - f(x) \tag{2.45}$$

Where $f(x)$ is the distance from the lens focal point to the surface of the azobenzene film along the optical axis, $t(x)$ is the distance along the X-axis to the selected coordinate, and $h(z)$ is the distance along the Z-axis to the selected coordinate. The functions, $f(x)$, $t(x)$, and $h(z)$, seen in Equation (2.45) are defined as follows.

$$f(x) = f - f_1 - x\sin(\theta) \tag{2.46}$$

$$t(x) = \left|x - \frac{L}{2}\right|\cos(\theta) \tag{2.47}$$

$$h(z) = |z| \tag{2.48}$$

Where f is the distance of the lens to the intersection axis of the mirror and the azobenzene film, f_1 is the focal length of the spherical lens, θ is the angle between the optical axis and mirror, and L is the width of the inscription area along the X-axis. Without the effects of the spherical lens, the optical path length to the same point would simply be $f(x)$.

The expression for the additional phase term contributed by the divergence of the laser beam from the spherical lens is therefore obtained by substituting the result for the optical path length difference into Equation (2.44). This can then be

applied to Equation (2.43) in order to obtain the complete form of the interference phase for non-uniform SRG patterning.

$$\delta = -\frac{4\pi x \sin(\theta)}{\lambda_{beam}} + \frac{2\pi}{\lambda_{beam}}\left(\sqrt{f(x)^2 + t(x)^2 + h(x)^2} - f(x)\right) \qquad (2.49)$$

The result obtained for the interference phase can be used to model the profile of a non-uniform SRG at any X-Z coordinate on the grating surface. Equation (2.49) can also be applied to the interference irradiance term in Equation (2.34), in order to model the total irradiance at any point across the grating surface.

2.6 Effects of Lens Position Variation

Due to the nature of nano-patterning, the positioning of the optical equipment can drastically influence the patterned structure. In the theoretical inscription method described in Section 2.5, the lens position within the laser beam was assumed to be perfectly centered and the distance from the azobenzene film was specified to a set integer. A misalignment within the laser beam however is possible in which a horizontal or vertical displacement of the lens position would affect the grating inscribing area and, consequentially, the interference phase. Therefore, the effects that a variation in the lens position could have on the interference phase are briefly described in this section.

The purpose of centering the spherical lens in the half of the laser beam directly irradiating the azobenzene film is to be able to assume that the lens axis – the line from the center of the lens to the surface of the film – is directly at the center of the inscription area along both the X and Z axes. Slight deviations of a distance ϵ in the spherical lens position along the X-axis will cause the overlapping beam profiles to shift horizontally, as illustrated in Figure 2.6.

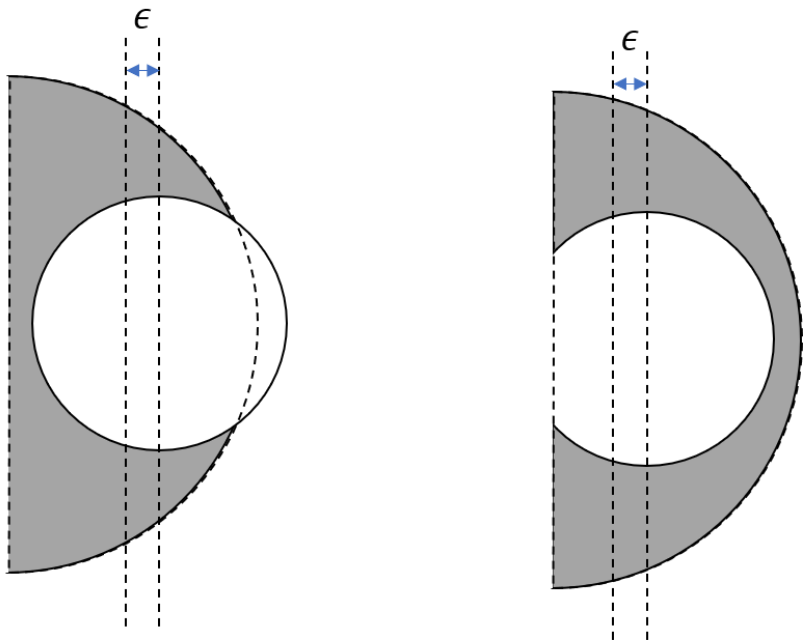

Figure 2.6: An example of the interfering laser beam profiles on the inscribing surface for a spherical lens that has been shifted along the X-axis by a distance of ϵ.

This deviation in the horizontal position of the lens would also cause a slight variation to Equation (2.49). By moving the spherical lens, the lens axis is shifted slightly to one direction by the same distance the lens has moved. Consequentially the path length difference is changed as follows:

$$\Delta = x\sin(\theta) + f_1 - f + \sqrt{(f - x\sin(\theta) - f_1)^2 + \left(\left|x - \left(\frac{L}{2} \pm \frac{\epsilon}{\sin(\theta)}\right)\right|\cos(\theta)\right)^2 + |z|^2} \tag{2.50}$$

The above equation effectively corrects for the shift in the lens axis by re-centering the center point of the diverging beam along the X-axis.

Due to the two-dimensional diverging nature of the spherical lens, a similar effect can happen along the Z-axis if the lens is placed either too high or too low with respect to the X-axis in the sample reference frame prior to inscription. The change induced in the overlapping beam profiles for a lens position variation of ϵ along the Z-axis is illustrated in Figure 2.7.

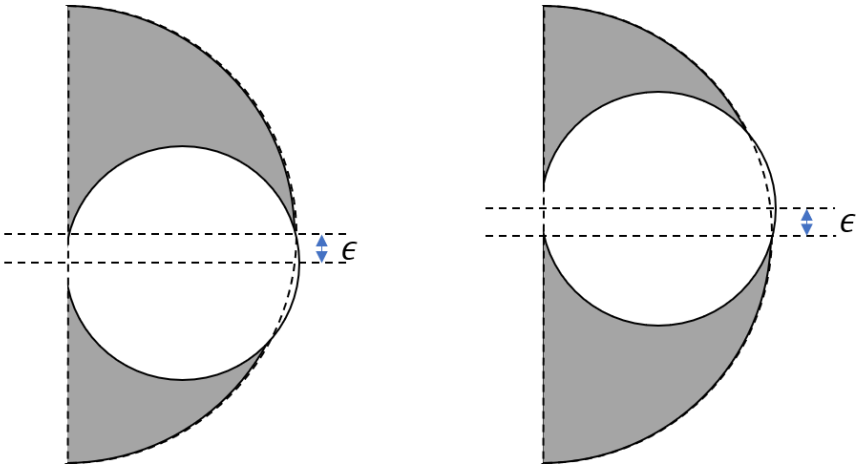

Figure 2.7: An example of the interfering laser beam profiles on the azobenzene surface for a spherical lens that has been shifted along the Z-axis by a distance of ϵ.

When the lens is moved along the Z-axis, the expression for the path length difference once again changes. The change is shown as follows:

$$\Delta = x\sin(\theta) + f_1 - f + \sqrt{(f - x\sin(\theta) - f_1)^2 + \left(\left|x - \frac{L}{2}\right|\cos(\theta)\right)^2 + |z \pm \epsilon|^2} \tag{2.51}$$

Where the position change, ϵ, of the spherical lens is shown to affect the coordinate along the Z-axis. This is once again a product of the lens axis being shifted away from the center of the inscription area. As such, the divergence of the laser beam from the spherical lens must be corrected to model the vertical position change.

2.7 Programing a Theoretical Simulation

In order to validate the theory against experimentally produced SRGs, a simulation of the grating inscription process was programed. The simulation applied the theoretical model derived in Sections 2.4 and 2.5 to predict where and how the constructive interference of the laser would inscribe patterns on the film's surface. By matching the simulation to experimental parameters, the theory and the experiment were directly compared, and the results will be shown in Chapter 4.

To generate a theoretical model, a Python script was built to simulate the experimental results by applying the same parameters used in the fabrication of non-

uniform SRGs to the theoretical expression derived for the interference phase of the overlapping lasers. As the output of Equation (2.49) is simply a phase value for a given point, an iterative calculation was written to produce a 40,000 point data matrix representing the phase values over the grating surface. The output of this program is therefore a profile map of the interference pattern at specific X-Z coordinates on the surface of a hypothetical azobenzene film.

The program simulating these grating surfaces needed to be automated to systematically generate each of the phase and irradiance values for a specified coordinate. The coordinate then needed to be iteratively increase by an increment determined by the surface area for which the model was being generated. Conditions were programmed into the code so as to control the modelling area, iteration increments, mirror angle, and laser dispersion for any given coordinate value at a specified central pitch and lens distance. The program was also required to export the data as it was being generated into external files which could be saved autonomously as the model was completed. In order to fulfill the requirements demanded to generate the theoretical output, two distinct file types were employed.

The first file type is referred to as a python package. These are imbedded files in the programing language that, although not intrinsically part of the python program, have been written and published as downloadable content. They are then installed and operated using a program known as Anaconda, which is a programing shell that runs the Python programing language and can be accessed using a variety of software. The primary software used for the development of the code was a programming window known as Spyder. This programing tool was selected as it runs using the Python language but operates using an output similar to that of MATLAB and was therefore both functional and accessible.

The second file type is a user written subscript. These are individual files that contain a program coded by the user to accomplish a certain task. Five of these were developed for the work presented herein in order to accomplish tasks for which there was no publicly available program. Primarily, this code can be imbedded within iterative loops in order to simplify the layout of the main script, or to generate a specific output that would later be used in the main program.

To produce the theoretical models, three main python scripts and five subscripts were created. The first script was designed to produce a three-dimensional phase map of the interference phase as seen in Equation (2.49) at 25 X-Z coordinates across a theoretical non-uniform SRG. The produced phase maps were generated for theoretical non-uniform SRGs at central pitches of $\Lambda = 500$ nm, $\Lambda = 1000$ nm, $\Lambda = 1500$ nm, and $\Lambda = 2000$ nm and at three lens distance of $f = 35$ mm, $f = 45$ mm,

and $f = 55$ mm. The second script used the information generated by the theoretical phase maps to calculate the grating pitch and grating vector at each of the 25 coordinates in each case listed above. The final script generated an irradiance distribution map at each of the 25 coordinates in each case listed above by applying Equation (2.34).

An in-depth discussion of each Python script, as well as a programing map and the Python code, can be found in Appendix A. The results generated by each of the Python scripts will be presented in Chapter 4.

Chapter 3 Experimental Procedure

The following chapter discusses the procedure and apparatus that were used for the experimental inscription of non-uniform SRGs on azobenzene thin films. The experimental procedure was created with the aim of attaining standardization, reproducibility, and precise characterization of the independent system parameters and the resulting SRGs. This chapter was written to provide an explanation of the approach used to fabricate non-uniform SRGs such that the process and results will be reproducible in future experiments. The requirements that motivated the system design are outlined in Section 3.1 and the resulting process of developing the azobenzene samples, the set up of the inscribing laser, and the measures used to control the central grating pitch and lens distance are given in Sections 3.2-3.4. Finally, the SRG measurement techniques are discussed and the process used to analyse the resulting data is given in Sections 3.5 and 3.6.

3.1 System Requirements

The aim for the design of the experimental non-uniform SRG inscription method was to build an optical system that was efficient, cost effective, and could be accurately modeled using the theoretical analysis outlined in Chapter 2. This design would permit the theory and experimental results to be directly compared in Chapter 4. The theoretical model of the system assumed that a collimated laser beam is incident on a Lloyd's mirror interferometer, where the light that is directly incident on the sample passes through a spherical lens.

The key parameters for determining the properties of the inscription in the theory are the position of the spherical lens with respect to the azobenzene surface, f, and the angle of the Lloyd's mirror with respect to the optical axis, θ. To guarantee reproducibility in the system, precise set up and control of the key parameters was necessary. To reduce additional variability and error in the system, the laser beam properties needed to be precisely controlled, and the samples on to which the grating would be written needed a standardized fabrication method. The selections made to satisfy these parameters and requirements are outlined in Section 3.2 through 3.4 of this chapter.

3.2 Azobenzene Sample Preparation

As discussed in Chapter 1, SRGs can be fabricated using a laser lithography approach to photomechanically imprint an interference pattern on the surface of a photoresistive film. For the production of the non-uniform SRGs discussed herein,

an azobenzene Disperse Red 1 molecular glass (gDR1) was used to produce the thin films necessary for grating fabrication. The gDR1 compound contains an azobenzene chromophore, which permits the repetitive photoisomerization process necessary to generate SRGs when irradiated by an incident laser at an absorbing wavelength. The absorption curve of the gDR1 compound and the film produced is shown in Figure 3.1 and is compared to the absorption profile of the Disperse Red 1 PMMA thin films.

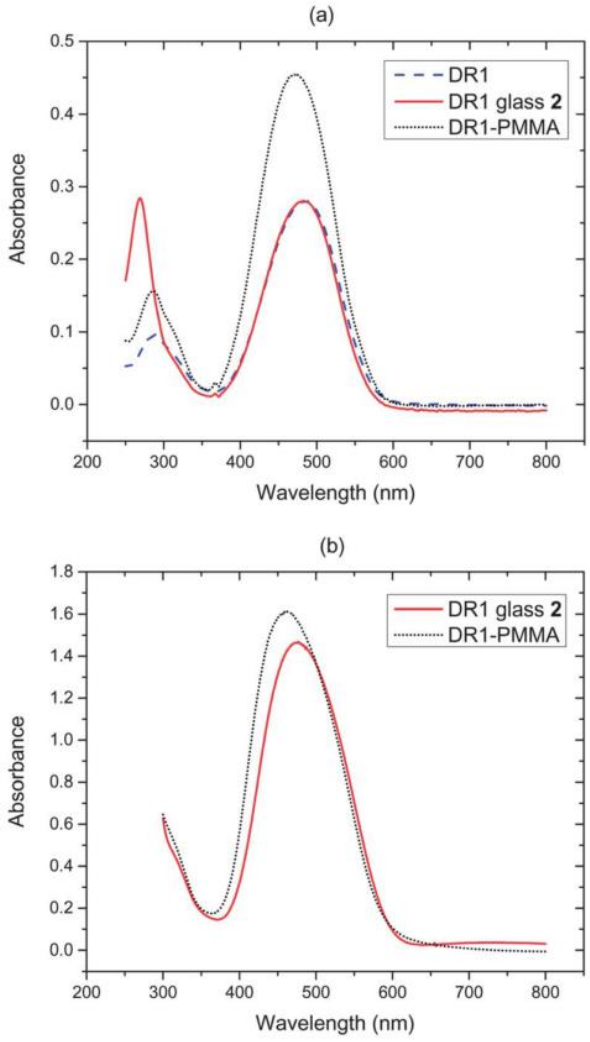

Figure 3.1: a) The absorption curve of Disperse Red 1, Disperse Red 1 Molecular Glass, and Disperse Red 1 PMMA compounds; and b) The absorption curve of Disperse Red 1 Molecular Glass, and Disperse Red 1 PMMA thin films [36].

The gDR1 compound was synthesized at the Royal Military College of Canada by Dr. Oliver Lebel and produced in the form of powder. The molecular structure of the synthesized gDR1 compound is shown in Figure 3.2.

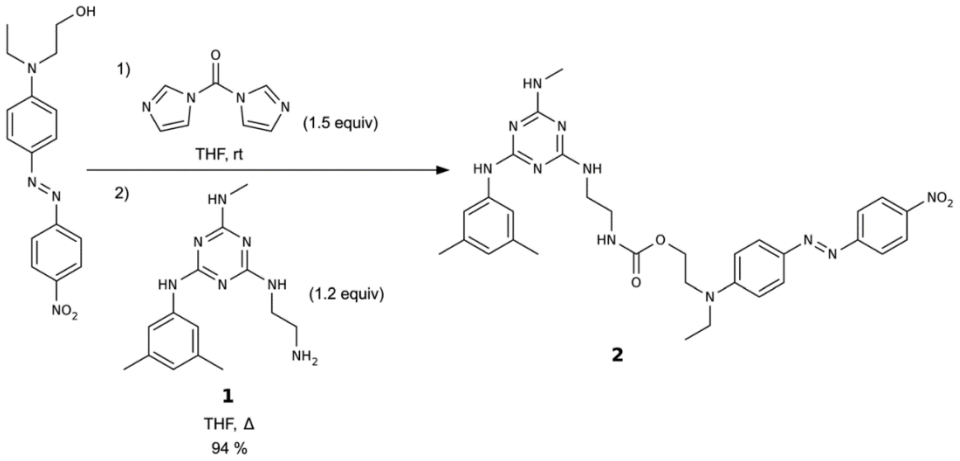

Figure 3.2: The molecular structure for the gDR1 compound [36].

The powder was then dissolved in dichloromethane and diluted to a weight/weight concentration 3%. The solution was shaken for one hour in a Fisher Vortex Genie 2 mechanical shaker to properly combine the chemical mixture. Upon completion of the shaking process, the mixed solution was filtered using a 0.45-microns filter to remove any remaining solids that may compromise the quality of the films.

To produce the substrates onto which the gDR1 solution was deposited, a 70 mm by 35 mm Corning soda-lime glass slide was cut into two equal halves using a diamond tip cutting tool. The two 35 mm by 35 mm slides were thoroughly cleaned to remove any dirt and dust and subsequently dried using a lint free Kimwipe. The washed glass slides were then baked in a ADP-21 vacuum oven set to 95^{o}C for 30 minutes in order to evaporate any remaining moisture on the substrate prior to depositing the gDR1 solution.

The thin film deposition method selected to produce the azobenzene thin films was a spin coating technique. Other thin film production methods exist that would produce thin films of high quality such as Chemical Vapor Deposition, Evaporation Deposition, Sputter Deposition, and Sol-Gel Deposition [61]. Spin coating was chosen as the technique was readily available, produces an evenly distributed film on the glass substrate, and requires fabrication time of less than two minutes per sample. The clean soda-lime glass slide was exposed to a blast of pressurized air to remove any residual dust that had clung to the surface during the

baking process and transportation to the spin coating chamber. Approximately 1 mL of the gDR1 solution was then deposited onto the surface of the substrate using a glass pipet. The sample was spun at approximately 1070 RPM for 25 seconds to evenly distribute the gDR1 solution across the surface and produce a film with thickness of approximately 250 nm. The film thickness was confirmed using a Dektak II profilometer.

The surface of the film was checked for any imperfections that may hinder the grating writing process. Imperfections such as dust trapped under the film surface, large particles in the solution, or an uneven distribution of material can produce surface defects such as deformations or streaking that will hinder the resolution of the inscribed SRG. The sample was then once again baked in the ADP-21 vacuum oven for an additional 30 minutes to evaporate any residual solvent on the surface. Upon completion of the second baking process, the gDR1 film was ready for grating inscription.

The gDR1 thin film generated forms an amorphous glass surface. The amorphous nature indicates that SRGs formed using the gDR1 compound can not only be fabricated on the material's surface, but, can also be erased when the surface reaches its glass transition temperature, T_g. For the gDR1 films, this transition temperature is defined to be 71^{o}C [36]. A heat flow graph of the gDR1 films is shown in Figure 3.3, with the glass transition temperature indicated.

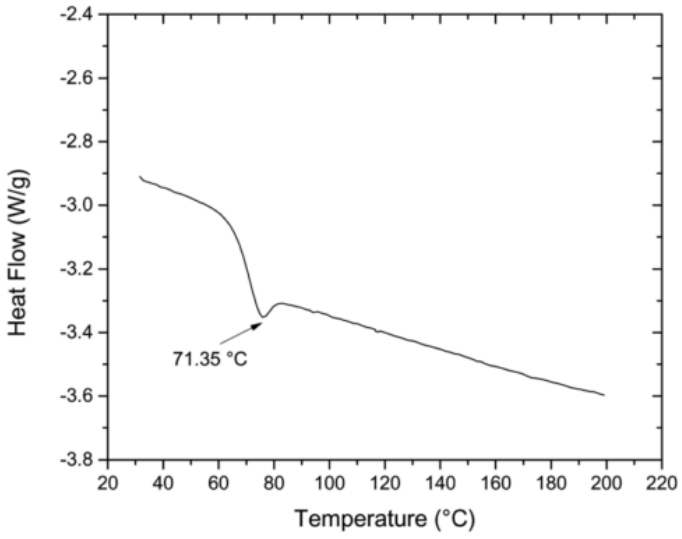

Figure 3.3: Heat flow diagram of gDR1 thin films, with the glass transition temperature of the film indicated [36].

3.3 Inscribing Laser Set Up

This section will describe the laser set up used for the inscription of the non-uniform SRGs. It will explain the laser parameters that were established and held constant throughout the entire SRG writing process and elaborate on the properties of the Lloyd's mirror interferometer and spherical lens used to produce the non-uniform grating pattern.

3.3.1 Inscribing Laser and Optical Set-up

The inscribing laser required a controllable beam size, while still maintaining a high irradiance profile. For non-uniform grating inscription, a collimated, circularly polarized medium power laser beam was necessary to ensure grating quality. The Gaussian profile of the beam was also required to be controlled to limit power loss and laser noise on the edges of the beam in order to write a clean grating across the entire inscription area.

To meet the experiment requirements, the laser used for the grating inscription was a Coherent Verdi V5 diode-pumped continuous wave laser with an irradiating wavelength of $\lambda = 532$ nm. Once emitted from the source, the laser beam passed through a 25 μm spatial filter, which reduced the initial Gaussian profile of the emitted laser beam and removed any aberrations in the laser signal. A collimating lens and subsequent quarter wave plate system was used to produce a collimated circularly polarized beam of laser light. A variable iris was then used to control the diameter of laser beam. The variable iris was set to a diameter of 14 mm for all inscriptions as this provides a large grating surface area and also covers the entire diameter of the selected spherical lens. A single optical rail was used to securely fasten and align each component.

3.3.2 The Lloyd's Mirror Interferometer

The precision and accuracy of the Lloyd's mirror interferometer were important as they controlled the recombination of the beams and, therefore, the interference pattern produced on the sample surface. The Lloyd's mirror interferometer required a rotating mount that could be remotely controlled, an optical mirror large enough to reflect half of the laser beam at small angles of θ, and a mount that would securely fasten the azobenzene sample at a 90° angle to the optical mirror without scratching the film or obstructing the laser.

A rotating platform containing the components of the Lloyd's mirror interferometer was fastened at the end of the optical rail on which the laser was mounted. The rotating platform was established on an optical mount such that the horizontal and vertical position of the interferometer could easily be adjusted in order to calibrate the system. A mirror was firmly attached to the rotating disk and the

azobenzene sample was fastened at a 90^{o} angle with respect to the mirror. The intersection axis between the two surfaces was then positioned at the center of the laser beam so that half of the laser beam was incident on the mirror's surface and half on the azobenzene surface. The centering of the interferometer was verified by ensuring the reflected laser beam from the mirror perfectly overlapped the one incident on the sample.

3.3.3 Spherical Lens and Lens Holder

The spherical lens used to generate the divergent laser beam was a convex lens of 5.72 mm diameter and 14.3 mm focal length. The lens was contained within a lens holder that was fabricated using a 3D printer in the RMC physics department. The design for the lens holder is shown in Figure 3.4.

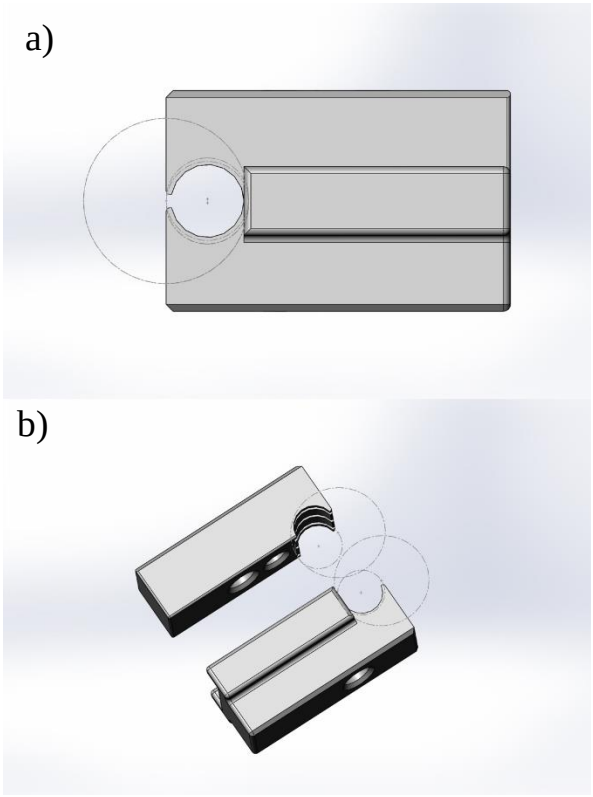

Figure 3.4: A rendered image of the design used to fabricate the spherical lens holder. The image was produced using the AutoCad design software, with the large circle seen around the lens position illustrating the laser beam area.

The lens holder is composed of two interlocking rectangular pieces with a half circle of diameter 5.72 mm cut through one end. The top piece is aligned with the bottom

piece using a slot that is generated by fastening two rectangular walls protruding up from the bottom piece, as can be seen in Figure 3.4 b). In addition to aligning the two pieces, the rectangular walls also blocked excess light from passing through any space between the two halves where they meet. The height of the entire lens holder was set to be 18 mm in order to block any component of the laser beam not passing through the spherical lens. The width of the holder was elongated to allow it to be attached to either an optical post or be held by a clamp. The spherical lens is locked in place using a grove that is cut into the top and bottom of the half circles on each piece. The material used to produce the lens holder was a matted black plastic to reduce any reflection from the laser beam.

At lens distances greater than 30 mm, the laser beam dispersed by the lens will cross the optical axis and be incident on the mirror. The result will produce an anomalous interference pattern in which the diverging light from the spherical lens is interfering with itself in addition to the half of the laser beam reflected by the mirror. To avoid this, a piece of matted black construction paper was used to block the excess light spilling over from the divergent laser beam at all lens distances. The paper was cut to a length that would not block any light reflected from the mirror. The complete optical set up used for experimental grating inscription is illustrated in Figure 3.5.

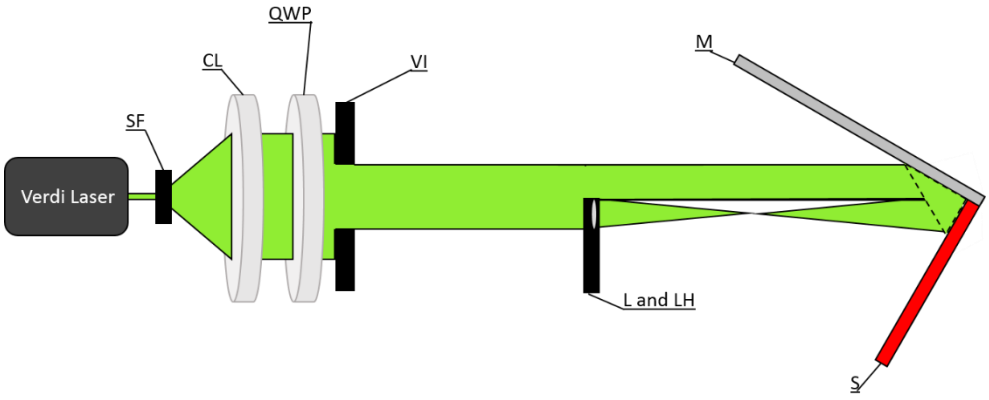

Figure 3.5: An illustration of the complete laser set up including the spherical lens and Lloyd's mirror interferometer. Each component is labeled as follows: SF (Spatial Filter), CL (Collimating Lens), QWP (Quarter Wave Plate), VI (Variable Iris), L and LH (Lens and Lens Holder), M (Mirror), and S (Sample).

3.4 Controlling Parameters

With the optical set up outlined in Section 3.3 being held constant, the two parameters that were varied to control the resulting non-uniform SRG profiles were the lens distance from the azobenzene film and the mirror angle with respect to the

optical axis. This section will discuss the methods used to standardize and control both of these parameters in the grating writing process.

3.4.1 Controlling the Mirror Angle

From Equation (2.41) in Chapter 2, the central pitch of a non-uniform SRG, Λ, is directly correlated to the angle of the mirror with respect to the optical axis. The mirror angle was controlled by rotating the platform on which the interferometer was positioned. The rotating disk was remotely controlled using a Labview program that applied an input value of the desired central pitch, calculated the required mirror angle, and oriented the mirror using a control system established between the computer console and the platform. The mirror angle was calculated by applying a laser of wavelength $\lambda = 532$ nm and the desired central pitch value to:

$$\theta = \sin^{-1}\left(\frac{\lambda}{2\Lambda}\right) \tag{3.52}$$

Where θ is the mirror angle, λ is the wavelength of the laser, and Λ is the grating central pitch. Using the derived mirror angle, the program could accurately position the Lloyd's mirror interferometer assuming that the system was properly calibrated.

The calibration of the system occurred prior to setting the interferometer for every grating sample. This was done by setting the Labview program's central pitch input to a value of $\Lambda = 499$ nm. This grating central pitch had a known mirror orientation on the Lloyd's mirror interferometer rotating platform. The platform was set to the known position, and securely fastened. Once the system was calibrated the mirror position was adjusted remotely by changing the central grating pitch input in the Labview program. The four central pitches selected for grating inscription and their corresponding mirror angles are shown in Table 3.1.

Table 3.1: The four central gating pitches used in the fabrication of non-uniform SRGs and their corresponding mirror orientations with respect to the optical axis.

Grating Central Pitch (Λ)	**Mirror Angle wrt Optical Axis (θ)**
500 nm	32.1°
1000 nm	15.4°
1500 nm	10.2°
2000 nm	7.6°

3.4.2 Spherical Lens Position

The laser beam divergence at the surface of the azobenzene film is governed by the distance of the spherical lens from the film's surface. Three lens distances were selected to model the theoretical simulation performed in Chapter 2. The lens distance was varied by 10 mm increments to generate non-uniform SRGs at lens positions $f = 35$ mm, $f = 45$ mm, and $f = 55$ mm from the azobenzene film.

The lens system was controlled independently from the rest of the optical system described in Section 3.3. The lens and lens holder were held in place by a clamp which was then secured to an independent optical mount and rail. This configuration allowed for control of the lens position with respect to the azobenzene film and the center of the laser beam without affecting any other parameters of the laser set up or the Lloyd's mirror interferometer. Once the lens was positioned in the center of the laser beam half directly irradiating the azobenzene film, and properly oriented with respect to the rest of the set up, the distance could be controlled by simply moving the mount along the optical rail. The lens distance from the sample surface was measured using a calliper. The distance was taken from the center of the lens to the intersection axis between the mirror and the azobenzene film. An illustration of the laser beam overlap on the azobenzene film at the three lens positions specified is shown in Figure 3.6. The grating area of the non-uniform SRGs inscribed at these lens positions would only be written within the areas the laser beams overlap.

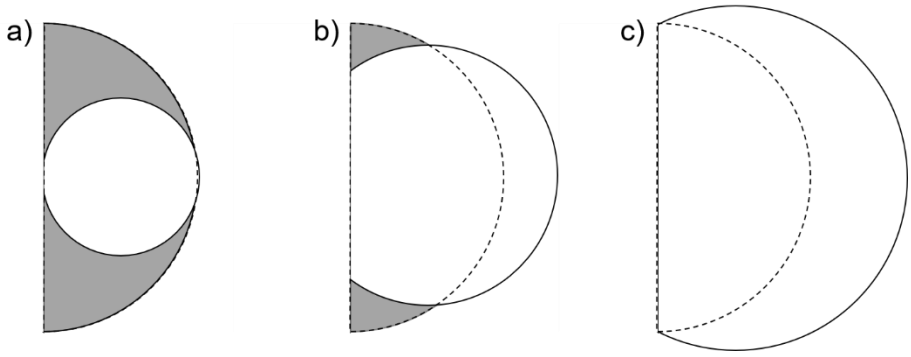

Figure 3.6: An illustration of the beam overlap generated on the surface of the azobenzene film with the introduction of a spherical lens to a Lloyd's mirror interferometer. The three images show the result of placing a spherical lens of focal length $f_1 = 14.3$ mm at the following distances from the surface being irradiated: a) $f = 35$ mm, b) $f = 45$ mm, and c) $f = 55$ mm.

3.5 Scanning and Data Acquisition

3.5.1 Scanning Parameters

A Bruker Dimension Edge Atomic Force Microscope (AFM) was used to analyze the surface profile of each non-uniform SRG. An AFM was selected for SRG analysis as it can three-dimensionally map surface nanostructures to a precision of up to 50 pm [62]. The parameters of the AFM were also conducive to the periodic structure analysis of SRGs, and the output format was easily accessible and manipulatable in future data processing stages. An inverted image of the AFM tip used for the scanning process is shown in Figure 3.7.

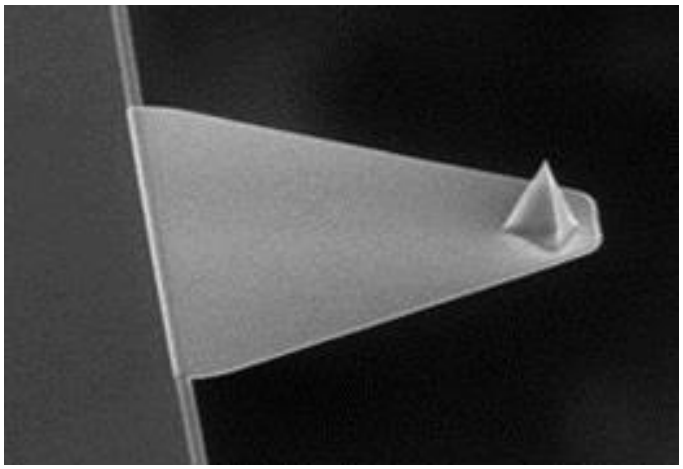

Figure 3.7: Image of the AFM tip used to scan the surfaces of the non-uniform SRGs [63].

The tip has an approximate radius of 5-12 nm and a height of the cantilever of 2.5-8 μm [63].

The AFM measures a surface profile using the feedback produced from the scanning probe repeatedly tapping the surface of the grating [64]. The feedback is generated from the force between the scanning surface and the tip of the probe. The system measures the position of the AFM tip as it is moved across the surface during a scan and the normal force on the probe every time the probe taps the surface of the grating. The vertical position of the tip is measured optically to retrieve data on the height of the surface. As the surface structure changes under the AFM tip during a scan, the tip position is adjusted to maintain a constant peak force during the tapping procedure, and therefore follows the profile of the structure. This feedback system generates three-dimensional position data for the entire surface being scanned.

The resolution of the image produced by the AFM was continuously monitored and optimized using an AFM application known as ScanAsyst [64]. This

application varies the AFM scanning system parameters in real time during the scan in order to adjust image scales, establish an image origin, and realign acquired data for optimized image output. The scan speed can also be adjusted prior to commencing a scan and can have a slight influence on the image resolution. Higher scanning speeds will decrease data resolution for complex surface patterns as the probe is hastily moved across the grating surface and the system has less time to adjust scanning parameters.

3.5.2 Scanning Procedure

For each scan the AFM tip was automatically lowered using a surface detection program in the AFM control software. The AFM software halts the movement of the tip once a tapping force that exceeds the system noise is registered, indicating contact with the surface.

Prior to commencing a scan, the surface was oriented with respect to the scanning probe and direction so that the coordinate system mirrored the theoretical SRG inscription model. The origin for each SRG was centered along the vertical axis and positioned on the left most edge of the grating area along the horizontal axis. Similarly to the theoretical model described in Chapter 2, 25 evenly spaced X-Z coordinates were selected for data acquisition. The coordinates were taken as measured distances from the established scanning origin. In order to standardize the coordinate positions across the samples, the AFM Nanodrive software was used to position the scanning probe and monitor the grating surface during scans. The software comes with a built-in positioning tool with which the probe can be moved to a specified position on the SRG surface with respect to a set origin and within a precision of 0.5 nm. The SRG was then oriented so that the grating vector at the center most point was parallel with the scan direction. This calibration allowed for the highest scanning resolution possible at a standardized scanning speed of 1 Hz. For all samples, a data sampling rate of 256 points per line was set. The sampling rate governed both the number of data points taken per line and the number of lines per scan. A data matrix of dimensions equal to the data sampling rate was therefore produced for each sample.

Scan dimensions of 5 μm squares were set for the $\Lambda = 500$ nm and $\Lambda = 1000$ nm central pitch gratings and 10 μm squares for the $\Lambda = 1500$ nm and $\Lambda = 2000$ nm central pitch gratings. These dimensions were selected as they capture enough of the grating profile at each central pitch to accurately model the grating properties. The scanning process moves the AFM tip both forward and backward horizontally across the surface to complete one line. In this motion, the AFM collects the number of data points specified by the sampling rate in both its forward and

backward motion. An illustration of a completed AFM scan for a SRG of central pitch $\Lambda = 1000$ nm is shown in Figure 3.8.

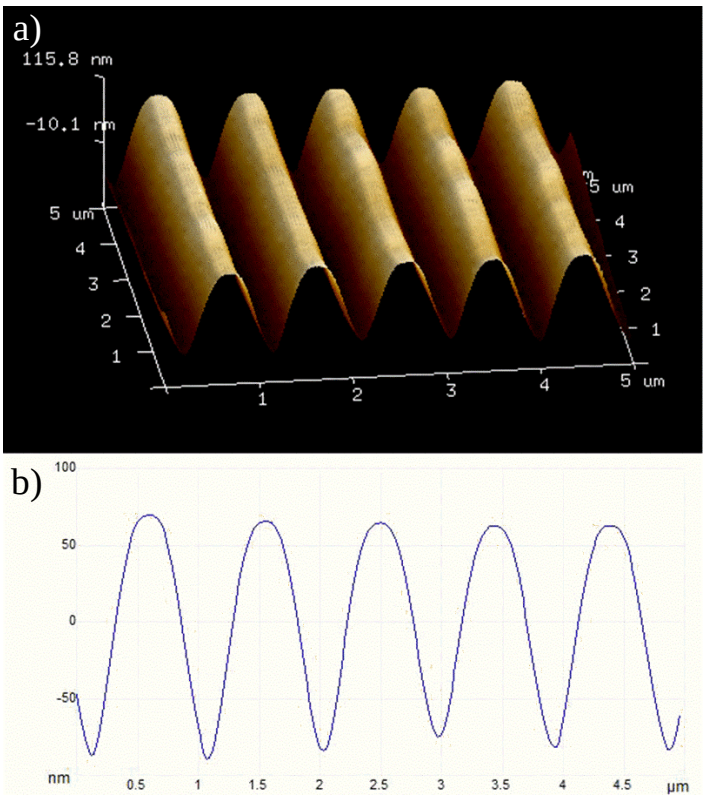

Figure 3.8: An illustration of the output from a Bruker Dimension Edge AFM scan in the form of a) a three-dimensional rendering of the grating surface profile, and b) the grating cross section.

3.6 Origin Data Analysis

OriginLab® Data Analysis and Graphing Software is a computer program that can be used to analyse, model, and integrate large data files for presentation in a variety of formats. For the analysis of the non-uniform SRGs, this software was used to produce one-dimensional grating cross sections, two-dimensional irradiance distribution colour maps, and three-dimensional grating profile representations of the exported AFM data.

The data file generated from the AFM scan contained a data matrix of grating height values across the scan area. Each row in the data matrix was the result of one pass of the AFM scanning probe. This facilitated the grating analysis as each matrix row could be taken as an individual cross section of the grating.

The application used to map the position of each peak was the Peak Analyzer program provided in the OriginLab® software package. This program uses a one-dimensional data set to locate any local maxima in the set. For the case of sinusoidally repeating data, such as the cross section of a SRG, the program is also capable of establishing a baseline using the grating minima and integrating the area under each grating peak. The program locates the grating peaks by finding local maxima in the data points and comparing them to every point within one period of the grating. The coordinate of the local maxima in the data set was then presented next to the peak number it represented. Alternative methods are provided in the program, such as the application of a first and second derivative method which can be used to find local extrema as well as hidden peaks. These methods were also tried, however there was no improvement noticed in the quality of the more complex methods, and therefore the simpler iterative process was used.

Two grating cross sections were selected for analysis from every scan. The positions of both cross sections were verified to have no abnormalities due to either surface or scanning defects. The peak coordinates were determined for each grating cross section and were used to calculate the grating pitch by determining the separation distance between two subsequent peaks along a single cross section. The distance values determined for both grating cross sections were averaged to yield the grating pitch value at the coordinate of the scan being analyzed. To calculate the grating vector, the angle of a straight line connecting corresponding peaks from the two analyzed grating cross section was calculated for each peak. The angle values were then averaged, and the value of the grating vector was derived from the result. The values of the maxima and minima for the two grating cross sections can also be used to calculate the modulation depth of the SRG at each scan position.

Chapter 4 Results

The following chapter presents and discusses the theoretical model and experimental results obtained for the non-uniform SRG pattern inscription created using a Direct Interference Lithography Patterning technique. The SRG patterns produced are characterized by the grating pitch, grating vector, and grating modulation depth distribution across the surface. The SRG properties were determined by selecting 25 points across the grating profile at which the local grating pitch, vector orientation, and modulation depth could be calculated. As the point selections were matched between experiment and the theory, a direct comparison could be made between the two. A comparison between the theory and experiment is made from the resulting grating and modulation depth profiles of SRGs fabricated at three different lens positions, *f*, to validate the model and fabrication technique used. A comparison is also made between the experimental and theoretical grating pitch rate of change and grating vector rate of change by manipulating the parameters of the grating central pitch and lens position.

4.1 Theoretical Results

4.1.1 Creating the Theoretical Model

Theoretical representations of non-uniform SRGs were calculated using the interference phase information generated by Equation (2.49) in Chapter 2. A point by point analysis of this information, centered around specified X-Z coordinates, produced a two-dimensional phase map of the interference pattern generated by the recombined laser beams. The gDR1 thin films, used in the experimental fabrication of the non-uniform SRGs, are photoresistive and undergo a *cis-trans* photoisomerization process, in which the grating pattern fabricated on the film is the second derivative of the interference phase of the incident light. Therefore, the calculation of the interference phase at the theoretical sample surface is a valid representation of the non-uniform grating profile.

An example of the phase generated by the theoretical model described in Chapter 2 is shown in Figure 4.1.

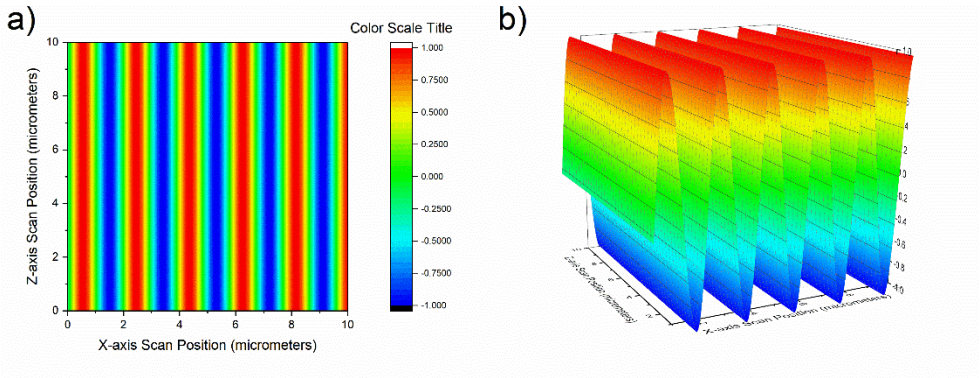

Figure 4.1: Theoretical SRG generated using the phase information of the recombined laser beams in the Lloyd's mirror interferometer. The interference phase is illustrated both as a) a two-dimensional colour map and b) a three-dimensional representation of the phase.

The above figure illustrates both a two-dimensional colour map representation and three-dimensional profile of the interference phase of the recombined laser beams. The depth magnitude of the three-dimensional theoretical gratings has no correlation to the actual modulation depth of the SRGs as it is simply a unit representation of the sinusoidal shape of the interference pattern. The grating modulation depth will be modelled later on in this chapter using the expression for the recombined irradiance of the two laser beams from Chapter 2, and will be discussed in the next section. The height and width of the analysis area are set to mirror the dimensions of a scan performed by the AFM in the experimental analysis of the non-uniform SRGs.

To characterize each theoretical sample, the phase profiles of the interference pattern were produced at 25 X-Z coordinates across the surface at measured increments. For the 45 mm and 55 mm lens positions, the coordinates of analysis were selected to be at increments of 1.25 mm to cover a square area of dimensions 5 mm in height and width. The 35 mm analysis area required a smaller analysis size due to the reduced inscription area of the laser beam. The positions were therefore selected at increments of 1 mm to form an analysis area of 4 mm in height and width.

By producing theoretical phase maps using dimensions simulating those produced in an AFM scan, the non-uniformity of the SRG pattern can be directly observed. The varying grating pitch and vector profiles can be qualitatively compared in the light phase plots produced at the incremental positions of analysis in order to generate a broader illustration of the overall grating profile. An example of a qualitative non-uniform grating profile is illustrated in Figure 4.2.

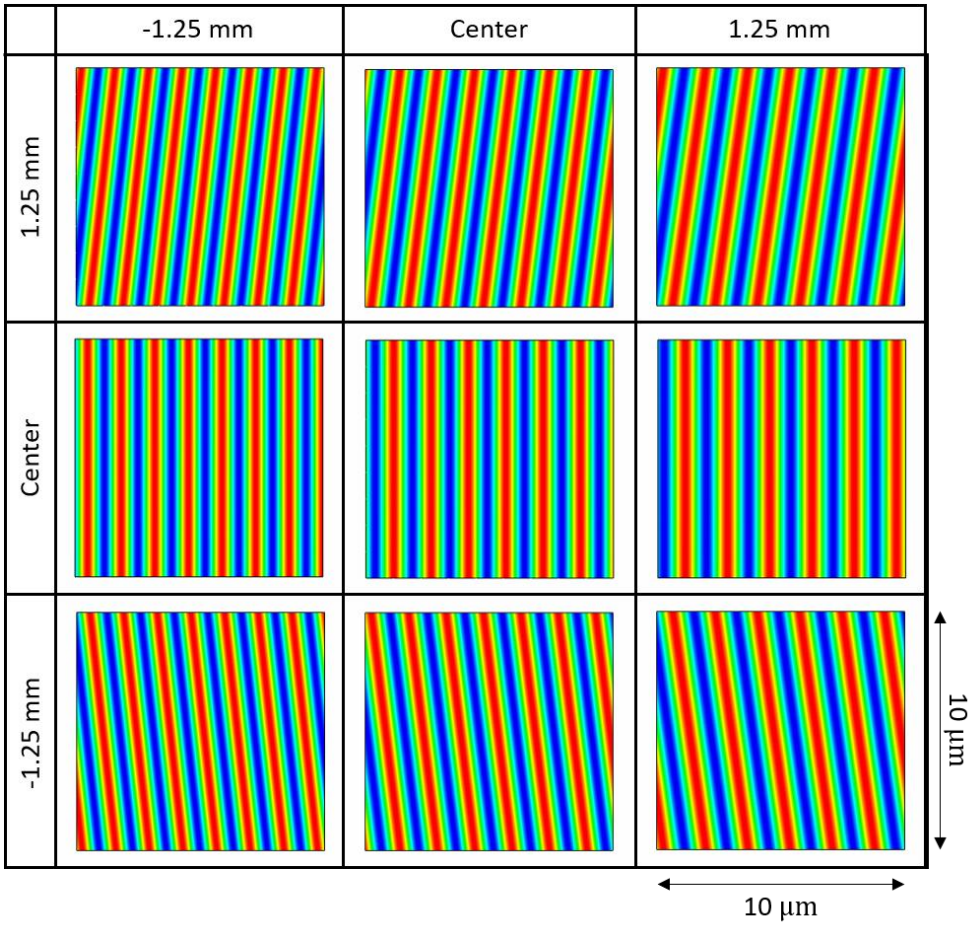

Figure 4.2: A qualitative illustration of the grating pitch and vector orientation across the surface of a theoretical SRG with central pitch $\Lambda = 1500$ nm and lens distance $f = 45$ mm.

The data presented in Figure 4.2 is a theoretical model of a SRG with central pitch $\Lambda = 1500$ nm and lens distance of $f = 45$ mm. The nine phase plots that make the figure have dimensions of 10 µm height and width, and are spaced at 1.25 mm increments. The center phase plot is the center point of the SRG.

4.1.2 Analyzing the Theoretical Model

As illustrated in Figure 4.2, the grating pitch and vector changes gradually across the surface of the SRG. Due to the size of the grating profile, a square of 5 µm or 10 µm dimensions is necessary to clearly analyze the grating profile. At this scale, the gratings can be approximated as uniform gratings with varying grating vector properties. As such, a local pitch and grating vector can be calculated from

each grating profile plot. The local grating pitch and vector information was therefore calculated for each phase profile produced using the theoretical model. The process of extracting the grating pitch and vector information is outlined in Chapter 2 and Annex A in the description of the Python code written to accomplish the analysis. The result is a local grating vector orientation and grating pitch value for each X-Z coordinate, with the properties illustrated in Figure 4.3.

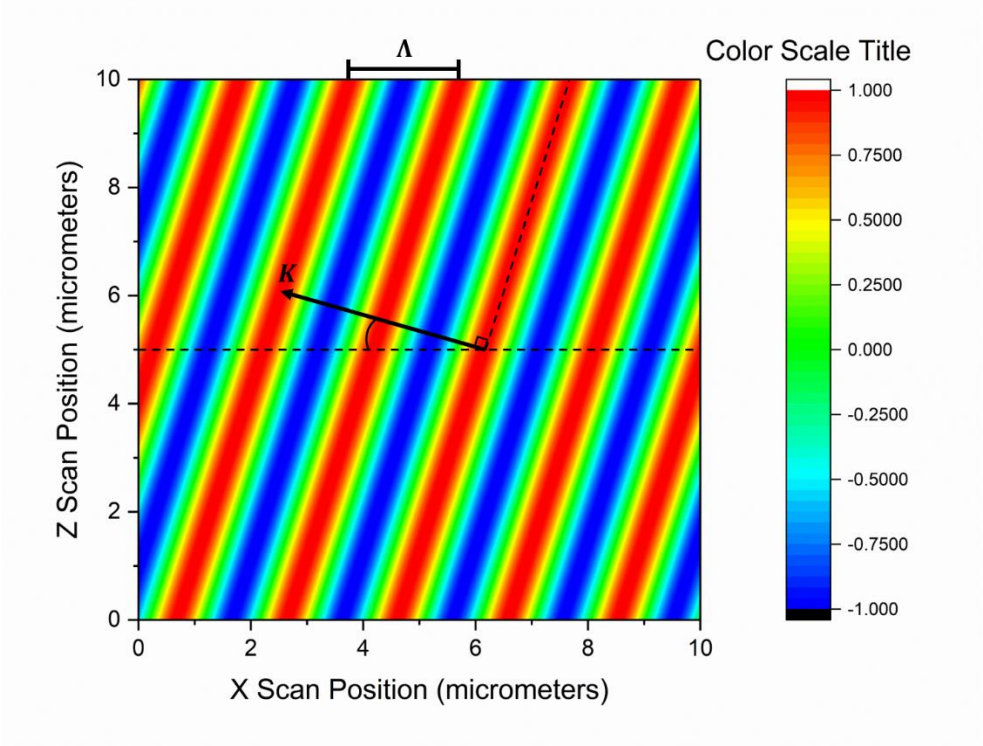

Figure 4.3: Reference for the measurement of the local grating pitch and vector orientation on the surface of a theoretical SRG.

In Figure 4.3, the orientation of the grating vector, K, is determined from the angle between the horizontal axis and the grating vector itself. The grating pitch and vector values are determined for the remaining 24 points across the surface of the theoretical SRG. The grating pitch and vector orientation can then be used to create a vector plot of the grating profile across the surface of the theoretical SRG.

4.1.3 Generating the Irradiance Model

In addition to determining the pitch and grating vector information, the laser irradiance was also calculated at each of the 25 coordinates analyzed. Using the Python code outlined in Annex A, an average irradiance value was determined by

applying Equation (2.27) from Chapter 2. The values generated were used to produce a colour plot representing the distribution of the laser irradiance across the surface of the theoretical SRG. This model was generated to determine if the theoretical irradiance value correlated with the SRG modulation depth distribution measured in the experimentally inscribed SRGs.

An initial irradiance of 428 mW/m^2 was applied to simulate the irradiance value of the Verdi V5 diode pumped continuous wave laser used to experimentally inscribe the non-uniform SRGs. The I_2 term from Equation (2.29), representing the laser irradiance of the beam incident on the Lloyd's mirror, was therefore calculated to reflect the area covered by the beam as it was reflected by the Lloyd's mirror onto the azobenzene surface. The I_1 term, representing the irradiance of the laser beam directly incident on the azobenzene surface, was calculated using the power incident on the surface area of the spherical lens. The transmitted irradiance was then calculated based on the area of the beam incident on the azobenzene sample at a given point. The area of the beam at any point was determined to be dependent on the distance of the lens from the sample surface as well as the angle of the mirror, since the laser beam was diverging. The I_{12} term, or the interference irradiance, was then calculated at the specified coordinate using the two individual irradiance terms, as well of the recombined interference phase.

4.1.4 SRG Irradiance and Vector Models

The grating vector and pitch information generated at each X-Z coordinate were combined to produce a grating vector map across the SRG surface. The vector map was overlaid on the theoretical irradiance distribution, and the result can be seen in Figure 4.4.

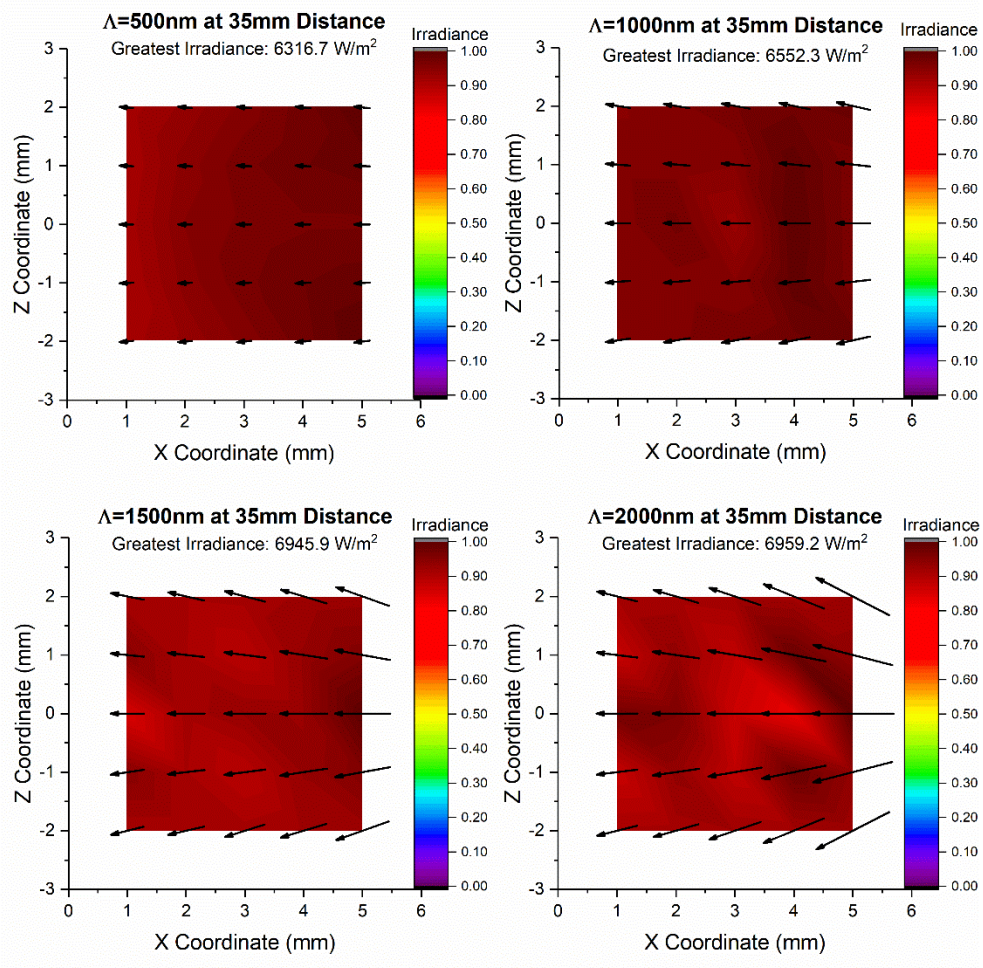

Figure 4.4: The grating pitch, vector orientation, and irradiance distribution for theoretical non-uniform SRG fabricated at central pitch values of $\Lambda = 500$ nm, $\Lambda = 1000$ nm, $\Lambda = 1500$ nm, and $\Lambda = 2000$ nm and a lens position of $f = 35$ mm.

The four plots illustrated in Figure 4.4 are for central pitch values of $\Lambda = 500$ nm, $\Lambda = 1000$ nm, $\Lambda = 1500$ nm, and $\Lambda = 2000$ nm at a lens position of $f = 35$ mm. These parameters were selected as they present the greatest variance in pitch and grating vector orientation, however a similar comparison can be done between the four central pitches at lens distances of $f = 45$ mm and $f = 55$ mm. In Figure 4.4, the grating local pitch is represented by the magnitude of the arrow at that position, and the orientation of the arrow represents the grating vector. The arrow magnitude has been standardized across all four plots, with a scale provided at the base of the figure to depict the length of an arrow with a grating pitch of $\Lambda = 1000$ nm.

In Figure 4.4, it can be seen that the grating central pitch has a dramatic influence over the theoretical grating profile, with SRGs written at higher central pitch values exhibiting a greater change in magnitude in both pitch and grating vector. This is supported by the analytic expression for the interference phase in Equation (2.49) from Chapter 2. At higher central pitch values, the mirror angle with respect to the optical axis, θ, will be lower. Consequentially, from Equation (2.49), all of the X coordinate terms are influenced by the mirror angle, impacting the contribution of the X coordinate to the overall interference phase value at any given point. However, the grating pitch does not vary along the Z-axis since the Z coordinate value in the $h(z)$ term in Equation (2.45) is unaffected by the mirror angle. In addition, the higher central pitch values will have a greater rate of change in the local grating pitch because the interference term, governed by Δ in Equation (2.44), will increase more rapidly at smaller values of θ.

4.2 Experimental Results

This section will discuss the results of the non-uniform SRG fabrication technique discussed in Chapter 3. The physical SRGs are presented along with their property analysis, with the aim of characterizing the data produced from the AFM surface profiling.

4.2.1 Experimental Production on Non-Uniform SRGs

The experimental procedure described in Chapter 3 produced non-uniform SRGs at three lens positions of $f = 35$ mm, $f = 45$ mm, and $f = 55$ mm and central pitch values of $\Lambda = 500$ nm, $\Lambda = 1000$ nm, $\Lambda = 1500$ nm, and $\Lambda = 2000$ nm. The fabrication process generated six SRGs on a single gDR1 sample, with two gratings written at each lens position, and each grating having the same central pitch. This created a backup system in case one grating was damaged during production or later during the analysis stage. An example of a set of three non-uniform SRGs fabricated at the three specified lens positions is shown in Figure 4.5.

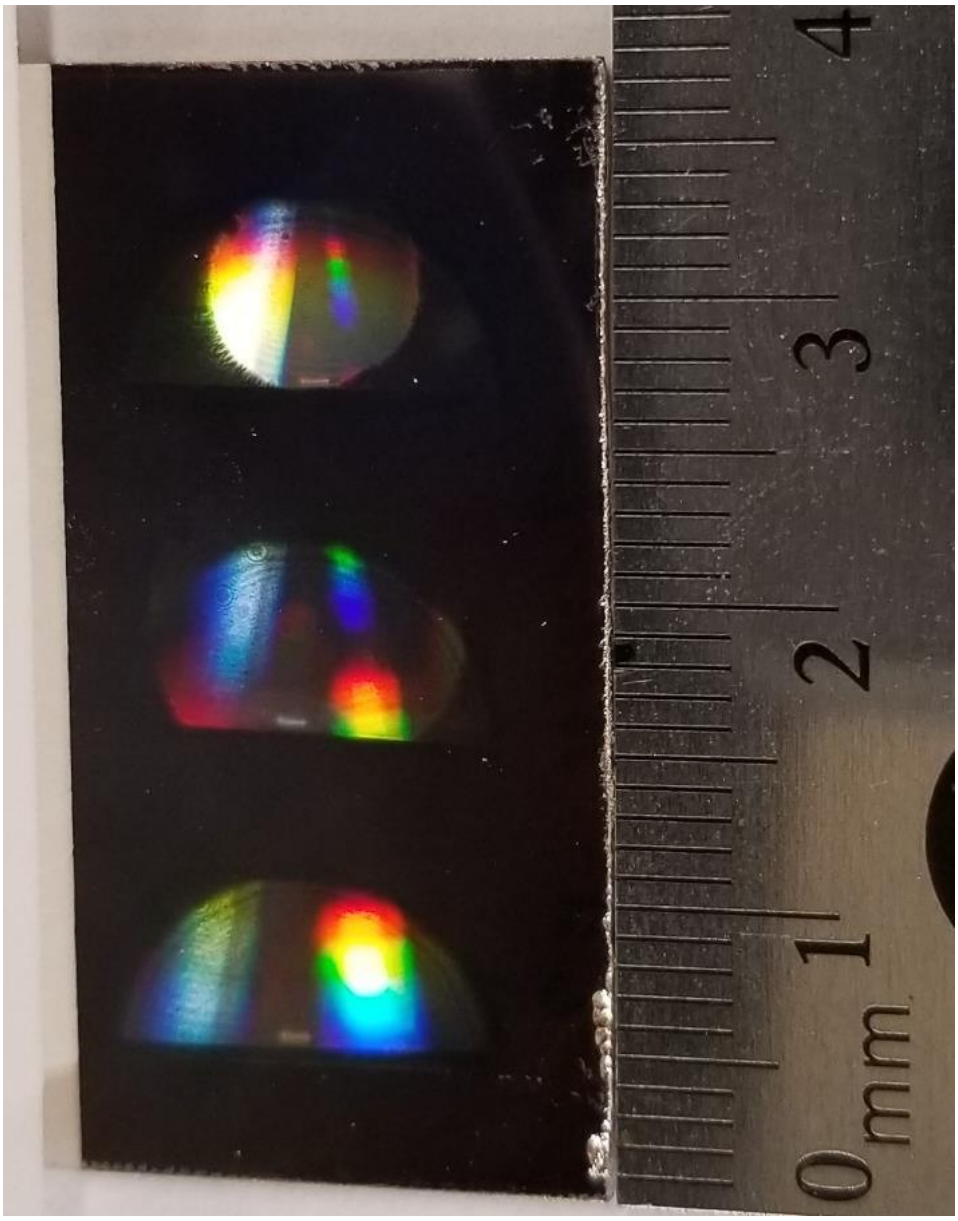

Figure 4.5: Experimentally inscribed non-uniform SRGs at a grating central pitch of $\Lambda = 1000$ nm and lens positions of $f = 35$ mm, $f = 45$ mm, and $f = 55$ mm from top to bottom.

All three of the SRGs depicted in Figure 4.5 are written at a central pitch of $\Lambda = 1000$ nm. The varying inscription area for the three lens positions caused by the divergence of the laser beam from the spherical lens is clearly shown in Figure 4.5.

The inscription areas for lens positions greater than $f = 55$ mm will not change since the grating size is regulated by the irradiating area of the beam reflected from the Lloyd's mirror.

4.2.2 Grating Profile and Depth Analysis

The grating local pitch and vector information was obtained from the AFM data matrices at each coordinate point analyzed, as described in Chapter 3. The results obtained from the Origin software analysis of this data was used to generate a plot of the grating properties across the area of analysis for each grating.

In addition to the grating pitch and vector information, the grating modulation depth was extracted from the AFM data. The result represents an averaged local value for the grating modulation depth at a random X-Z coordinate and was generated using a grating cross section taken from averaging the profile of the entire local grating surface. An example of the measurement taken is shown in Figure 4.6.

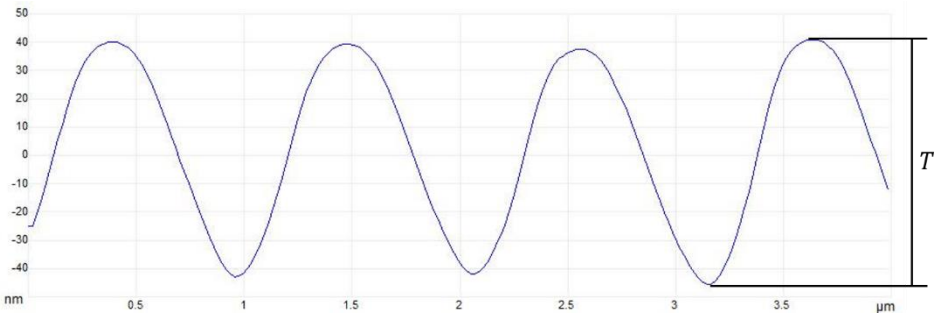

Figure 4.6: Averaged grating cross section used to derive the grating modulation depth at a random coordinate on the surface of a non-uniform SRG with central grating pitch of $\Lambda = 1000$ nm.

The modulation depth of the SRG, shown as T in Figure 4.6, was used to construct a grating depth profile across the SRG surface.

4.2.3 Experimental Vector Models

The local grating pitch and vector information at the 25 X-Z coordinates analyzed were used to generate a vector plot of the experimentally fabricated SRGs. The modulation depth information at the 25 coordinates was used to generate a colour map illustrating the grating modulation depth change across the SRG surface. The results for the four central pitch values at a lens position of $f = 35$ mm is presented in Figure 4.7.

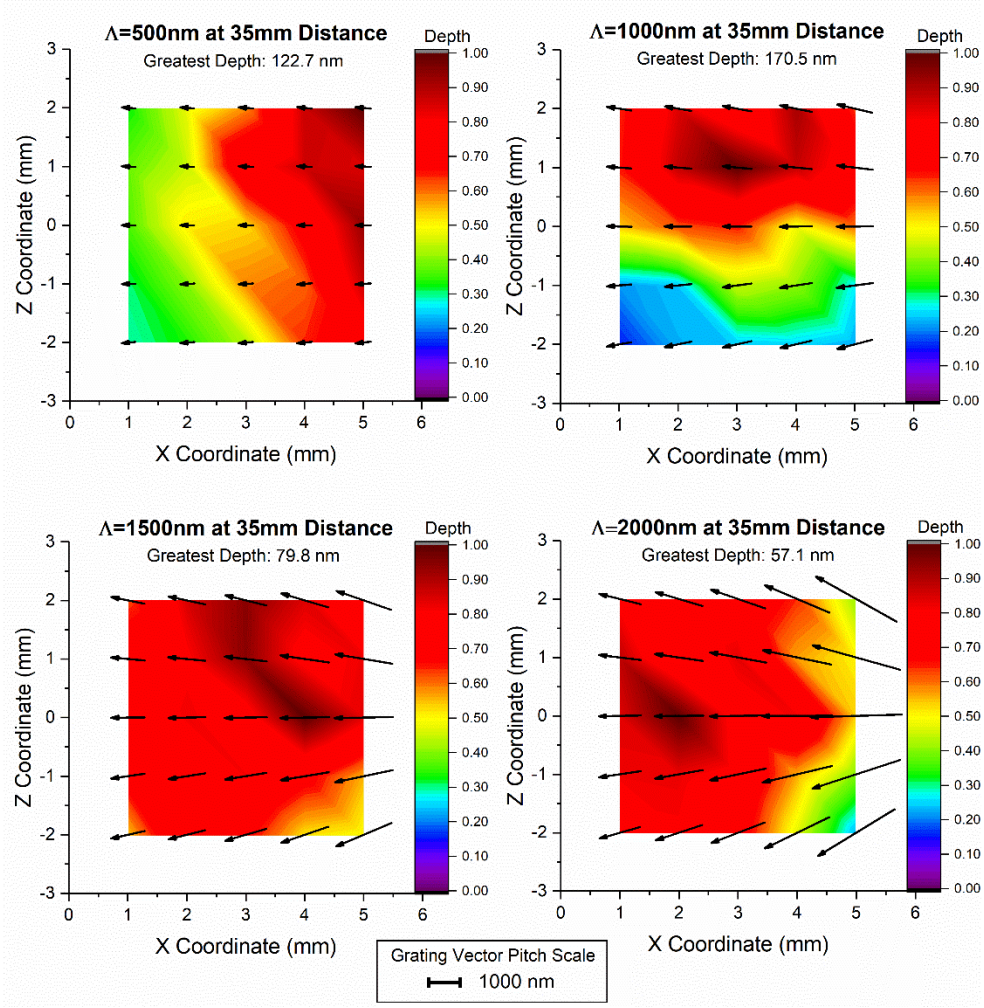

Figure 4.7: The grating pitch, vector orientation, and irradiance distribution for experimentally inscribed non-uniform SRG at central pitch values of $\Lambda = 500$ nm, $\Lambda = 1000$ nm, $\Lambda = 1500$ nm, and $\Lambda = 2000$ nm and a lens position of $f = 35$ mm.

The direction of the arrows in the vector plots presented in Figure 4.7 a)-d) illustrate the grating vector orientation at the X-Z coordinate from which the data was taken. The magnitude of the arrows show the grating pitch, with the scale being standardized across all four vector plots. A standardized arrow magnitude representing a local pitch value of 1000 nm is presented in the legend at the bottom of Figure 4.7.

The influence of the grating central pitch on both the orientation of the grating vector, as well as the grating pitch change across the SRG surface is clear

from the results presented in Figure 4.7. It can also be seen that the grating pitch is chirped along the X-axis, however it appears to remain constant along the Z-axis.

When compared to the theoretical results illustrated in Figure 4.4, a close correlation between the local grating pitch values and grating vector orientations across the area of analysis is observed at identical central pitch and lens position values. There are however noticeable discrepancies between the irradiance distribution and the SRG modulation depth distribution. The comparison and explanation of the similarities and differences between the two models will be discussed further in Section 4.4.

4.3 Varying the Lens Position

In both Figure 4.4 and Figure 4.7, the vector maps illustrate the effect of varying the central pitch of the SRG being modeled, and the result of the change on the grating profile across the entire surface. A comparison will now be made between SRGs written at identical central pitches but varying lens positions. An example of the grating profile variation generated by setting the central pitch value to $\Lambda = 2000$ nm and adjusting the lens position to distances of $f = 35$ mm, $f = 45$ mm, and $f = 55$ mm is shown in Figure 4.8.

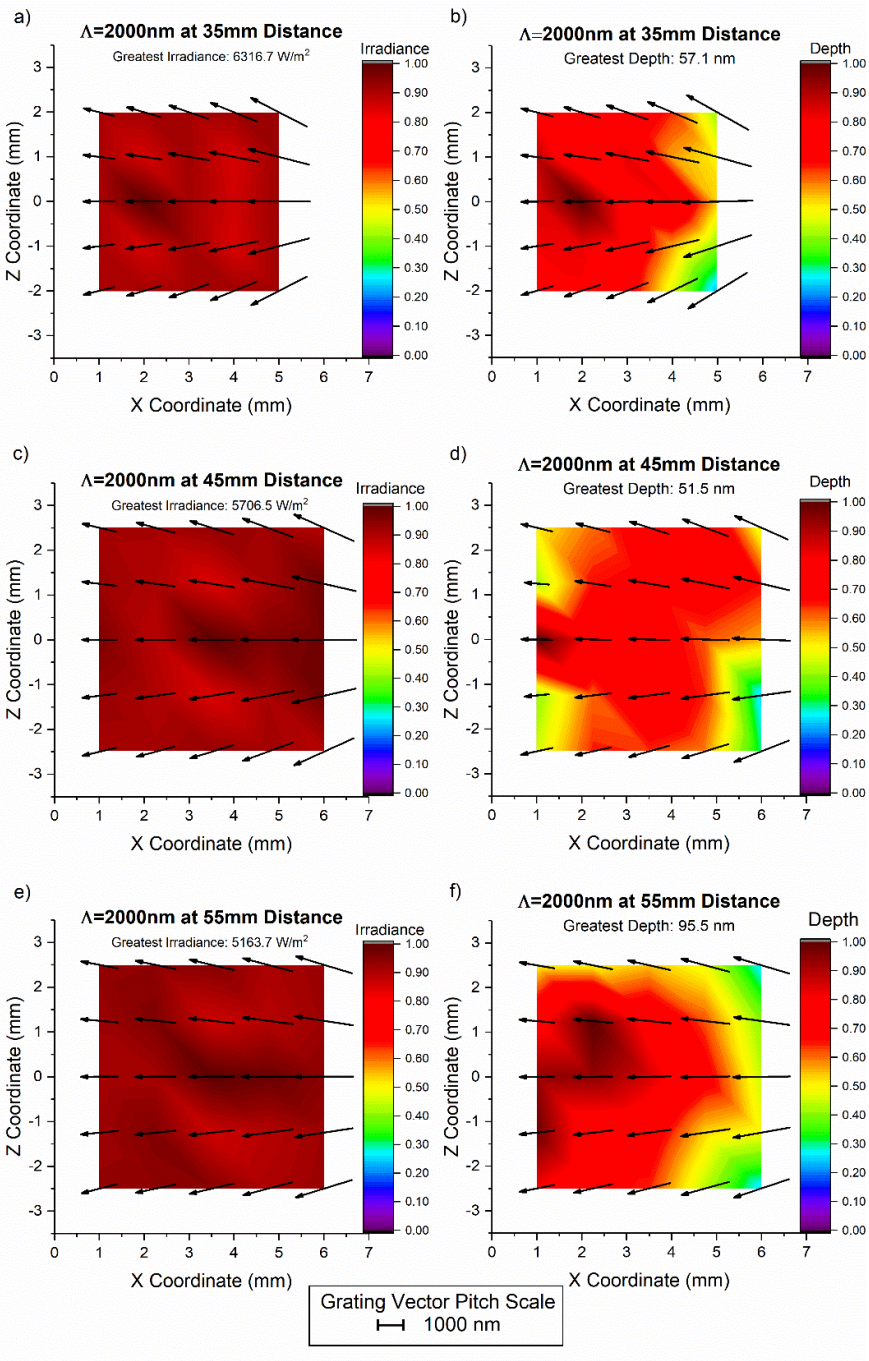

Figure 4.8: Theoretical (left) and experimental (right) non-uniform SRG written at a central pitch value of $\Lambda = 2000$ nm and lens positions of $f = 35$ mm, $f = 45$ mm, and $f = 55$ mm.

Figure 4.8 shows both the SRG profile change with respect to the grating pitch and vector as well as the depth profile for theoretically and experimentally produced non-uniform SRGs. The central pitch value of $\Lambda = 2000$ nm was selected for this analysis as it most clearly illustrates the effect of the lens position on the SRG structure.

As seen in Figure 4.8, as the lens is moved further from the azobenzene surface, the grating parameters exhibit a less drastic change across the surface. For the experimentally inscribed SRG written at a lens position of $f = 55$ mm, the local grating pitch and vector at coordinates on the edges of the analysis area clearly exhibit a less drastic variation from the center vector than those taken at the same coordinates on the SRGs written at $f = 45$ mm and $f = 35$ mm. This trend in the variation of the grating parameters across the grating surface is supported by the theoretical model, as the grating parameters exhibited in the theoretically produced SRGs closely match the grating profile produced experimentally.

An investigation into the numerical differences between the rate of change in the grating pitch (chirping rate) and the rate of change in the grating vector orientation will be discussed in Section 4.4. An explanation for the trend observed in Figure 4.8 however can be provided by discussing the geometrical analysis of the laser beam inscribing the SRG at the three lens positions. The divergence of the laser beam from the spherical lens will produce larger areas of irradiance the further away the spherical lens is placed from the surface of the azobenzene film, as illustrated in Figure 3.6. Selecting a position of analysis anywhere on the surface of the SRG and tracing a straight line from that coordinate to the focal point will yield an angle between the line and the lens axis. By moving the lens further away and thereby changing the distance of the lens to the sample surface, the angle between the line connecting the lens focal point to the specified coordinate and the lens axis will decrease. Effectively, by positioning the lens further away from the azobenzene surface, the SRG grating profile is being magnified. Therefore, the chirping rate and the vector orientation rate of change will gradually decrease as the lens position increases.

The effect that varying the lens position has on the grating profile is also affected by the grating central pitch, as can be expected from the results in Figure 4.4 and Figure 4.7. A comparison between non-uniform SRGs inscribed experimentally at central grating pitch values of $\Lambda = 1000$ nm and $\Lambda = 2000$ nm at the three lens positions analyzed in Figure 4.8 is shown below in Figure 4.9.

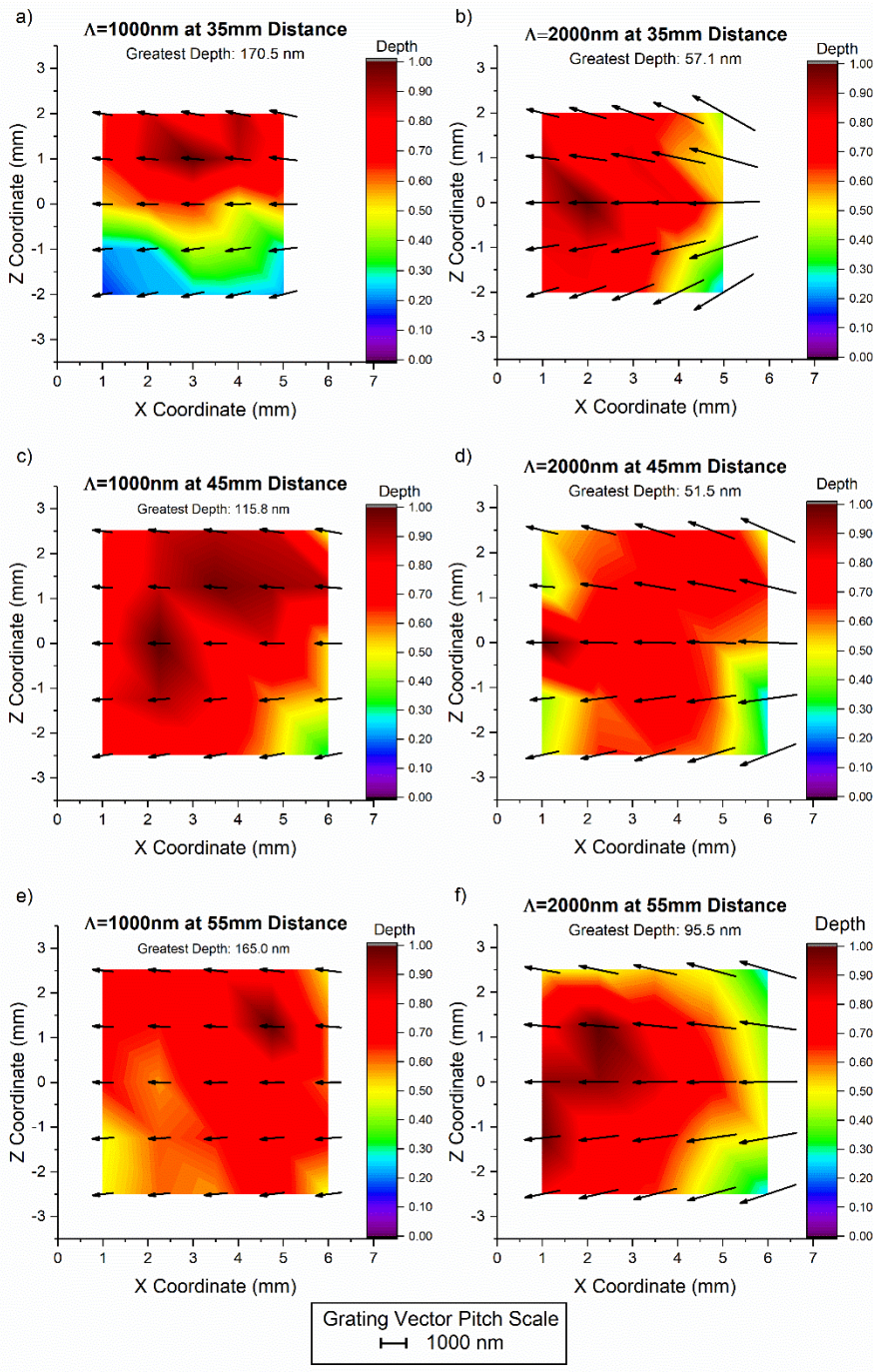

Figure 4.9: Experimental non-uniform SRG written at a central pitch values of $\Lambda = 1000$ nm (left) and $\Lambda = 2000$ nm (right) and lens positions of $f = 35$ mm, $f = 45$ mm, and $f = 55$ mm.

Figure 4.9 shows the effect that varying the lens position has on the grating profile is consistent at various central pitches and is proportional to the grating central pitch.

4.4 Comparison of Experimental and Theoretical Results

The surface profiles of non-uniform SRGs have been mapped both through experimental fabrication and theoretical modeling in Section 4.1 and 4.2. The resulting local grating pitch values and vector orientations were then used to produce a vector plot of the SRG surface at four central pitches specified in Section 4.1 using 25 X-Z coordinates on the grating surface. Identical central pitch values, lens positions, and sampling coordinates were selected for the experimental and theoretical analysis of the gratings to provide a foundation for which to compare results and validate the fabrication method.

4.4.1 Comparison of the Grating Pitch Variation

From Figure 4.4 and Figure 4.7, the chirping that is produced in the grating pitch is caused by the divergence of the laser beam. It is also clear from the two figures that the rate at which the local grating pitch changes across the grating surface is not constant for gratings written at various central pitch values. Therefore, by taking the difference between the grating local pitch at two consecutive analysis coordinates, a value for the average grating pitch rate of change for each of the twelve experimentally inscribed SRGs was generated. A similar analysis of the chirping rate for the theoretically produced non-uniform SRGs was conducted, and the average chirping rate values for each SRG were calculated. The value was set to be a percentage of the central pitch of the specified grating, and the results can be seen in Figure 4.10.

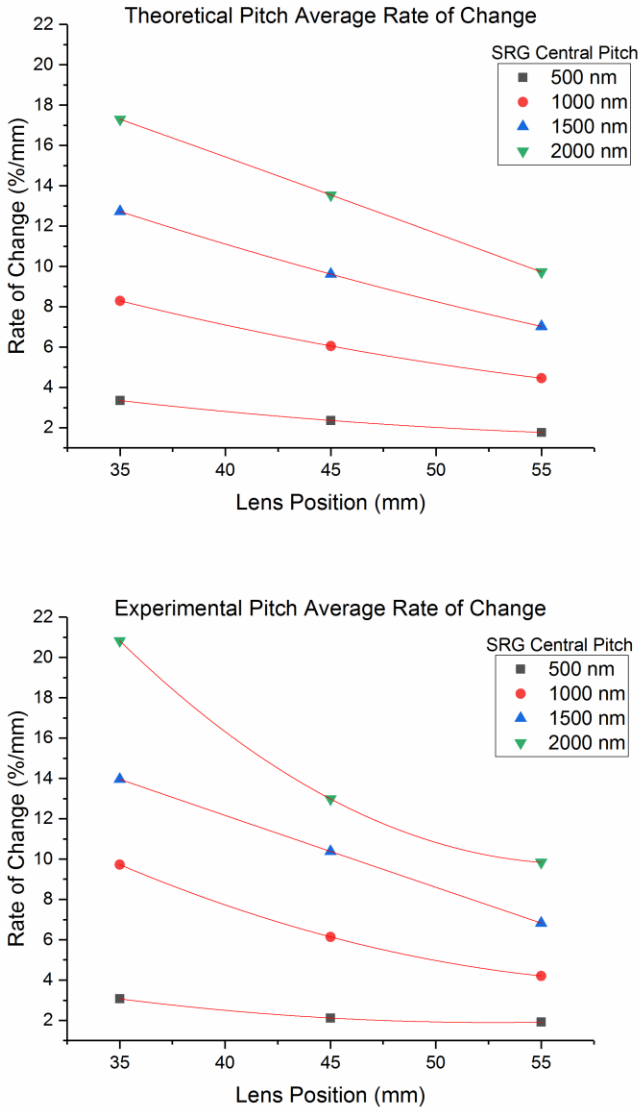

Figure 4.10: Comparison of the average chirping rate across the surface of non-uniform SRGs fabricated experimentally and theoretically at central pitch values of $\Lambda = 500$ nm, $\Lambda = 1000$ nm, $\Lambda = 1500$ nm, and $\Lambda = 2000$ nm and lens positions of $f = 35$ mm, $f = 45$ mm, and $f = 55$ mm.

A comparison of the results presented in Figure 4.10 show a similar trend between the experimental and theoretical results, with the chirping rate consistently being higher at closer lens positions, and with an average chirping rate value increase that is linearly proportional to the increase in the central pitch value. The discrepancies

observed between the values of the theoretical and experimental chirping rate can be attributed to error in the scanning position on the experimental SRG surface, or the misalignment of the lens during the inscription process.

The average chirping rate values were generated by averaging the difference between the pitch increase between two consecutive analysis coordinates along the X axis. What was found however is that the chirping rate of the SRGs is not constant across the SRG surface but rather increases from left to right consistently for all samples. The average values generated in for Figure 4.10 show the averages of this increase, but do not display the chirping rate increase along the X-axis. An example of the rate increase on the surface of a SRG with central pitch $\Lambda = 2000$ nm and lens distance $f = 35$ mm is shown in Table 4.1.

Table 4.1: Distribution of the chirping rate taken between the specified X-Z coordinates across the surface of a non-uniform SRG written at a central pitch value of $\Lambda = 2000$ nm and lens position of $f = 35$ mm. Chirping rate is presented as a percentage of the central grating pitch.

X-Z coordinate (mm)	1.0– 2.0	2.0– 3.0	3.0– 4.0	4.0– 5.0	Average Chirping Rate
2.0	10.7 %	14.0 %	21.5 %	38.6 %	21.2 %
1.0	10.3 %	14.3 %	21.9 %	36.0 %	20.6 %
0	10.9 %	13.7 %	23.4 %	35.6 %	20.9 %
-1.0	10.9 %	14.5 %	23.4 %	36.1 %	21.2 %
-2.0	10.9 %	14.3 %	24.6 %	30.9 %	20.2 %
					20.8 %

It is shown in Table 4.1 that the increasing chirping rate is consistent along the Z-axis, once again illustrating that the Z coordinate does not affect the grating pitch.

4.4.2 Comparison of Grating Vector Variation

Similarly to the grating chirping rate, the rate at which the grating vector changes across the surface of a SRG is depended on the grating central pitch. It can be seen from the vector plots that at higher central pitch values, the grating vector orientation will change more rapidly across the surface than at lower central pitch values. The rate of change in the grating vector orientation was calculated for the twelve SRG cases by calculating the angle between two grating vectors at consecutive X-Z coordinates on the surface. The average rate of change for the entire SRG surface was then calculated, and the results are shown in Figure 4.11.

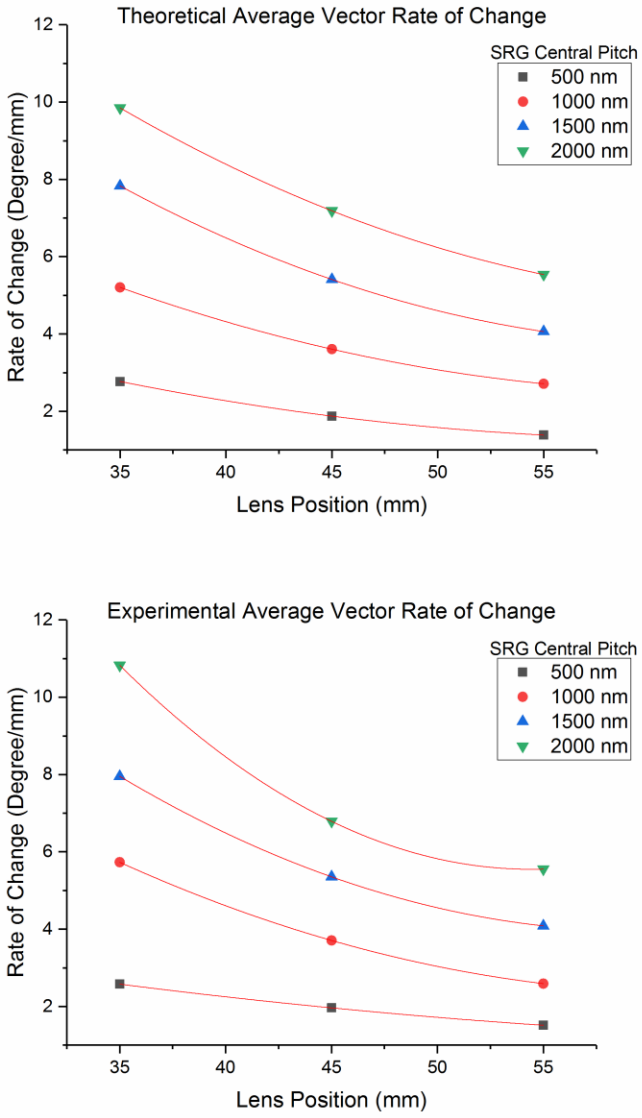

Figure 4.11: Comparison of the average grating vector rate across the surface of non-uniform SRGs fabricated experimentally and theoretically at central pitch values of $\Lambda = 500$ nm, $\Lambda = 1000$ nm, $\Lambda = 1500$ nm, and $\Lambda = 2000$ nm and lens positions of $f = 35$ mm, $f = 45$ mm, and $f = 55$ mm.

The theoretical and experimental results for the grating vector rate of change once again closely match, with small variations between the two. The trend however is identical to that discovered during the analysis of the grating chirping rate, with

higher central pitch values generating higher grating vector rates of change. From the theoretical results, the increase in the average rate of change seems to be linearly proportional to the increase in grating central pitch. The SRGs written at closer lens positions also produce more rapid increases in the grating vector rate of change between identical grating central pitches with the relationship between the three lens positions analysed herein appearing to be linearly increasing proportionally to the proximity of the lens to the azobenzene surface. The discrepancies observed between the theoretical model can once again be attributed to the misalignment of the scanning origin while conducting grating surface scans using the AFM, or error in the alignment of the lens when writing the gratings.

The results shown in Figure 4.11 illustrate the average rate of increase of the grating vector orientation along the Z-axis of the SRGs at the specified parameters. The rate of change in the grating vector orientation is constant along the Z-axis, with the difference in the grating vector orientation being approximately equivalent between two subsequent points. The rate of change does however increase as the position along the X-axis increases. An example of the distribution for the grating vector rate of change across the surface of a SRG written experimentally at central pitch $\Lambda = 2000$ nm and lens position $f = 35$ mm is shown in Table 4.2.

Table 4.2: Distribution of the grating vector rate of change taken between the specified X-Z coordinates across the surface of a non-uniform SRG written at a central pitch value of $\Lambda = 2000$ nm and lens position of $f = 35$ mm.

X-Z coordinate (mm)	1.0	2.0	3.0	4.0	5.0
2.0 – 1.0	7.4°	8.4°	9.0°	11.3°	13.9°
1.0 – 0.0	8.0°	9.0°	11.5°	12.3°	17.5°
0.0 – -1.0	7.3°	9.5°	10.7°	13.2°	16.5°
-1.0 – -2.0	7.5°	8.2°	9.3°	12.6°	13.4°
Average Grating Vector Rate of Change	7.6°	8.8°	10.1°	12.3°	15.3°
					10.8°

The information provided in Table 4.2 shows that the local grating pitch has an affect on the orientation of the grating vector. Since the grating pitch increases from left to right on the grating surface, the rate of change in the grating vector orientation will also increase.

4.4.3 Comparison of the Modulation Depth and Irradiance Distribution

The most evident discrepancy between the experimental SRG results and the theoretical model produced is the difference in the modulation depth and irradiance

profile across the SRG surfaces in Figure 4.4 and Figure 4.7. A brief analysis has been conducted to attribute possible factors in the experimental procedure that may have contributed to this difference such as the lens position, the scanning procedure, and the correlation between the *cis-trans* photoisomerization of the gDR1 film to the irradiance of the incident laser beam.

When constructing the theoretical model for the irradiance distribution, the total irradiance was assumed to be directly proportional to the grating modulation depth that would be inscribed on the gDR1 thin film, implying that the increase in the irradiance at a point on the film's surface would correlate directly to an equivalent increase in the grating modulation depth. This however is most likely not the case [36]. Although the photoresponsive properties of gDR1 can be correlated to the laser beam irradiance incident on the film's surface, the relationship is not assumed to be linear, with small decreases or increases in incident irradiance having possibly large-scale effects on the grating modulation depth profile. It is for this reason that an optimization process was conducted in order to determine the optimal exposure times for the irradiating laser when fabricating the experimental SRGs.

The specific properties of the inscribing laser can also affect the grating modulation depth across the non-uniform SRG. The Gaussian profile of the irradiating laser was not accounted for when constructing the theoretical model of the irradiance distribution. The assumption was made that after passing through the spatial filter, the irradiance distribution across the area of the beam would be effectively constant. In reality, a Gaussian profile, although reduced by the spatial filter, does still exist in the distribution of irradiance.

Any abnormalities or imperfections in the film surface could influence the local grating depth as well. These include any micro-particles or bubbles trapped under the film's surface that would affect the film quality, or any abnormalities in the localized film thickness from the spin coating process. Imperfections on the Lloyd's mirror surface could also contribute to a decreased irradiance on the azobenzene film from the beam being reflected.

Although, the irradiance distribution model does not reflect the extremes seen in the grating modulation depth profile, there are minor similarities between the distribution, and location of the extremes between the two methods. This indicates that future work into developing a more sophisticated theoretical model while taking into consideration the physical properties of the gDR1 thin film is possible to more closely reflect experimental grating depth modulation in the production of non-uniform SRGs.

4.5 Discussion of Future Work

The analysis and discussion in this chapter presented a model for the inscription of non-uniform SRGs using a Direct Interference Lithography Patterning technique. Using the numerical model, the effect of manipulating the grating central pitch and lens position on the inscribed grating profile can be predicted. Future work on the development of non-uniform SRGs could include the design of a control system to take advantage of the broad spectrum of grating parameters found on a single non-uniform SRG and exploring the applications of non-uniform SRGs in nano-systems, both of which will be briefly expanded on in the following paragraphs.

SRG applications require fine tuned grating profile properties, and while the existing numerical model can predict the profile, it does not currently provide a direct solution for locating the desired grating properties on the sample surface. By applying the experimental and theoretical work presented in Chapter 2 to Chapter 4 of this thesis, a numerical solution relating profile properties to SRG coordinates could be developed. Using this solution, a control system could be built for diffraction grating application in order to use a single non-uniform grating to generate a variety of diffraction properties by accessing specific areas on the non-uniform SRG. Using a control system, when the diffraction parameters of the grating required changes, the system could calculate the exact position on the SRG surface those parameters are located and rotate and reposition the grating surface to meet the needs of the system.

Non-uniform SRGs also have a number of future applications in nanoplasmonics and surface plasmon resonance. As discussed in Chapter 1, uniform SRGs have been applied to generate surface plasmon polaritons on metal surfaces. Chirped uniform gratings have been applied to increase the full width half maximum bandwidth of the plasmon polariton induction wavelength. The application of non-uniform SRGs to surface plasmon induction would provide control over the bandwidth of the surface plasmon induction wavelength, as well as plasmon induction at a variety of light polarizations based on the orientation in the grating vector. Surface plasmons induced by surface relief gratings have been applied to solar technology, and have already been shown to generate a photocurrent in the cell [65]. The induced current generated is based on the orientation of the grating and the grating pitch, as only electromagnetic waves with transverse-magnetic polarization with respect to the grating orientation and wavelength proportional to the grating pitch will generate surface plasmon resonance. Due to the chirped pitch and non-uniform structure of the gratings generated in this thesis, there is the possibility of applying this technology to generate photocurrent at a wider bandwidth of both

wavelengths and light polarizations. Additionally, the direction of surface plasmon propagation across a metallic surface can also be controlled using non-uniform surface relief gratings. The control over the change in the grating vector orientation will allow for the manipulation of the surface plasmon propagation direction. This application could be beneficial in nano-system and nano-electronic devices, when the generation of localized charge could be induced and manipulated simply using a light source and a non-uniform SRG.

The developed theoretical model has the potential to produce the grating pattern of a SRG fabricated using additional optical systems once the appropriate interference phase equation has been developed. Therefore, should more intricate SRG patterns be desired through the addition of other lenses or irradiating lasers, the equations for irradiance and interference phase could be solved analytically and inserted into the program to map the resulting SRG at specified X-Z coordinates.

Chapter 5 Conclusion

The inscription of non-uniform SRG on azobenzene thin films was described in this thesis both from an experimental fabrication process and a theoretical model. The work focused around developing a theoretical model from the analytic expression for the interference phase of recombined coherent laser beams, and then comparing the generated models to experimental SRG profiles as measured using an AFM scan of fabricated non-uniform SRGs. The results were compared in order to validate the fabrication method.

The analytic expression of the interference phase was derived for the recombination of a laser beam incident on a Lloyd's mirror interferometer. The derivation used a geometric ray trace technique that used the electromagnetic wave properties of a collimated irradiating laser. The general expressions for wave vectors of a laser beam recombining on an azobenzene surface from the interferometer were derived and applied to generate an analytic expression for the recombined interference phase. A path length difference was then added to the laser beam component incident on the azobenzene surface, modelling the addition of a spherical lens in order to generate a divergent incident beam. The total expression for the recombined laser irradiance was also derived, incorporating the interference phase to account for the irradiance interference term.

A Python code was written to apply the analytic expressions to iteratively produce a map of the laser interference phase across areas of 5 μm and 10 μm width and height at 25 evenly spaced X-Z coordinates across the surface of a theoretical SRG. The local grating pitch and vector information from the generated theoretical SRGs was analyzed using separate iterative processes. A separate code was produced to generate a theoretical irradiance profile from the recombined beams.

The experimental non-uniform SRGs were fabricated using a Verdi V5 diode pumped continuous wave laser set-up, which generated a collimated circularly polarized coherent laser beam at a wavelength of $\lambda = 532$ nm. A 5.72 mm spherical lens and fabricated lens holder were used to manipulate the half of the laser beam incident on a photoresistive gDR1 thin film to generate the non-uniform interference pattern. The non-uniform SRGs were fabricated with central pitch values of $\Lambda = 500$ nm, $\Lambda = 1000$ nm, $\Lambda = 1500$ nm, and $\Lambda = 2000$ nm at lens positions of $f = 35$ mm, $f = 45$ mm, and $f = 55$ mm. The grating profiles were analyzed using a Bruker Dimension Edge AFM.

The results generated from both the experimental fabrication and theoretical model of non-uniform SRGs were presented using a vector map showing the grating pitch and vector information at 25 coordinates across the SRG's surface. Through the comparison of the experimental and theoretical results, the local grating pitch and vector appeared to be consistent across the surface of the SRGs. A modulation depth analysis was also conducted on the experimentally fabricated non-uniform SRGs at the selected 25 X-Z coordinates, and the data was compared to a theoretical model of the total incident irradiance on the surface of the azobenzene thin film during the inscription process. Although the distribution of the deeper and shallower sections of the SRGs did agree in some cases, the differences between the depths recorded experimentally were far more extreme than the differences in the theoretical irradiance values mapped across the SRG surface. The grating chirping rate and vector orientation rate of change were then compared between non-uniform SRGs fabricated at central grating pitch values of $\Lambda = 500$ nm, $\Lambda = 1000$ nm, $\Lambda = 1500$ nm, and $\Lambda = 2000$ nm and at lens positions of $f = 35$ mm, $f = 45$ mm, and $f = 55$ mm for the experimentally inscribed and theoretically modeled SRGs. It was found that by increasing the grating central pitch and decreasing the distance between the spherical lens and the azobenzene surface onto which the grating was being inscribed, the rate of change in both parameters could be increased. It was also found that the rate of change was not consistent across the surfaces of the SRGs with the chirping rate increasing from left to right on the sample surface, and the grating vector rate of change also increasing from left to right on the sample surface, with only slight variations along the vertical axis.

Using the results generated from both the experimental and theoretical models, future work could be done to fabricate an automated program to generate the parameters for non-uniform SRGs with desired surface parameters or grating vector and pitch rates of change. With more research, automated programs could be developed to apply the diffraction grating properties of non-uniform SRGs to obtain a wide variety of diffraction applications from a single non-uniform SRG. Future research into their applicability in the field of surface plasmonics for both the generation of local surface plasmon polaritons and for guiding propagating surface plasmons can be done to incorporate this technology into emerging solar energy systems and nano-electronics.

Furthermore, future research is required to better understand the relationship between the gDR1 azobenzene films and the laser irradiance to better explain the correlation between the incident irradiance and the modulation depth distribution of the gratings. With better understanding, a more accurate model could be developed to better reflect the laser conditions that influence the inscriptions of the grating

profile on the azobenzene film. This information could be used to develop a more accurate theoretical model of the modulation depth of non-uniform SRGs.

This project was undertaken to develop and model a repeatable and precise fabrication method for non-uniform SRGs. The experimental and theoretical work done demonstrated that this fabrication method could produce finely tuned and controllable non-uniform grating profiles by manipulating the central pitch and lens distance parameters. The mask-less laser lithography technique employed also ensured that this method was efficient and cost effective. The modified Lloyd's mirror interferometer used and validated over the course of this thesis will therefore make research and development of non-uniform SRG applications much more attainable for future research and developments in nano-optics.

References

[1] E. Loewen and E. Popov, *Diffraction Gratings and Applications*. 1997.

[2] W. J. Smith, *Modern Optical Engineering*. 2008.

[3] E. Hecht, *Optics*. 2002.

[4] S. Massenot, R. Chevallier, J. L. de Bougrenet de la Tocnaye, and O. Parriaux, "Tunable grating-assisted surface plasmon resonance by use of nano-polymer dispersed liquid crystal electro-optical material," *Opt. Commun.*, 2007.

[5] T. K. Gaylord and M. G. Moharam, "Analysis and applications of optical diffraction by gratings," *Proc. IEEE*, vol. 73, no. 5, pp. 894–937, 1985.

[6] L. Li, "New formulation of the Fourier modal method for crossed surface-relief gratings," *J. Opt. Soc. Am. A*, vol. 14, no. 10, p. 2758, 1997.

[7] M. G. Moharam, D. A. Pommet, E. B. Grann, and T. K. Gaylord, "Stable implementation of the rigorous coupled-wave analysis for surface-relief gratings: enhanced transmittance matrix approach," *J. Opt. Soc. Am. A*, vol. 12, no. 5, p. 1077, 1995.

[8] A. Biswas, I. S. Bayer, A. S. Biris, T. Wang, E. Dervishi, and F. Faupel, "Advances in top-down and bottom-up surface nanofabrication: Techniques, applications & future prospects," *Advances in Colloid and Interface Science*, vol. 170, no. 1–2. pp. 2–27, 2012.

[9] T. Suntola and J. Antson, "Method for producing compound thin films," 1977.

[10] H. Kim, H. B. R. Lee, and W. J. Maeng, "Applications of atomic layer deposition to nanofabrication and emerging nanodevices," *Thin Solid Films*, vol. 517, no. 8, pp. 2563–2580, 2009.

[11] L. C. Palmer and S. I. Stupp, "Molecular self-assembly into one-dimensional nanostructures," *Acc. Chem. Res.*, vol. 41, no. 12, pp. 1674–1684, 2008.

[12] S. Shukla and M. Sastry, "Probing differential Ag+–nucleobase interactions with isothermal titration calorimetry (ITC): Towards patterned DNA metallization," *Nanoscale*, vol. 1, no. 1, p. 122, 2009.

[13] J. D. Le, Y. Pinto, N. C. Seeman, K. Musier-Forsyth, T. A. Taton, and R. A. Kiehl, “DNA-Templated Self-Assembly of Metallic Nanocomponent Arrays on a Surface,” *Nano Lett.*, vol. 4, no. 12, pp. 2343–2347, 2004.

[14] N. Bowden, W. T. S. Huck, K. E. Paul, and G. M. Whitesides, “The controlled formation of ordered, sinusoidal structures by plasma oxidation of an elastomeric polymer,” *Cit. Appl. Phys. Lett*, vol. 75, 1999.

[15] W. Yeh, J. Kleingartner, and A. C. Hillier, “Wavelength Tunable Surface Plasmon Resonance-Enhanced Optical Transmission Through a Chirped Diffraction Grating,” *Lett. to Anal. Chem.*, vol. 82, no. 12, pp. 4988–4993, 2010.

[16] N. Bowden, S. Brittain, A. G. Evans, J. W. Hutchinson, and G. M. Whitesides, “Spontaneous formation of ordered structures in thin filmsofmetals supported on an elastomeric polymer,” *Nature,* vol. 393, pp. 146–149, 1998.

[17] Y. Yan, Z. Hu, X. Zhao, T. Sun, S. Dong, and X. Li, “Top-down nanomechanical machining of three-dimensional nanostructures by atomic force microscopy,” *Small*, vol. 6, no. 6, pp. 724–728, 2010.

[18] J. Sun, X. Luo, W. Chang, J. M. Ritchie, J. Chien, and A. Lee, “Fabrication of periodic nanostructures by single-point diamond turning with focused ion beam built tool tips,” *J. Micromechanics Microengineering*, vol. 22, 2012.

[19] Q. Guo, X. Teng, and H. Yang, “Overpressure contact printing,” *Nano Lett.*, vol. 4, no. 9, pp. 1657–1662, 2004.

[20] B. D. Terris *et al.*, “Ion-beam patterning of magnetic films using stencil masks,” *Appl. Phys. Lett.*, vol. 75, no. 3, p. 403, 1999.

[21] C. A. Volkert and A. M. Minor, “Focused Ion Beam Microscopy and Micromachining,” *MRS Bull.*, vol. 32, no. 5, pp. 389–399, 2007.

[22] Y. K. Kim, A. J. Danner, J. J. Raftery, and K. D. Choquette, “Focused ion beam nanopatterning for optoelectronic device fabrication,” *IEEE J. Sel. Top. Quantum Electron.*, vol. 11, no. 6, pp. 1292–1297, 2005.

[23] T. Schenkel, V. Radmilovic, E. A. Stach, S.-J. Park, and A. Persaud, “Formation of a few nanometer wide holes in membranes with a dual beam focused ion beam system,” *J. Vac. Sci. Technol. B Microelectron. Nanom. Struct.*, vol. 21, no. 6, p. 2720, 2003.

[24] L. R. Harriott, “Limits of lithography,” *Proc. IEEE*, vol. 89, no. 3, pp. 366–

374, 2001.

[25] N. C. R. Holme, L. Nikolova, S. Hvilsted, P. H. Rasmussen, R. H. Berg, and P. S. Ramanujam, “Optically Induced Surface Relief Phenomena in Azobenzene Polymers,” *Appl. Phys. Lett.*, vol. 74, no. 4, p. 519, 1999.

[26] D. Y. Kim, L. Li, X. L. Jiang, V. Shivshankar, J. Kumar, and S. K. Tripathy, “Laser-induced holographic surface relief gratings on nonlinear optical polymer films,” *Macromolecules*, vol. 28, no. 26, p. 8835, 1995.

[27] T. Kondo *et al.*, “Holographic lithography of periodic two- and three-dimensional microstructures in photoresist SU-8,” *Opt. Express*, vol. 14, no. 17, p. 7943, 2006.

[28] J. A. Delaire and K. Nakatani, “Linear and Nonlinear Optical Properties of Photochromic Molecules and Materials,” *Chem. Rev.*, vol. 100, no. 5, pp. 1817–1845, 2000.

[29] M. Hendrikx, A. Schenning, M. Debije, and D. Broer, “Light-Triggered Formation of Surface Topographies in Azo Polymers,” *Crystals*, vol. 7, no. 8, p. 231, 2017.

[30] W. Commons, “Azobenzene isomerization.” [Online]. Available: https://commons.wikimedia.org/wiki/File:Azobenzene_isomerization.svg. [Accessed: 21-Feb-2018].

[31] P. Rochon, E. Batalla, and A. Natansohn, “Optically induced surface gratings on azoaromatic polymer films,” *Appl. Phys. Lett.*, vol. 66, no. 2, pp. 136–138, 1995.

[32] J. Paterson and A. Natansohn, “Optically inscribed surface relief diffraction gratings on azobenzene- containing polymers for coupling light into slab waveguides,” *Appl. Phys. Lett.*, vol. 69, no. 22, pp. 3318–3320, 1996.

[33] E. Ishow *et al.*, “Structural and photoisomerization cross studies of polar photochromic monomeric glasses forming surface relief gratings,” *Chem. Mater.*, vol. 18, no. 5, pp. 1261–1267, 2006.

[34] J. Kumar, L. Li, X. L. Jiang, D.-Y. Kim, T. S. Lee, and S. Tripathy, “Gradient Force: The Mechanism for Surface Relief Grating Formation in Azobenzene Functionalized Polymers,” *Appl. Phys. Lett.*, vol. 72, no. 17, p. 2096, 1998.

[35] N. S. Yadavalli and S. Santer, “In-situ atomic force microscopy study of the mechanism of surface relief grating formation in photosensitive polymer films,” *J. Appl. Phys.*, vol. 113, no. 22, p. 224304, 2013.

[36] R. Kirby, R. G. Sabat, J.-M. Nunzi, and O. Lebel, “Disperse and disordered: a mexylaminotriazine-substituted azobenzene derivative with superior glass and surface relief grating formation,” *J. Mater. Chem. C*, vol. 2, no. 5, pp. 841–847, 2014.

[37] M. Matsuhara and K. 0 Hill, “Optical-Waveguide Band-Rejection Filters: Design,” *Appl. Opt.*, vol. 13, no. 12, p. 2886, 1974.

[38] L. F. Johnson, G. W. Kammlott, and K. A. Ingersoll, “Generation of periodic surface corrugations,” *Appl. Opt.*, vol. 17, no. 8, p. 1165, 1978.

[39] R. J. Stockermans and P. Rochon, “Experimental demonstration of photonic bandgaps in azopolymer resonant waveguide grating systems,” *J. Opt. Soc. Am. A*, vol. 24, no. 8, pp. 2457–2463, 2007.

[40] U. Tiwari *et al.*, “Tunable wavelength division multiplexing channel isolation filter based on dual chirped long-period fiber gratings,” *Opt. Lett.*, vol. 36, no. 19, p. 3747, 2011.

[41] S. M. Saltiel *et al.*, “Nonlinear diffraction from a virtual beam,” *Phys. Rev. Lett.*, vol. 104, no. 8, p. 83902, 2010.

[42] H. J. Lezec *et al.*, “Beaming Light from a Subwavelength Aperture,” *Science*, vol. 297, no. 5582. pp. 820–822, 2002.

[43] R. D. Boyd *et al.*, “High-efficiency metallic diffraction gratings for laser applications,” *Appl. Opt.*, vol. 34, no. 10, p. 1697, 1995.

[44] D. Nevejans *et al.*, “Compact high-resolution spaceborne echelle grating spectrometer with acousto-optical tunable filter based order sorting for the infrared domain from 22 to 43 μm,” *Appl. Opt.*, vol. 45, no. 21, p. 5191, 2006.

[45] T. O. Sharpee, H. Sugihara, A. V. Kurgansky, S. P. Rebrik, M. P. Stryker, and K. D. Miller, “Adaptive filtering enhances information transmission in visual cortex,” *Nature*, vol. 439, no. 7079, pp. 936–942, 2006.

[46] C. J. Kramer, “Novel Surface-Relief Diffraction Grating (Patent),” 2003.

[47] J. M. Miller, “Surface Relief Difraction Grating (Patent),” 2011.

[48] W. L. Barnes, A. Dereux, and T. W. Ebbesen, “Surface Plasmon Subwavelength Optics,” *Nature*, vol. 424, no. August, pp. 824–831, 2003.

[49] S. A. Maier, *Plasmonics: Fundamentals and Applications*, 1st ed. New York: Pringer Science+Buisness Media LLC, 2007.

[50] A. Otto, “Excitation of nonradiative surface plasma waves in silver by the method of frustrated total reflection,” *Zeitschrift fur Phys.*, vol. 216, no. 4, pp. 398–410, 1968.

[51] B. Hecht, H. Bielefeldt, L. Novotny, Y. Inouye, and D. W. Pohl, “Local excitation, scattering, and interference of surface plasmons,” *Phys. Rev. Lett.*, 1996.

[52] R. H. Ritchie, E. T. Arakawa, J. J. Cowan, and R. N. Hamm, “Surface-plasmon resonance effect in grating diffraction,” *Phys. Rev. Lett.*, vol. 21, no. 22, pp. 1530–1533, 1968.

[53] E. Bailey and R. G. Sabat, “Surface plasmon bandwidth increase using chirped-pitch linear diffraction gratings,” *Opt. Express*, vol. 25, no. 6, pp. 136–138, 2017.

[54] S. Pillai, K. R. Catchpole, T. Trupke, and M. A. Green, “Surface plasmon enhanced silicon solar cells,” *J. Appl. Phys.*, vol. 101, no. March, p. 93105, 2007.

[55] J. Leibold, P. Snell, O. Lebel, and R. G. Sabat, “Design and fabrication of constant-pitch circular surface-relief diffraction gratings on disperse red 1 glass,” *Opt. Lett.*, vol. 39, no. 12, p. 3445, 2014.

[56] J. Leibold and R. G. Sabat, “Laser-induced controllable chirped-pitch circular surface-relief diffraction gratings on AZO glass,” *Photonics Res.*, vol. 3, no. 4, pp. 158–163, 2015.

[57] D. J. Griffiths, *Introduction to Electrodynamics - Electrodynamics*. 1999.

[58] D. J. Griffiths, *Introduction to Electrodynamics - Electromagnetic Waves*. 1999.

[59] G. C. King, *Vibrations and Waves*. 2009.

[60] R. G. Sabat, “Superimposed surface-relief diffraction grating holographic lenses on azo-polymer films,” *Opt. Express*, vol. 21, no. 7, p. 8711, 2013.

[61] J. L. Vossen *et al.*, *Thin Film Processes II*. Academic Press, Inc., 1991.

[62] Bruker, “Dimension Edge with ScanAsyst: Most Accessible High-Performance AFM.” pp. 1–8.

[63] B. N. Inc., “Bruker AFM Probes,” 2018. [Online]. Available: https://www.brukerafmprobes.com/Product.aspx?ProductID=3759.

[64] Bruker, “ScanAsyst: Exclusive Self-Optimizing AFM Imaging.” pp. 1–4.

[65] J. Jefferies and R. G. Sabat, “Surface-relief diffraction gratings’ optimization for plasmonic enhancements in thin-film solar cells,” *Prog. Photovoltaics Res. Appl.*, vol. 22, pp. 648–655, 2014.

Appendices

Appendix A Analysis of Theoretical SRGs Using Python Code

A.1 Phase Model

The theoretical SRG phase map was produced using an iterative script designed using the Python programming language. The script operates as an exterior shell, programmed to handle and sort the produced data, and a sub-script that iteratively calculates the interference phase value at the specified X-Z coordinates. An overview of the process executed by the python script is illustrated in Figure A.1. Each step of the computational process shown below will be described in detail to explain its role in the generation of the phase map.

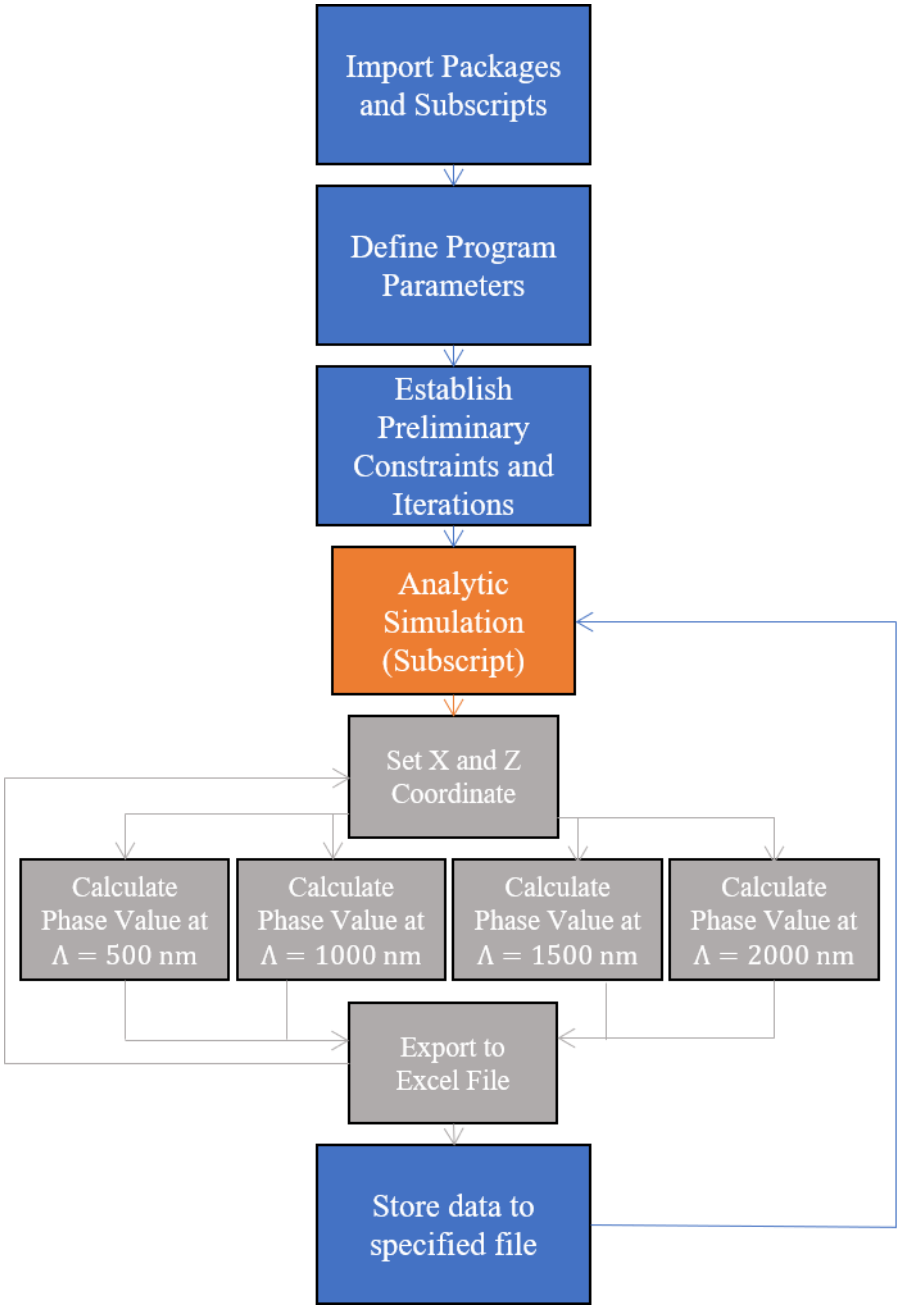

Figure A.1: Illustrative map of the Python programming procedure used for the production of the phase modeling of non-uniform SRGs.

Importing Python Packages

The main shell begins by importing three python packages: the NumPy Math package, the AnalyticSim subscript, and the Python Compile package. Numpy Math is a coding package designed to solve analytic problems with pre-programmed mathematical values and functions. The AnaliticSim subscript is a user written subscript designed to generate the interference phase value of the recombined beams at a given X-Z coordinate. Finally, the Python Compile package is a package used to compile the data generated from the subscript into a format that can be applied in the main shell.

Define Program Parameters

The values for the lens focal length and laser wavelength were defined in this section. These two values are constants throughout the SRG inscription process with other variables defined later in the subscript. The values for the mirror angle with respect to the optical axis were also defined for each of the four central pitches – 500 nm, 1000 nm, 1500 nm, and 2000 nm – using Equation (2.41). Finally, three NumPy matrices were created for the three lens positions, f, that would be used throughout the theoretical modeling – 35 mm, 45 mm, and 55mm. These matrices contain the file information necessary to store the output data generated from the Python code into Excel files for future data management.

Establishing Preliminary Constraints and Iterations

A set of 25 coordinate positions on the surface of the generated theoretical SRGs were chosen to analyze the theoretical phase profile. The points were evenly spaced across a 4 mm x 4 mm square for a lens distance of $f = 35$ mm and across a 5 mm x 5 mm square for a lens distance of $f = 45$ mm and $f = 55$ mm. The modeling areas necessary to produce a phase map from which all the required information could be extrapolated was determined to be 5 μm in width and height for a central pitch value of $\Lambda = 500$ nm and $\Lambda = 1000$ nm, and 10 μm in width and height for a central pitch values of $\Lambda = 1500$ nm and $\Lambda = 2000$ nm. Therefore, the beginning coordinates for the X and Z positions on the theoretical SRG were defined, and an iterative loop was created.

In addition to defining the modeling areas, an iterative loop was also produced to control the lens distance, f, as the program was running. Once the iterations had completed mapping all the points for all four central pitch values at each of the 25 positions with a lens distance of $f = 35$ mm, the program would increase the lens position by 10 mm and restart the process for $f = 45$mm. The program would then do this one more time for a lens position of $f = 55$ mm.

A marker was written into the code to track the progress of the computations and to ensure that each SRG was being mapped properly at each of the three lens distances.

Analytic Computation Sub-script (AnalyticSim)

The AnalyticSim sub-script operates by analytically evaluating the phase value of the interfering beams at a single position, then iterating through the subsequent points to produce a three-dimensional map of the phase profile. The script begins by importing the necessary values from the main shell for the lens position, focal length, mirror angle, upper and lower X and Z constraints for each central pitch, and the file name to which data will be saved once the program is complete. It then imports two python packages, the NumPy Math package, and an Excel Write package. The Excel Write package is designed to directly export a specified data value to a defined Excel cell, sheet, and workbook.

The expression for the phase value, as seen in Equation (2.49), was then defined for each of the four central pitch values by using the necessary mirror angles to generate each pitch. A new workbook with four sheets was then generated using the Excel Write package, and each sheet was named according to the type of data that would be stored into it.

Four "for" loops were then constructed. Each loop was constrained in two dimensions by X and Z coordinate values centered around the main analysis point. An increment was set in order to generate 200 data points along both the X and Z axes, thereby producing a 40,000 data point matrix. Each phase value was determined individually for their respective position and then exported to a separate Excel file before the program calculated the following phase value. Two counting variables were also established in order to control the number of iterations executed by the two "for" loops governing the X coordinate and the Z coordinate. These counting variables were also used to govern the cell position in the Excel file to which the generated data would be stored. The iterative process completed an entire row of Z coordinates before increasing the X position value by the set increment.

The complete data matrix for each central pitch was saved to an individual Excel worksheet in a single workbook. A separate workbook was generated for each of the given 25 analysis coordinates. The document was then saved to a folder using a document name indicating the position on the grating surface for which the data had been derived.

This process produces four 40,000 point matrices modelling the three dimensional shape of a theoretical non-uniform SRG. The main shell would

iteratively run this subscript 75 times, to produce one workbook for each of the 25 X-Z coordinates at each of the three-lens distance.

A.2 Grating Pitch and Vector Calculations

Once the phase information has been generated, the data files can be used to calculate the pitch and grating vector information for the theoretical SRGs. This was achieved using a second main shell and three user written subscripts. A programming map illustrating the process used to generate these values is shown in Figure A.2.

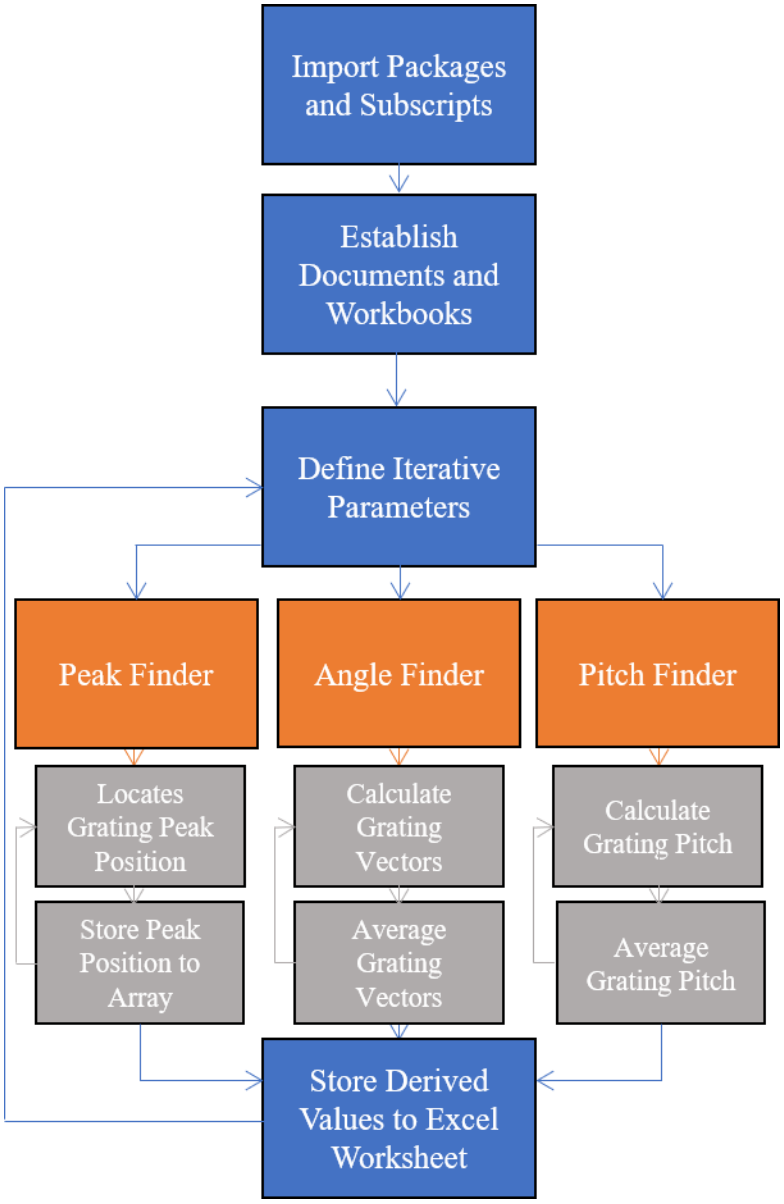

Figure A.2: Illustrative map of the Python programming procedure used for the analysis of the grating pitch and vector from the produced grating phase map information of non-uniform SRGs.

Importing Packages and Subscripts

The main shell begins by importing three python packages: The NumPy Math package, the Excel Write package, and the Python Compile package. It also imports three user written subscripts which are referred to as Angle Finder, Peak

Finder, and Pitch Finder. The names of the three subscripts identify their individual applications. The structure of each subscript will be described in the following sections. Each subscript is then compiled using the Python Compile package, to access the subscript files and convert the generated data into format compatible with the main shell.

Establishing Documents and Workbooks

Three arrays were created in the main shell, each with a list of document names that would be used to later create files for data storage. A new Excel workbook was then created with three sheets, each sheet associated with a lens distance, f. The individual sheets were then labelled by titling the columns with the name of the information that would later be stored there (eg. "Angle 500" for the angle value derived at a central pitch of $\Lambda = 500$ nm).

Defining Iterative parameters

The iterations in the main shell are based on the central X-Z coordinate used to map the interference phase in Section A.1. Two one-dimensional arrays are also created for storing the grating pitch and vector information that will be generated. Three imbedded for loops are then initiated. The first for loop defines the initial X coordinate and the incrementation that will be used to increase the X coordinate value. The second loop defines the initial Z coordinate, and the incrementation used to increase this value. The final loop defines the sheet number into which the derived information will be stored. The final loop contains within it all of the user written subscripts.

Peak Finder

The first subscript to be accessed is Peak Finder. This subscript locates the crests of the interference phase within the 40 000 data point matrices generated in Section A.1. It does this along four rows only. The reason for this is that the pitch value will not vary significantly across the sample area analyzed by the phase map, with only slight variations due to the resolution of the matrix. Therefore, the Peak Finder script scans one row of data, locating the positions of the local maxima and storing them into an established one-dimensional array. The row position on the phase map is then increased by 50 cells, and the process is repeated another three times. The located positions will be used by the remaining two subscripts to calculate the grating pitch and grating vector at each of the coordinates. The script then exports the position arrays to the main shell.

The main shell then accesses each of the position arrays and stores them as new arrays under the row value from which they were found in the phase map.

Angle Finder

The Angle Finder subscript operate by completing two primary tasks: calculating the granting vector using the grating peak positions found by the Peak Finder script, and averaging the angles calculated.

The grating vectors are determined first by importing the four peak arrays described above. Three new one-dimensional arrays are then created to store the derived grating vectors called Angles1, Angles2, and Angles3. A new for loop is opened in which the number of iterations are governed by the size of the three arrays. An iterative "for" loop uses the arrays denoting the positions of the grating peaks to calculate the direction of the grating vector. From observation of the produced theoretical phase maps, the direction of the grating vector for positions above and below the X-axis were known. Therefore, above the X-axis, the location of a grating peak at higher vertical positions in a phase map would have a higher value than those at lower vertical positions. This was applied by subtracting the peak coordinate values from two subsequent arrays. An angle was then found by dividing the difference by the distance separating the two rows from which the two data sets were taken, and finding the angle using a tangent function. The angle values were then stored in a new array and the iteration was repeated for the two subsequent data arrays.

The same steps were taken for calculating the grating vector below the X-axis, however the peak position values were known to mirror those above the Z axis. Therefore, the peak position would increase as the Z position decreased.

Upon completion of the calculation of all the grating vectors for a specific X-Z coordinate phase map, the three completed one-dimensional arrays containing the angle information were averaged. The three averaged values of these arrays were then in turn averaged, and the value was exported to the main shell as the grating vector direction for that particular X-Z coordinate.

Pitch Finder

The information generated by the Peak Finder subscript was also applied in order to find the grating pitch values across the theoretical SRG surface. The subscript begins by importing the one-dimensional arrays containing the peak coordinate information, along with the NumPy Math package. Three new one-dimensional arrays are also created and named Pitches1, Pitches 2, and Pitches 3.

Using an iterative process, set to a number of cycles equal to the size of the one-dimensional pitch arrays, the difference between the position of each peak and its subsequent peak is calculated. The units assigned to the difference value calculated is the number of data point between the two peaks. Therefore, knowing

that the matrix had dimensions of 200 by 200 data points, the difference is divided by 200. The result is then multiplied by 10,000 in order to convert the value to the scale being used by the main shell.

The calculated pitch values are then averaged by counting the total number of non-zero values in an array and storing it as an iteration number, summing all of the non-zero pitch values in that array, and dividing the result by the iteration number. The three averages were then, in turn, averaged, to determine the average pitch value the specified coordinate. This value was then exported to the main shell.

Storing the Grating Pitch and Vector Data

Once the grating vector and pitch values had been calculated for a given X-Z coordinate, the two values were exported to the appropriate Excel file and sheet. The entire process was conducted for each of the four grating central pitches, at each of the 25 coordinates. The document was then saved, and the lens distance was increased by 10 mm. This process was conducted for the remaining two lens positions of $f = 45$ mm and $f = 55$ mm.

A.3 Irradiance model

A separate irradiance model was generated at each of the X-Z coordinates used to generate a phase map. The motivation for this was to compare the theoretical irradiance distribution across a non-uniform SRG with the depth profile of an experimentally fabricated SRG. Since the irradiance of the inscribing laser beam directly influences the inscription depth, a hypothesis was made that there may be direct correlation between the experimental depth profile, and the theoretical irradiance profile.

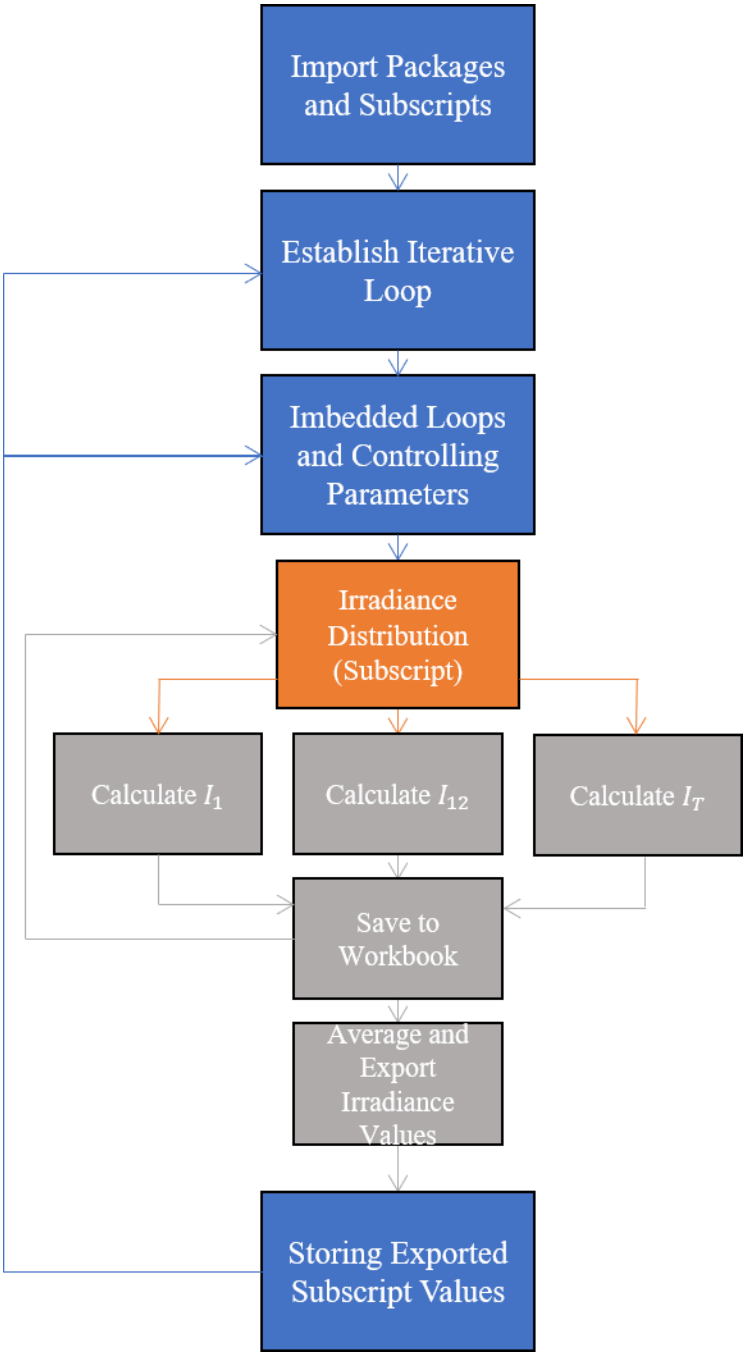

Figure A.3: Illustrative map of the Python programming procedure used for the modelling of the irradiance distribution across the surface of a non-uniform SRG.

Defining Variable and Importing Python Packages

The program begins by importing the NumPy Math package, the Excel Write package, and a user written subscript titled Irradiance Distribution 2. The subscript will be described in detail in the following paragraphs, however its primary role was to generate irradiance values at each coordinate, sum them, and export them to the main shell. The necessary variables and parameters needed to initiate the derivations are also defined. The laser irradiance and wavelength were set to the known values of the inscribing laser used for SRG fabrication. The lens dimensions and focal length were defined, and the measurements for the beam radius was set. Equations for the irradiating power of the direct and reflected laser beams were determined based on the laser irradiance and the irradiating area. Finally, the expressions for the beam divergence angle caused by the spherical lens, and the angle of the reflecting mirror at the four central pitches were defined, and the arrays establishing the desired Excel file names for data storage were created.

Establishing Iterative Loop

The main shell for the generation of the irradiance map applies a "while" loop in order to generate the necessary data matrices. The while loop is governed by the lens position with respect to the sample surface and is therefore repeated three times in the main shell for lens distance of $f = 35$ mm, $f = 45$ mm and for $f = 55$ mm. An iteration counter was defined in order to access the appropriate Excel workbook in which to store the generated data matrices.

For each iteration, a single work book is generated containing four sheets. Each sheet is dedicated to a single central pitch and contains the information for the averaged reflected irradiance, direct irradiance, total irradiance, as well as the coordinates at which they were derived.

Imbedded Loops and Controlling Parameters

A second loop is written to control the central pitch at which the irradiance is being analyzed. This loop is then imbedded with a another two "for" loops to control the coordinates being analyzed, with a total of 25 X-Z coordinates across the theoretical SRG surface. The modelling area at each coordinate is a square with 5 μm width and height centered around the X-Z coordinate. The necessary calculations were then conducted in order to derive the inscription surface distance along the lens axis from the focal point, and the area of the beam on the sample surface from the reflection off the mirror.

A controlling parameter is then set based on the interfering area of the divergent laser beam and the beam reflected by the mirror. Assuming the lens is perfectly centered, the beams on the inscribing surface overlap only within a specific

area based on the distance of the lens from the surface. For any coordinate outside of this area, the irradiance was set to zero. If the coordinate fell within the defined area, the irradiance from the beam reflected by the mirror was calculated as I_2.

Based on the current lens position, the appropriate file was then accessed for data storage in the following steps.

Irradiance Distribution Subscript

Once the required parameters had been established, the shell accessed the Irradiance Distribution subscript. This subscript begins by importing the required laser parameters, lens properties, coordinate information, central pitch, and document name from the main shell, along with the standard NumPy and Excel Write packages. The subscript also imports two new packages called Excel Read and Excel Utilize. These two packages work together to import existing data from a defined Excel file in a format that can be used by the python code.

A new workbook was created for the specific coordinates at which the irradiance map was being generated. Twelve sheets were created, four for the irradiance map generated from the diverging lens beam at each central pitch, four for the interference irradiance map at each central pitch, and four for the total irradiance map at each central pitch. A square matrix with height and width dimensions of 101 cells was then generated for each for the twelve conditions. Two "while" loops were written to control the incrementation of the X and Z positions around the central coordinate.

For each increment, the defined X and Z positions were used to calculate the final three irradiance terms. The irradiance term from the diverging beam was determined base on the distance of the inscribing surface from the laser focal point at each position. This was done by calculating the beam area at a given point based on the divergence angle of the beam. The irradiance was then calculated by dividing the power incident on the spherical lens by the beam area. The interference term was determined using Equation (2.34) and by applying Equation (2.49) for the interference phase, along with the calculated values of I_1 and I_2. Finally, the total irradiance value was calculated using Equation (2.27). The derived irradiance values for the defined central pitch were then stored into their respective Excel files and worksheets, as well as into their respective matrices. This process was iteratively repeated until each of the 10,201 data points were filled.

The matrices containing the calculated I_1, I_{12} and I_T values were then averaged to obtain an average irradiance values at the specified central X-Z coordinate. This was simply done using a matrix averaging function provided by the NumPy Math package.

The document containing the irradiance maps was then saved, and the averaged values for I_1, I_{12}, and I_T were exported to the main shell.

Storing Exported Subscript Values

The average irradiance values that were derived in the subscript were imported into the main shell in the form of an array containing three data points. The values were then individually accessed and stored into their respective Excel worksheets under the appropriate X-Z coordinates.

The program then iteratively increased the X-Z coordinate until the averaged irradiance values were obtained at each of the 25 points on the theoretical SRG surface at the desired central pitch. The central pitch value was then increased, until average irradiance values were derived at each of the 25 coordinates for the four central pitches. The Excel file for the specified lens position was then saved under the assigned file name, and the entire process was repeated for lens positions of $f = 45$ mm and $f = 55$ mm.

Appendix B Python Code

```
import numpy as np
import AnalyticSim as Analytic
import py_compile

py_compile.compile("AnalyticSim.py")

f1=14.3*10**-3
lam=532*10**-9
Theta500=np.arcsin(lam/(2*(500*10**-9)))
Theta1000=np.arcsin(lam/(2*(1000*10**-9)))
Theta1500=np.arcsin(lam/(2*(1500*10**-9)))
Theta2000=np.arcsin(lam/(2*(2000*10**-9)))


#This will be what the analytical data files derived by this program will be
#saved as

DocNames35=np.array(["35 X-30 Y-30.xls", "35 X-30 Y-15.xls", "35 X-30 Y0.xls",
                     "35 X-30 Y15.xls", "35 X-30 Y30.xls", "35 X-15 Y-30.xls",
                     "35 X-15 Y-15.xls", "35 X-15 Y0.xls", "35 X-15 Y15.xls",
                     "35 X-15 Y30.xls", "35 X0 Y-30.xls", "35 X0 Y-15.xls",
                     "35 X0 Y0.xls", "35 X0 Y15.xls", "35 X0 Y30.xls",
                     "35 X15 Y-30.xls", "35 X15 Y-15.xls", "35 X15 Y0.xls",
                     "35 X15 Y15.xls", "35 X15 Y30.xls", "35 X30 Y-30.xls",
                     "35 X30 Y-15.xls", "35 X30 Y0.xls", "35 X30 Y15.xls",
                     "35 X30 Y30.xls"])
DocNames45=np.array(["45 X-30 Y-30.xls", "45 X-30 Y-15.xls", "45 X-30 Y0.xls",
                     "45 X-30 Y15.xls", "45 X-30 Y30.xls", "45 X-15 Y-30.xls",
                     "45 X-15 Y-15.xls", "45 X-15 Y0.xls", "45 X-15 Y15.xls",
                     "45 X-15 Y30.xls", "45 X0 Y-30.xls", "45 X0 Y-15.xls",
                     "45 X0 Y0.xls", "45 X0 Y15.xls", "45 X0 Y30.xls",
                     "45 X15 Y-30.xls", "45 X15 Y-15.xls", "45 X15 Y0.xls",
                     "45 X15 Y15.xls", "45 X15 Y30.xls", "45 X30 Y-30.xls",
                     "45 X30 Y-15.xls", "45 X30 Y0.xls", "45 X30 Y15.xls",
                     "45 X30 Y30.xls"])
DocNames55=np.array(["55 X-30 Y-30.xls", "55 X-30 Y-15.xls", "55 X-30 Y0.xls",
                     "55 X-30 Y15.xls", "55 X-30 Y30.xls", "55 X-15 Y-30.xls",
                     "55 X-15 Y-15.xls", "55 X-15 Y0.xls", "55 X-15 Y15.xls",
                     "55 X-15 Y30.xls", "55 X0 Y-30.xls", "55 X0 Y-15.xls",
                     "55 X0 Y0.xls", "55 X0 Y15.xls", "55 X0 Y30.xls",
                     "55 X15 Y-30.xls", "55 X15 Y-15.xls", "55 X15 Y0.xls",
                     "55 X15 Y15.xls", "55 X15 Y30.xls", "55 X30 Y-30.xls",
                     "55 X30 Y-15.xls", "55 X30 Y0.xls", "55 X30 Y15.xls",
                     "55 X30 Y30.xls"])

#This sets the Upper and the Lower bounds for the sample I am moddeling.
#For this I have set it so that the two are 10 micrometers apart, modeling a
#scan size of 10 micormeters. I will most likely change this to 5 micrometers
#for the 500 nm and 1000 nm models later some how to more accurately represent
#the experimental data.

Inc=50
for SN in range (0,3):
    XLower=995000
    XUpper=1005000
    a=0
    if SN==0:
```

```
        print ("35 mm")
        for SX in range (0,5):
            ZLower=-2005000
            ZUpper=-1995000
            for SZ in range (0,5):
                DocName1=DocNames35[a]
                f=35*10**-3
                Analytic.AnalyticSim(f,f1,Theta500,Theta1000,Theta1500,
                                     Theta2000, XLower, XUpper, ZLower, ZUpper,
                                     Inc, DocName1)
                print (ZLower)
                a=a+1
                ZLower=ZLower+1000000
                ZUpper=ZUpper+1000000
            XLower=XLower+1000000
            XUpper=XUpper+1000000
    if SN==1:
        print ("45 mm")
        for SX in range (0,5):
            ZLower=-2505000
            ZUpper=-2495000
            for SZ in range (0,5):
                DocName1=DocNames45[a]
                f=45*10**-3
                Analytic.AnalyticSim(f,f1,Theta500,Theta1000,Theta1500,
                                     Theta2000, XLower, XUpper, ZLower, ZUpper,
                                     Inc, DocName1)
                print (ZLower)
                a=a+1
                ZLower=ZLower+1250000
                ZUpper=ZUpper+1250000
            XLower=XLower+1250000
            XUpper=XUpper+1250000
    if SN==2:
        print ("55 mm")
        for SX in range (0,5):
            ZLower=-2505000
            ZUpper=-2495000
            for SZ in range (0,5):
                DocName1=DocNames55[a]
                f=55*10**-3
                Analytic.AnalyticSim(f,f1,Theta500,Theta1000,Theta1500,
                                     Theta2000, XLower, XUpper, ZLower, ZUpper,
                                     Inc, DocName1)
                print (ZLower)
                a=a+1
                ZLower=ZLower+1250000
                ZUpper=ZUpper+1250000
            XLower=XLower+1250000
            XUpper=XUpper+1250000


AngleValues=np.zeros(shape=(5,5))
PitchValues=np.zeros(shape=(5,5))

print("done")
```

```
def AnalyticSim (f, f1, Theta500, Theta1000, Theta1500, Theta2000, XLower,
                 XUpper, ZLower, ZUpper, Inc, DocName1):
    import numpy as np
    import xlwt

    lam=532*10**-9
    pi=np.pi
    L=7*10**-3

    def Delta500(x,z):
        return(-(4*pi*(x/(1*10**9))*np.sin(Theta500)/lam)+(2*pi/lam)*
               (((f-(x/(1*10**9))*np.sin(Theta500)-f1)**2+(abs((x/(1*10**9))-
                (L/2))*np.cos(Theta500))**2+abs(z/(1*10**9))**2)**(1/2)-
                f+(x/(1*10**9))*np.sin(Theta500)+f1))

    def Delta1000(x,z):
        return(-(4*pi*(x/(1*10**9))*np.sin(Theta1000)/lam)+(2*pi/lam)*
               (((f-(x/(1*10**9))*np.sin(Theta1000)-f1)**2+(abs((x/(1*10**9))-
                (L/2))*np.cos(Theta1000))**2+abs(z/(1*10**9))**2)**(1/2)-
                f+(x/(1*10**9))*np.sin(Theta1000)+f1))

    def Delta1500(x,z):
        return(-(4*pi*(x/(1*10**9))*np.sin(Theta1500)/lam)+(2*pi/lam)*
               (((f-(x/(1*10**9))*np.sin(Theta1500)-f1)**2+(abs((x/(1*10**9))-
                (L/2))*np.cos(Theta1500))**2+abs(z/(1*10**9))**2)**(1/2)-
                f+(x/(1*10**9))*np.sin(Theta1500)+f1))

    def Delta2000(x,z):
        return(-(4*pi*(x/(1*10**9))*np.sin(Theta2000)/lam)+(2*pi/lam)*
               (((f-(x/(1*10**9))*np.sin(Theta2000)-f1)**2+(abs((x/(1*10**9))-
                (L/2))*np.cos(Theta2000))**2+abs(z/(1*10**9))**2)**(1/2)-
                f+(x/(1*10**9))*np.sin(Theta2000)+f1))

    book = xlwt.Workbook(encoding="utf-8")
    sheet1=book.add_sheet("Sheet1")
    sheet2=book.add_sheet("Sheet2")
    sheet3=book.add_sheet("Sheet3")
    sheet4=book.add_sheet("Sheet4")

    a=0
    b=0
    for x in range (XLower,XUpper,Inc):
        b=0
        for z in range (ZLower,ZUpper,Inc):
            sheet1.write(b, a, float(np.sin((Delta500(x,z)))))
            b=b+1
        a=a+1

    a=0
    b=0
    for x in range (XLower, XUpper, Inc):
        b=0
        for z in range (ZLower, ZUpper, Inc):
            sheet2.write(b, a, float(np.sin((Delta1000(x,z)))))
            b=b+1
        a=a+1
```

```
a=0
b=0
for x in range (XLower, XUpper, Inc):
    b=0
    for z in range (ZLower, ZUpper, Inc):
        sheet3.write(b, a, float(np.sin((Delta1500(x,z)))))
        b=b+1
    a=a+1

a=0
b=0
for x in range (XLower, XUpper, Inc):
    b=0
    for z in range (ZLower, ZUpper, Inc):
        sheet4.write(b, a, float(np.sin((Delta2000(x,z)))))
        b=b+1
    a=a+1

book.save(DocName1)
```

```
import numpy as np
import xlwt
import AngleFinder2 as AFind
import PeakFinder as PFind
import PitchFinder as PitFind
import py_compile

#This file we will use to calculate the angles and pitches for each of the vector
#plots that are being derived in the Vector Plot Generator File. Therefore we will
#be using the AngleFinder, PeakFinder, and PitchFinder programs.

py compile.compile("AngleFinder2.py")
py compile.compile("PeakFinder.py")
py_compile.compile("PitchFinder.py")

#We will also be using the files that have been generated in the Vector Plot Generator
#File and be accessing each individually to generate the desired values.

DocNames35=np.array(["35 X-30 Y-30.xls", "35 X-30 Y-15.xls", "35 X-30 Y0.xls",
                     "35 X-30 Y15.xls", "35 X-30 Y30.xls", "35 X-15 Y-30.xls",
                     "35 X-15 Y-15.xls", "35 X-15 Y0.xls", "35 X-15 Y15.xls",
                     "35 X-15 Y30.xls", "35 X0 Y-30.xls", "35 X0 Y-15.xls",
                     "35 X0 Y0.xls", "35 X0 Y15.xls", "35 X0 Y30.xls",
                     "35 X15 Y-30.xls", "35 X15 Y-15.xls", "35 X15 Y0.xls",
                     "35 X15 Y15.xls", "35 X15 Y30.xls", "35 X30 Y-30.xls",
                     "35 X30 Y-15.xls", "35 X30 Y0.xls", "35 X30 Y15.xls",
                     "35 X30 Y30.xls"])
DocNames45=np.array(["45 X-30 Y-30.xls", "45 X-30 Y-15.xls", "45 X-30 Y0.xls",
                     "45 X-30 Y15.xls", "45 X-30 Y30.xls", "45 X-15 Y-30.xls",
                     "45 X-15 Y-15.xls", "45 X-15 Y0.xls", "45 X-15 Y15.xls",
                     "45 X-15 Y30.xls", "45 X0 Y-30.xls", "45 X0 Y-15.xls",
                     "45 X0 Y0.xls", "45 X0 Y15.xls", "45 X0 Y30.xls",
                     "45 X15 Y-30.xls", "45 X15 Y-15.xls", "45 X15 Y0.xls",
                     "45 X15 Y15.xls", "45 X15 Y30.xls", "45 X30 Y-30.xls",
                     "45 X30 Y-15.xls", "45 X30 Y0.xls", "45 X30 Y15.xls",
                     "45 X30 Y30.xls"])
DocNames55=np.array(["55 X-30 Y-30.xls", "55 X-30 Y-15.xls", "55 X-30 Y0.xls",
                     "55 X-30 Y15.xls", "55 X-30 Y30.xls", "55 X-15 Y-30.xls",
                     "55 X-15 Y-15.xls", "55 X-15 Y0.xls", "55 X-15 Y15.xls",
                     "55 X-15 Y30.xls", "55 X0 Y-30.xls", "55 X0 Y-15.xls",
                     "55 X0 Y0.xls", "55 X0 Y15.xls", "55 X0 Y30.xls",
                     "55 X15 Y-30.xls", "55 X15 Y-15.xls", "55 X15 Y0.xls",
                     "55 X15 Y15.xls", "55 X15 Y30.xls", "55 X30 Y-30.xls",
                     "55 X30 Y-15.xls", "55 X30 Y0.xls", "55 X30 Y15.xls",
                     "55 X30 Y30.xls"])

book = xlwt.Workbook(encoding="utf-8")
sheet1=book.add_sheet("35mm Distance")
sheet2=book.add_sheet("45mm Distance")
sheet3=book.add_sheet("55mm Distance")

sheet1.write(0,0, "Angle 500")
sheet1.write(0,1, "Pitch 500")
sheet1.write(0,2, "Angle 1000")
sheet1.write(0,3, "Pitch 1000")
sheet1.write(0,4, "Angle 1500")
sheet1.write(0,5, "Pitch 1500")
```

```
sheet1.write(0,6, "Angle 2000")
sheet1.write(0,7, "Pitch 2000")

sheet2.write(0,0, "Angle 500")
sheet2.write(0,1, "Pitch 500")
sheet2.write(0,2, "Angle 1000")
sheet2.write(0,3, "Pitch 1000")
sheet2.write(0,4, "Angle 1500")
sheet2.write(0,5, "Pitch 1500")
sheet2.write(0,6, "Angle 2000")
sheet2.write(0,7, "Pitch 2000")

sheet3.write(0,0, "Angle 500")
sheet3.write(0,1, "Pitch 500")
sheet3.write(0,2, "Angle 1000")
sheet3.write(0,3, "Pitch 1000")
sheet3.write(0,4, "Angle 1500")
sheet3.write(0,5, "Pitch 1500")
sheet3.write(0,6, "Angle 2000")
sheet3.write(0,7, "Pitch 2000")

XLower=995000
Angle=np.array([0,0,0,0])
Pitch=np.array([0,0,0,0])
a=0
for SX in range (0,5):
    ZLower=-2005000
    for SZ in range (0,5):
        print("a is", a)
        FileName=DocNames35[a]
        print(FileName)
        for ShN in range (0,4):
            SheetNum=ShN
            Peaks=PFind.PeakFinder(FileName, SheetNum)
            Peaks0=Peaks[0]
            Peaks50=Peaks[1]
            Peaks100=Peaks[2]
            Peaks150=Peaks[3]
            print ("XLower is", XLower)
            print ("ZLower is", ZLower)
            Angle=AFind.AngleFinder2(Peaks0, Peaks50, Peaks100, Peaks150,
                                     ZLower)
            Pitch=PitFind.PitchFinder(Peaks0, Peaks50, Peaks100)
            sheet1.write(SZ+1+(SX*5), ShN*2, Angle)
            sheet1.write(SZ+1+(SX*5), ShN*2+1, Pitch)
        ZLower=ZLower+1000000
        a=a+1
    XLower=XLower+1000000

XLower=995000
a=0
for SX in range (0,5):
    ZLower=-2505000
    for SZ in range (0,5):
        print("a is", a)
        FileName=DocNames45[a]
        print(FileName)
```

```
        for ShN in range (0,4):
            SheetNum=ShN
            Peaks=PFind.PeakFinder(FileName, SheetNum)
            Peaks0=Peaks[0]
            Peaks50=Peaks[1]
            Peaks100=Peaks[2]
            Peaks150=Peaks[3]
            print ("XLower is", XLower)
            print ("ZLower is", ZLower)
            Angle=AFind.AngleFinder2(Peaks0, Peaks50, Peaks100, Peaks150,
                                     ZLower)
            Pitch=PitFind.PitchFinder(Peaks0, Peaks50, Peaks100)
            sheet2.write(SZ+1+(SX*5), ShN*2, Angle)
            sheet2.write(SZ+1+(SX*5), ShN*2+1, Pitch)
        ZLower=ZLower+1250000
        a=a+1
    XLower=XLower+1250000

XLower=995000
a=0
for SX in range (0,5):
    ZLower=-2505000
    for SZ in range (0,5):
        print("a is", a)
        FileName=DocNames55[a]
        print(FileName)
        for ShN in range (0,4):
            SheetNum=ShN
            Peaks=PFind.PeakFinder(FileName, SheetNum)
            Peaks0=Peaks[0]
            Peaks50=Peaks[1]
            Peaks100=Peaks[2]
            Peaks150=Peaks[3]
            print ("XLower is", XLower)
            print ("ZLower is", ZLower)
            Angle=AFind.AngleFinder2(Peaks0, Peaks50, Peaks100, Peaks150,
                                     ZLower)
            Pitch=PitFind.PitchFinder(Peaks0, Peaks50, Peaks100)
            sheet3.write(SZ+1+(SX*5), ShN*2, Angle)
            sheet3.write(SZ+1+(SX*5), ShN*2+1, Pitch)
        ZLower=ZLower+1250000
        a=a+1
    XLower=XLower+1250000

book.save("Theoretical Computation V1.xls")
print("done")
```

```
def PeakFinder (FileName, SheetNum):

    import numpy as np
    import xlrd

    book=xlrd.open workbook(FileName)
    sheet1=book.sheet_by_index(SheetNum)
    a=0
    b=0

    Peaks1=np.zeros(shape=(30, 1))
    Peaks2=np.zeros(shape=(30, 1))
    Peaks3=np.zeros(shape=(30,1))
    Peaks4=np.zeros(shape=(30, 1))

    while a<200:
        l=0
        for b in range (2, 197):
            if sheet1.cell(a,b).value>sheet1.cell(a,b-1).value:
                if sheet1.cell(a,b).value>sheet1.cell(a,b-2).value:
                    if sheet1.cell(a,b).value>sheet1.cell(a,b+1).value:
                        if sheet1.cell(a,b).value>sheet1.cell(a,b+2).value:
                            if a==0:
                                Peaks1[l,0]=b
                                #print(Peaks1[l,0], "b is", b)
                                #print("Value 1 is", sheet1.cell(a,b).value)
                                b=b+1
                                l=l+1
                            if a==50:
                                Peaks2[l,0]=b
                                #print(Peaks2[l,0], "b is", b)
                                #print("Value 2 is", sheet1.cell(a,b).value)
                                b=b+1
                                l=l+1
                            if a==100:
                                Peaks3[l,0]=b
                                #print(Peaks3[l,0], "b is", b)
                                #print("Value 3 is", sheet1.cell(a,b).value)
                                b=b+1
                                l=l+1
                            if a==150:
                                Peaks4[l,0]=b
                                #print(Peaks4[l,0], "b is", b)
                                #print("Value 4 is", sheet1.cell(a,b).value)
                                b=b+1
                                l=l+1
                            else:
                                a=a
                        else:
                            b=b+1
                    else:
                        b=b+1
                else:
                    b=b+1
            else:
                b=b+1
        a=a+50
```

```
#print (Peaks1, Peaks2, Peaks3, Peaks4)
return (Peaks1, Peaks2, Peaks3, Peaks4)
```

```
def PitchFinder (Peaks1, Peaks2, Peaks3):

    import numpy as np

    Pitches1=np.zeros(shape=(30, 1))
    Pitches2=np.zeros(shape=(30, 1))
    Pitches3=np.zeros(shape=(30,1))
    for a in range (0, 29):
        Pitches1[a,0]=(Peaks1[a+1,0]-Peaks1[a,0])/200*10000
        Pitches2[a,0]=(Peaks2[a+1,0]-Peaks2[a,0])/200*10000
        Pitches3[a,0]=(Peaks3[a+1,0]-Peaks3[a,0])/200*10000

    #print(Pitches1, Pitches2, Pitches3)

    PSum1=0
    PSum2=0
    PSum3=0
    for a in range (0, 29):
        if Pitches1[a,0]>0:
            PSum1=PSum1+Pitches1[a,0]
        else:
            b=0
        if Pitches2[a,0]>0:
            PSum2=PSum2+Pitches2[a,0]
        else:
            b=0
        if Pitches3[a,0]>0:
            PSum3=PSum3+Pitches3[a,0]
        else:
            b=0

    PInt1=0
    PInt2=0
    PInt3=0
    for a in range (0, 29):
        if Pitches1[a,0]>0:
            PInt1=a+1
        else:
            b=0
        if Pitches2[a,0]>0:
            PInt2=a+1
        else:
            b=0
        if Pitches3[a,0]>0:
            PInt3=a+1
        else:
            b=0

    Pitch=((PSum1/PInt1)+(PSum2/PInt2)+(PSum3/PInt3))/3

    return (Pitch)
```

```
def AngleFinder2 (Peaks1, Peaks2, Peaks3, Peaks4, ZLower):

    import numpy as np

    pi=np.pi

    Angles1=np.zeros(shape=(30, 1))
    Angles2=np.zeros(shape=(30, 1))
    Angles3=np.zeros(shape=(30,1))

    a=0
    for a in range (0, 29):
        if ZLower+5000<0:
            if Peaks1[a,0]!=0 and Peaks2[a,0]!=0 and Peaks3[a,0]!=0:
                if Peaks1[a,0]>Peaks2[a,0]:
                    Angles1[a,0]=(np.arctan(((Peaks2[a,0]-Peaks1[a,0])/50)))*180/pi
                else:
                    Angles1[a,0]=(np.arctan(((Peaks2[a,0]-Peaks1[a+1,0])/50)))*180/pi
                if Peaks2[a,0]>Peaks3[a,0]:
                    Angles2[a,0]=(np.arctan(((Peaks3[a,0]-Peaks2[a,0])/50)))*180/pi
                else:
                    Angles2[a,0]=(np.arctan(((Peaks3[a,0]-Peaks2[a+1,0])/50)))*180/pi
                if Peaks3[a,0]>Peaks4[a,0]:
                    Angles3[a,0]=(np.arctan(((Peaks4[a,0]-Peaks3[a,0])/50)))*180/pi
                else:
                    Angles3[a,0]=(np.arctan(((Peaks4[a,0]-Peaks3[a+1,0])/50)))*180/pi
            else:
                b=0

        if ZLower+5000==0:
            if Peaks1[a,0]!=0 and Peaks2[a,0]!=0 and Peaks3[a,0]!=0:
                if Peaks1[a,0]>Peaks2[a,0]:
                    Angles1[a,0]=(np.arctan((Peaks1[a,0]-Peaks2[a,0])/50))*180/pi
                else:
                    Angles1[a,0]=(np.arctan((Peaks1[a,0]-Peaks2[a,0])/50))*180/pi
                if Peaks2[a,0]>Peaks3[a,0]:
                    Angles2[a,0]=(np.arctan((Peaks2[a,0]-Peaks3[a,0])/50))*180/pi
                else:
                    Angles2[a,0]=(np.arctan((Peaks2[a,0]-Peaks3[a,0])/50))*180/pi
                if Peaks3[a,0]>Peaks4[a,0]:
                    Angles3[a,0]=(np.arctan((Peaks3[a,0]-Peaks4[a,0])/50))*180/pi
                else:
                    Angles3[a,0]=(np.arctan((Peaks3[a,0]-Peaks4[a,0])/50))*180/pi
            else:
                b=0

        if ZLower+5000>0:
            if Peaks1[a,0]!=0 and Peaks2[a,0]!=0 and Peaks3[a,0]!=0:
                if Peaks1[a,0]<Peaks2[a,0]:
                    Angles1[a,0]=(np.arctan((Peaks2[a,0]-Peaks1[a,0])/50))*180/pi
                else:
                    Angles1[a,0]=(np.arctan((Peaks2[a+1,0]-Peaks1[a,0])/50))*180/pi
                if Peaks2[a,0]<Peaks3[a,0]:
                    Angles2[a,0]=(np.arctan((Peaks3[a,0]-Peaks2[a,0])/50))*180/pi
                else:
                    Angles2[a,0]=(np.arctan((Peaks3[a+1,0]-Peaks2[a,0])/50))*180/pi
                if Peaks3[a,0]<Peaks4[a,0]:
```

```
                Angles3[a,0]=(np.arctan((Peaks4[a,0]-Peaks3[a,0])/50))*180/pi
            else:
                Angles3[a,0]=(np.arctan((Peaks4[a+1,0]-Peaks3[a,0])/50))*180/pi
        else:
            b=0

Sum1=0
Sum2=0
Sum3=0

if ZLower+5000<0:
    for a in range (0, 29):
        if Angles1[a,0]<0:
            Sum1=Sum1+Angles1[a,0]
        else:
            b=0
        if Angles2[a,0]<0:
            Sum2=Sum2+Angles2[a,0]
        else:
            b=0
        if Angles3[a,0]<0:
            Sum3=Sum3+Angles3[a,0]
        else:
            b=0
if ZLower+5000==0:
    for a in range (0, 29):
        if -20<Angles1[a,0]<20:
            Sum1=Sum1+Angles1[a,0]
        else:
            b=0
        if -20<Angles2[a,0]<20:
            Sum2=Sum2+Angles2[a,0]
        else:
            b=0
        if -20<Angles3[a,0]<20:
            Sum3=Sum3+Angles3[a,0]
        else:
            b=0
if ZLower+5000>0:
    for a in range (0, 29):
        if Angles1[a,0]>0:
            Sum1=Sum1+Angles1[a,0]
        else:
            b=0
        if Angles2[a,0]>0:
            Sum2=Sum2+Angles2[a,0]
        else:
            b=0
        if Angles3[a,0]>0:
            Sum3=Sum3+Angles3[a,0]
        else:
            b=0

if ZLower+5000<=0:
    for a in range (0, 29):
        if Angles1[a,0]<0:
            Int1=a+1
```

```
        else:
            b=0
        if Angles2[a,0]<0:
            Int2=a+1
        else:
            b=0
        if Angles3[a,0]<0:
            Int3=a+1
        else:
            b=0

if ZLower+5000==0:
    for a in range (0, 29):
        if -20<Angles1[a,0]<20:
            Int1=a+1
        else:
            b=0
        if -20<Angles2[a,0]<20:
            Int2=a+1
        else:
            b=0
        if -20<Angles3[a,0]<20:
            Int3=a+1
        else:
            b=0

if ZLower+5000>0:
    for a in range (0, 29):
        if Angles1[a,0]>0:
            Int1=a+1
        else:
            b=0
        if Angles2[a,0]>0:
            Int2=a+1
        else:
            b=0
        if Angles3[a,0]>0:
            Int3=a+1
        else:
            b=0

Angle=((Sum1/Int1)+(Sum2/Int2)+(Sum3/Int3))/3

return (Angle)
```

```
# -*- coding: utf-8 -*-
"""
Created on Mon Dec  4 15:49:49 2017

@author: Nicholas Swanson
"""

import numpy as np
import xlwt
import IradianceDistribution2 as IradDist

#IRad=Iradiance; LensDi=Lens Diameter; lam=wavelength of laser; f=focal length
#of lens; L=radius of laser beam; Phi=beam angle from lens; LArea=Lens area;
#OpAx=optical axis position; SDist=distance of sample from the focal point;
#HRad=hypothetical radius of beam on the sample
Irad=4280
LensDi=5.72*10**-3
lam=532*10**-9
f=14.3*10**-3
L=7*10**-3
pi=np.pi
Phi=np.arctan((LensDi/2)/f)

Theta500=np.arcsin(lam/(2*(500*10**-9)))
Theta1000=np.arcsin(lam/(2*(1000*10**-9)))
Theta1500=np.arcsin(lam/(2*(1500*10**-9)))
Theta2000=np.arcsin(lam/(2*(2000*10**-9)))

DocNames35=np.array(["Irad 35 X-30 Y-30.xls", "Irad 35 X-30 Y-15.xls",
                     "Irad 35 X-30 Y0.xls", "Irad 35 X-30 Y15.xls",
                     "Irad 35 X-30 Y30.xls", "Irad 35 X-15 Y-30.xls",
                     "Irad 35 X-15 Y-15.xls", "Irad 35 X-15 Y0.xls",
                     "Irad 35 X-15 Y15.xls", "Irad 35 X-15 Y30.xls",
                     "Irad 35 X0 Y-30.xls", "Irad 35 X0 Y-15.xls",
                     "Irad 35 X0 Y0.xls", "Irad 35 X0 Y15.xls",
                     "Irad 35 X0 Y30.xls", "Irad 35 X15 Y-30.xls",
                     "Irad 35 X15 Y-15.xls", "Irad 35 X15 Y0.xls",
                     "Irad 35 X15 Y15.xls", "Irad 35 X15 Y30.xls",
                     "Irad 35 X30 Y-30.xls", "Irad 35 X30 Y-15.xls",
                     "Irad 35 X30 Y0.xls", "Irad 35 X30 Y15.xls",
                     "Irad 35 X30 Y30.xls"])
DocNames45=np.array(["Irad 45 X-30 Y-30.xls", "Irad 45 X-30 Y-15.xls",
                     "Irad 45 X-30 Y0.xls", "Irad 45 X-30 Y15.xls",
                     "Irad 45 X-30 Y30.xls", "Irad 45 X-15 Y-30.xls",
                     "Irad 45 X-15 Y-15.xls", "Irad 45 X-15 Y0.xls",
                     "Irad 45 X-15 Y15.xls", "Irad 45 X-15 Y30.xls",
                     "Irad 45 X0 Y-30.xls", "Irad 45 X0 Y-15.xls",
                     "Irad 45 X0 Y0.xls", "Irad 45 X0 Y15.xls",
                     "Irad 45 X0 Y30.xls", "Irad 45 X15 Y-30.xls",
                     "Irad 45 X15 Y-15.xls", "Irad 45 X15 Y0.xls",
                     "Irad 45 X15 Y15.xls", "Irad 45 X15 Y30.xls",
                     "Irad 45 X30 Y-30.xls", "Irad 45 X30 Y-15.xls",
                     "Irad 45 X30 Y0.xls", "Irad 45 X30 Y15.xls",
                     "Irad 45 X30 Y30.xls"])
DocNames55=np.array(["Irad 55 X-30 Y-30.xls", "Irad 55 X-30 Y-15.xls",
                     "Irad 55 X-30 Y0.xls", "Irad 55 X-30 Y15.xls",
                     "Irad 55 X-30 Y30.xls", "Irad 55 X-15 Y-30.xls",
```

```
                    "Irad 55 X-15 Y-15.xls", "Irad 55 X-15 Y0.xls",
                    "Irad 55 X-15 Y15.xls", "Irad 55 X-15 Y30.xls",
                    "Irad 55 X0 Y-30.xls", "Irad 55 X0 Y-15.xls",
                    "Irad 55 X0 Y0.xls", "Irad 55 X0 Y15.xls",
                    "Irad 55 X0 Y30.xls", "Irad 55 X15 Y-30.xls",
                    "Irad 55 X15 Y-15.xls", "Irad 55 X15 Y0.xls",
                    "Irad 55 X15 Y15.xls", "Irad 55 X15 Y30.xls",
                    "Irad 55 X30 Y-30.xls", "Irad 55 X30 Y-15.xls",
                    "Irad 55 X30 Y0.xls", "Irad 55 X30 Y15.xls",
                    "Irad 55 X30 Y30.xls"])

LArea=(((LensDi)/2)**2)*pi
P2=Irad*LArea
Pl=Irad*((L**2)*pi)/2
FileName=np.array(["Depth 35mm Distance.xls", "Depth 45mm Distance.xls",
                   "Depth 55mm Distance.xls"])

F=35*10**-3
i=0
while (F<=56*10**-3):
    book = xlwt.Workbook(encoding="utf-8")
    sheet1=book.add_sheet("500nm")
    sheet2=book.add_sheet("1000nm")
    sheet3=book.add_sheet("1500nm")
    sheet4=book.add_sheet("2000nm")

    sheet1.write(0,0,"PositionX")
    sheet1.write(0,1,"PositionY")
    sheet1.write(0,2,"Irradiance Left")
    sheet1.write(0,3,"Irradiance Right")
    sheet1.write(0,4,"Irradiance Total")

    sheet2.write(0,0,"PositionX")
    sheet2.write(0,1,"PositionY")
    sheet2.write(0,2,"Irradiance Left")
    sheet2.write(0,3,"Irradiance Right")
    sheet2.write(0,4,"Irradiance Total")

    sheet3.write(0,0,"PositionX")
    sheet3.write(0,1,"PositionY")
    sheet3.write(0,2,"Irradiance Left")
    sheet3.write(0,3,"Irradiance Right")
    sheet3.write(0,4,"Irradiance Total")

    sheet4.write(0,0,"PositionX")
    sheet4.write(0,1,"PositionY")
    sheet4.write(0,2,"Irradiance Left")
    sheet4.write(0,3,"Irradiance Right")
    sheet4.write(0,4,"Irradiance Total")

    Pitch=500
    while (Pitch<=2100):
        xmid=1*10**-3
        Q=0
        for a in range (0,5):
            Theta=np.arcsin(lam/(2*(Pitch*10**-9)))
            dxmid=xmid*np.sin(Theta)
```

```
SDist=F-f-dxmid
MLength=L/np.cos(Theta)
MArea=MLength*L*pi/2
if F==35*10**-3:
    ymid=-2*10**-3
else:
    ymid=-2.5*10**-3
if ((xmid-L/2)**2/MLength**2)+(ymid**2/L**2)<=1:
    I1=P1/MArea
else:
    I1=0
for b in range (0,5):
    if 30*10**-3<F<40*10**-3:
        DocName=DocNames35[Q]
        print(DocName)
    if 40*10**-3<F<50*10**-3:
        DocName=DocNames45[Q]
        print(DocName)
    if 50*10**-3<F<60*10**-3:
        DocName=DocNames55[Q]
        print(DocName)
    Averages=IradDist.IradDist(xmid, ymid, L, Phi, SDist, Theta,
                               lam, I1, Pitch, DocName, MLength,
                               F, f, P2)
    print("Pitch is", Pitch)
    print("Averages are", Averages[0], Averages[1], Averages[2])
    I2=Averages[0]
    I12=Averages[1]
    IT=Averages[2]
    if Pitch==500:
        sheet1.write((a*5)+b+1,0,xmid)
    if Pitch==1000:
        sheet2.write((a*5)+b+1,0,xmid)
    if Pitch==1500:
        sheet3.write((a*5)+b+1,0,xmid)
    if Pitch==2000:
        sheet4.write((a*5)+b+1,0,xmid)
    if Pitch==500:
        sheet1.write((a*5)+b+1,1,ymid)
    if Pitch==1000:
        sheet2.write((a*5)+b+1,1,ymid)
    if Pitch==1500:
        sheet3.write((a*5)+b+1,1,ymid)
    if Pitch==2000:
        sheet4.write((a*5)+b+1,1,ymid)
    if Pitch==500:
        sheet1.write((a*5)+b+1,2,I1)
    if Pitch==1000:
        sheet2.write((a*5)+b+1,2,I1)
    if Pitch==1500:
        sheet3.write((a*5)+b+1,2,I1)
    if Pitch==2000:
        sheet4.write((a*5)+b+1,2,I1)
    if Pitch==500:
        sheet1.write((a*5)+b+1,3,I2)
    if Pitch==1000:
        sheet2.write((a*5)+b+1,3,I2)
```

```
            if Pitch==1500:
                sheet3.write((a*5)+b+1,3,I2)
            if Pitch==2000:
                sheet4.write((a*5)+b+1,3,I2)
            if Pitch==500:
                sheet1.write((a*5)+b+1,4,IT)
            if Pitch==1000:
                sheet2.write((a*5)+b+1,4,IT)
            if Pitch==1500:
                sheet3.write((a*5)+b+1,4,IT)
            if Pitch==2000:
                sheet4.write((a*5)+b+1,4,IT)
            if F==35*10**-3:
                ymid=ymid+1*10**-3
            else:
                ymid=ymid+1.25*10**-3
            Q=Q+1
        if F==35*10**-3:
            xmid=xmid+1*10**-3
        else:
            xmid=xmid+1.25*10**-3
    Pitch=Pitch+500
book.save(FileName[i])

i=i+1
F=F+10*10**-3
```

```
# -*- coding: utf-8 -*-
"""
Created on Mon Dec 11 15:27:52 2017

@author: Nicholas
"""

def IradDist (xmid, ymid, L, Phi, SDist, Theta, lam, I1, Pitch, DocName,
              MLength, F, f, P2) :

    import numpy as np
    import xlwt
    from xlrd import open workbook
    from xlutils.copy import copy

    if Pitch==500:
        book = xlwt.Workbook(encoding="utf-8")

        sheet1=book.add_sheet("I2 500nm")
        sheet2=book.add sheet("I2 1000nm")
        sheet3=book.add sheet("I2 1500nm")
        sheet4=book.add_sheet("I2 2000nm")

        sheet5=book.add sheet("I12 500nm")
        sheet6=book.add sheet("I12 1000nm")
        sheet7=book.add sheet("I12 1500nm")
        sheet8=book.add_sheet("I12 2000nm")

        sheet9=book.add sheet("IT 500nm")
        sheet10=book.add sheet("IT 1000nm")
        sheet11=book.add sheet("IT 1500nm")
        sheet12=book.add_sheet("IT 2000nm")

    if Pitch==1000:
        book=open workbook(DocName)
        wbook=copy(book)
        sheet2=wbook.get sheet(1)
        sheet6=wbook.get sheet(5)
        sheet10=wbook.get_sheet(9)

    if Pitch==1500:
        book=open workbook(DocName)
        wbook=copy(book)
        sheet3=wbook.get sheet(2)
        sheet7=wbook.get sheet(6)
        sheet11=wbook.get_sheet(10)

    if Pitch==2000:
        book=open_workbook(DocName)
        wbook=copy(book)
        sheet4=wbook.get sheet(3)
        sheet8=wbook.get sheet(7)
        sheet12=wbook.get_sheet(11)


    I2A500=np.zeros(shape=(101,101))
    I2A1000=np.zeros(shape=(101,101))
```

```
I2A1500=np.zeros(shape=(101,101))
I2A2000=np.zeros(shape=(101,101))
I12A500=np.zeros(shape=(101,101))
I12A1000=np.zeros(shape=(101,101))
I12A1500=np.zeros(shape=(101,101))
I12A2000=np.zeros(shape=(101,101))
ITA500=np.zeros(shape=(101,101))
ITA1000=np.zeros(shape=(101,101))
ITA1500=np.zeros(shape=(101,101))
ITA2000=np.zeros(shape=(101,101))

C1=1
pi=np.pi
x=xmid-2.5*10**-6
while(x<xmid+2.5*10**-6+2.0*10**-9):
    C2=1
    y=ymid-2.5*10**-6
    while (y<ymid+2.5*10**-6+2.0*10**-9):
        if (xmid**2/MLength**2)+(ymid**2/L**2)<=1 and (xmid-L/2)**2+y**2<=
            (SDist)*np.tan(Phi):
            dx=x*np.sin(Theta)
            SD=F-f-(dx)
            BWidth=SD*np.tan(Phi)
            I2=P2/(BWidth**2*pi)
            delta=(-(4*pi*(x)*np.sin(Theta)/lam)+(2*pi/lam)*
                   (((F-(x)*np.sin(Theta)-f)**
                     2+(abs((x)-(L/2))*np.cos(Theta))**2+abs(y)**2)**(1/2)-
                      F+(x)*np.sin(Theta)+f))
            I12=2*(I1*I2)**(1/2)*np.cos(delta)
            IT=I2+I1+I12
            if 400<Pitch<600:
                sheet1.write(C1-1,C2-1,I2)
                I2A500[C1-1,C2-1]=I2
            if 900<Pitch<1100:
                sheet2.write(C1-1,C2-1,I2)
                I2A1000[C1-1,C2-1]=I2
            if 1400<Pitch<1600:
                sheet3.write(C1-1,C2-1,I2)
                I2A1500[C1-1,C2-1]=I2
            if 1900<Pitch<2100:
                sheet4.write(C1-1,C2-1,I2)
                I2A2000[C1-1,C2-1]=I2
            if 400<Pitch<600:
                sheet5.write(C1-1,C2-1,I12)
                I12A500[C1-1,C2-1]=I12
            if 900<Pitch<1100:
                sheet6.write(C1-1,C2-1,I12)
                I12A1000[C1-1,C2-1]=I12
            if 1400<Pitch<1600:
                sheet7.write(C1-1,C2-1,I12)
                I12A1500[C1-1,C2-1]=I12
            if 1900<Pitch<2100:
                sheet8.write(C1-1,C2-1,I12)
                I12A2000[C1-1,C2-1]=I12
            if 400<Pitch<600:
                sheet9.write(C1-1,C2-1,IT)
                ITA500[C1-1,C2-1]=IT
```

```
            if 900<Pitch<1100:
                sheet10.write(C1-1,C2-1,IT)
                ITA1000[C1-1,C2-1]=IT
            if 1400<Pitch<1600:
                sheet11.write(C1-1,C2-1,IT)
                ITA1500[C1-1,C2-1]=IT
            if 1900<Pitch<2100:
                sheet12.write(C1-1,C2-1,IT)
                ITA2000[C1-1,C2-1]=IT
        else:
            IT=0

        C2=C2+1
        y=y+0.50*10**-7
    C1=C1+1
    x=x+0.50*10**-7
if 400<Pitch<600:
    I2Av=I2A500.mean()
    I12Av=I12A500.mean()
    ITAv=ITA500.mean()
if 900<Pitch<1100:
    I2Av=I2A1000.mean()
    I12Av=I12A1000.mean()
    ITAv=ITA1000.mean()
if 1400<Pitch<1600:
    I2Av=I2A1500.mean()
    I12Av=I12A1500.mean()
    ITAv=ITA1500.mean()
if 1900<Pitch<2100:
    I2Av=I2A2000.mean()
    I12Av=I12A2000.mean()
    ITAv=ITA2000.mean()
if Pitch==500:
    book.save(DocName)

if Pitch==1000:
    wbook.save(DocName)

if Pitch==1500:
    wbook.save(DocName)

if Pitch==2000:
    wbook.save(DocName)

return (I2Av, I12Av, ITAv)
```

Appendix C Error Tables

Table B.1: Experimental error of the modified Lloyd's mirror interferometer.

Error Source	**Order of Magnitude**	**Error Value**
X-Axis Lens Position	mm	0.3 mm
Z-Axis Lens Position	mm	0.3 mm
Lens Distance	mm	0.1 mm
Mirror Angle	Degrees	0.05º
Lens Angle	Degrees	0.2º

Table B.2: Mechanical error of the Bruker Dimension Edge AFM.

Error Source	**Order of Magnitude**	**Error Value**
Scanning Height	nm	0.2 nm
Scanning Position	µm	1 µm
Noise	pm	50 pm

Appendix D Papers Published from Research

N. Swanson and R.G. Sabat, “Inscription and analysis of non-uniform diffraction gratings in azobenzene molecular glass thin films,” *Opt. Express,* vol. 26, no. 7, pp. 7876-7887, 2018.